

Master's Thesis

Interpretation von Top-Quark-Messungen im Kontext anomaler Wtb -Kopplungen

Interpretation of Top Quark Measurements in the Context of Anomalous Wtb Couplings

prepared by

Nils-Arne Rosien

from Dannenberg (Elbe)

at the II. Institute of Physics

Thesis number: II.Physik-UniGö-MSc-2014/02
Thesis period: 22nd April 2014 until 21st October 2014
First referee: Prof. Dr. Arnulf Quadt
Second referee: Prof. Dr. Ariane Frey

Abstract

In this master of science thesis, a combination of measurements of top quark observables is performed to set bounds on anomalous couplings at the Wtb vertex. These observables are the W helicity fractions in the top quark decay and the t -channel cross section for the electroweak production of single top quarks. In the process of combination, correlations between the different sources of systematic uncertainties of the measurements are considered to set more precise bounds on the exclusion limits of anomalous Wtb couplings. In addition, a combination with a measurement of the branching ratio of the process $\bar{B} \rightarrow X_s \gamma$ is performed. Ensemble tests are used to test the capabilities of the framework. Four-, two-, and one-dimensional fits of the couplings are performed. The Standard Model values of the couplings are at least consistent with the resulting smallest 95.5% C.L. bounds. While the combination with the measurement of the B -physics observable improves the bounds on V_L , V_R and g_L , the sensitivity of the combination of the two top quark measurements on g_R is better than of the B -physics observable alone. The obtained bounds are used to estimate lower bounds on electroweak physics beyond the Standard Model.

Zusammenfassung

In dieser Masterarbeit werden zwei Messungen von Top-Quark-Observablen kombiniert, um Grenzen auf anomale Kopplungen am Wtb -Vertex zu setzen. Diese Observablen sind die W -Helizitäten im Top-Quark-Zerfall und der t -Kanal-Wirkungsquerschnitt für die elektroschwache Produktion einzelner Top-Quarks. Dabei werden die Korrelationen zwischen den einzelnen Quellen von Unsicherheiten der Messungen berücksichtigt, wodurch genauere Ausschlussgrenzen für anomale Wtb -Kopplungen gesetzt werden können. Zusätzlich wird das Potential einer weiteren Kombination mit einer Messung des Verzweigungsverhältnisses des Prozesses $\bar{B} \rightarrow X_s \gamma$ überprüft. Um die Möglichkeiten des Verfahrens zu testen, werden Ensembledests durchgeführt. Vier-, zwei-, und eindimensionale Fits der Kopplungen werden vorgenommen. Die Werte des Standardmodells für die Kopplungen sind mindestens konsistent mit den daraus resultierenden kleinsten 95.5% C.L.-Grenzen. Während die Kombination mit der Messung der B -Physik-Observablen die Grenzen auf V_L , V_R um g_L verkleinert, ist die Sensitivität der Kombination beider Top-Quark-Messungen auf g_R höher als die der B -Physik-Observablen einzeln. Die erhaltenen Grenzen werden dazu verwendet, untere Grenzen auf elektroschwache Physik jenseits des Standardmodells abzuschätzen.

Contents

Introduction	1
1 Fundamentals	3
1.1 The Standard Model of elementary particle physics	3
1.1.1 Fundamental Standard Model interactions and gauge bosons	4
1.1.2 Fermions	6
1.1.3 Mass generation with a toy theory	8
1.1.4 The electroweak model within the Standard Model	10
1.1.5 Limitations of the Standard Model	12
1.2 The top quark	13
1.3 Anomalous couplings at the Wtb vertex	17
1.4 W helicity fractions	21
1.5 t -channel single top quark production cross section	23
1.6 The Large Hadron Collider and the ATLAS experiment	24
2 Current measurements	29
2.1 W helicity fractions	29
2.2 t -channel single top quark production cross section	32
2.3 Categorisation of the uncertainties	34
3 Combination and fitting framework	45
3.1 The Bayesian method for the combination of measurements	45
3.2 Modelling of the observables	47
3.3 Strategy for the combination of the measurements	49
4 Standard setup of the analysis	55
5 Sensitivity studies using pseudo data	59
5.1 Generation of the pseudo data	60
5.2 Combination of both observables	61

Contents

5.3	Expectation compared to pseudo data fits	65
5.4	Effect of the correlation	68
5.5	Effect of merging the top and antitop cross sections into one observable . .	70
5.6	Combination of the top quark measurements with a B -physics measurement	73
6	Results	79
6.1	Results of the fits to real data	79
6.1.1	Combination of the W helicity measurement with the t -channel cross section measurement	80
6.1.2	Combination of the two top quark measurements with the B -physics measurement	86
6.2	Comparison with similar results setting bounds on anomalous Wtb couplings	89
6.3	Energy scale of the effective operators	93
	Summary, conclusion and outlook	97
	Appendix	101
A.1	Categories for the systematic uncertainties	101
A.2	Determination of W helicity fractions using the angular asymmetry method	111
A.3	Additional fits from the sensitivity studies	111
A.4	Additional fits for the real measurements	118
A.5	Combination of branching ratio measurements of the process $\bar{B} \rightarrow X_s \gamma$. .	122
A.6	Bounds on anomalous couplings from other measurements	123
	Bibliography	125
	Acknowledgements	137
	Erklärung	139

Introduction

Since its discovery in 1995 [1, 2], the top quark has been an interesting object in searches for physics beyond the Standard Model. Many of these searches are based on specific models, such as supersymmetry, see e.g. Reference [3]. Other interesting approaches are model independent searches. In this master of science thesis, a combination of two top quark measurements is performed to constrain the parameters of an effective field theory based on higher dimensional operators. This theory introduces four anomalous couplings at the vertex for the coupling of a top quark to a bottom quark and a W boson (called Wtb vertex): a left-handed and a right-handed vector coupling V_L and V_R , as well as a left-handed and a right-handed tensor coupling g_L and g_R . In this thesis, they are assumed to be real. In the Standard Model, these couplings have the values $V_L = V_{tb} \approx 1$ and $V_R = g_L = g_R = 0$ at tree level, where V_{tb} is the CKM matrix element at the Wtb vertex. Any deviation of these anomalous couplings from their Standard Model values would hint at physics beyond the Standard Model.

The combination makes use of Bayesian statistics, implemented in the *Bayesian Analysis Toolkit* (BAT) [4, 5]. The two combined top quark measurements are a measurement of the W helicity fractions [6] and a measurement of the t -channel single top production cross section [7], both conducted using data taken with the ATLAS detector. These observables are directly dependent on physics at the Wtb vertex [8, 9] and are therefore ideal candidates for the combination. A detailed study of the correlations between the measurements with respect to the different sources of systematic uncertainties is performed to improve the precision of the bounds on the anomalous couplings. In addition, a combination of these two top quark measurements with the measurement of the branching ratio of the process $\bar{B} \rightarrow X_s \gamma$ [10], which is also sensitive to anomalous couplings at the Wtb vertex [11], is performed. Ensemble tests are used to test the sensitivity of the combination. Four-, two-, and one-dimensional fits of the couplings are performed.

Ensemble tests show that the correlations between the systematic uncertainties of the two measurements have to be known precisely in order to perform the combination correctly.

In Chapter 1, the most important concepts of the Standard Model concerning these studies are presented, as well as the physics of the top quark, the concept of anomalous couplings in the context of effective field theory, the two top quark observables used for this combination and the experimental setup. Chapter 2 describes the two top quark measurements that will be combined: the W -helicity fraction measurement and the t -channel single top quark production cross section measurement. In addition, the sources of systematic uncertainties are categorised to allow further comparison between the two measurements. Chapter 3 describes the dependence of the top quark observables on anomalous couplings and the combination of the two measurements. Chapter 4 presents the uncertainties and the correlation matrix used for the fits in the following chapters. They are determined by the methods for the combination of the uncertainties of the two measurements described in Chapter 2 and 3. In addition, the ranges of the different fits are listed. Chapter 5 is a demonstration of the framework's capabilities using pseudo data. It contains studies on the effect of the combination of the two top quark measurements and their correlations. In addition, a study is conducted on how the combination of the two top quark measurement with the measurement of the branching ratio of the radiative B meson decay $\bar{B} \rightarrow X_s \gamma$ could improve the limits on anomalous couplings. Chapter 6 contains the result of the combination using experimental data with and without the B -physics measurement and gives a comparison to similar results. It also provides an estimation for the minimal energy at which new electroweak physics could exist. The last chapter provides a conclusion and an outlook.

1 Fundamentals

This chapter introduces the fundamental theoretical principles of the Standard Model of elementary particle physics and of anomalous top quark couplings at the Wtb vertex. It also presents the observables used for the combination, namely the W helicity fractions and the t -channel production cross section, as well as the experimental setup, namely the Large Hadron Collider and the ATLAS detector. Recent results of top quark physics are also presented in a short overview.

1.1 The Standard Model of elementary particle physics

The Standard Model of elementary particle physics (SM) is a renormalizable quantum field theory describing the elementary particles and three of their four fundamental interactions: the electromagnetic, weak and strong interactions. Up to this day, attempts to include the fourth fundamental force, gravity, in the Standard Model have failed.

The elementary particles can be grouped into 12 fermions with spin $1/2$ and 13 bosons with integer spin. The fermions can further be grouped into 3 generations, containing 2 quarks and 2 leptons each. The difference between the generations are the mass, mass related properties and properties related to the CKM matrix element (for quarks, see Section 1.1.4) of the particles. The bosons can be grouped into 12 gauge bosons with spin 1, mediating the fundamental forces of the Standard Model and the Higgs boson with spin 0 as an excitation of the Higgs field which causes most of the mass of the elementary particles. This classification of the particles within the Standard Model and their approximate masses can be seen in Figure 1.1 [12–14].

		Fermions			Bosons
		I.	II.	III.	
Quarks		u $\mathcal{O}(1 \text{ MeV})$	c $\mathcal{O}(1 \text{ GeV})$	t $\approx 173 \text{ GeV}$	γ massless
		d $\mathcal{O}(1 \text{ MeV})$	s $\mathcal{O}(100 \text{ MeV})$	b $\approx 4 - 5 \text{ GeV}$	W $\approx 80.4 \text{ GeV}$
Leptons		ν_e $\sim 0 \text{ MeV}$	ν_μ $\sim 0 \text{ MeV}$	ν_τ $\sim 0 \text{ MeV}$	Z $\approx 91.2 \text{ GeV}$
		e $\approx 511 \text{ keV}$	μ $\approx 106 \text{ MeV}$	τ $\approx 1777 \text{ MeV}$	g massless
					H $\approx 125.7 \text{ GeV}$

Figure 1.1: All elementary particles described by the Standard Model and their masses. The abbreviations are: *up quark* (u), *down quark* (d), *charm quark* (c), *strange quark* (s), *top quark* (t), *bottom quark* (b), *electron* (e), *muon* (μ), *tau lepton* (τ) the *neutrinos* belonging to the charged leptons (ν), *photon* (γ), *W boson* (W), *Z boson* (Z), *gluon* (g) and the *Higgs-boson* (H) [12, 13].

1.1.1 Fundamental Standard Model interactions and gauge bosons

Gauge bosons are the mediators of fundamental interactions and arise in the Standard Model from the assumption of local gauge invariance under a certain gauge transformation. Photons arise in the context of quantum electrodynamics (QED) by implying local U(1) gauge invariance and the eight gluons arise in the context of quantum chromodynamics (QCD) by implying local SU(3) gauge invariance. The Z boson and the two W bosons arise from the $U_Y(1) \times SU(2)$ electroweak theory, which is discussed further in Section 1.1.4. Photons were first described as quanta of an electromagnetic field by Albert Einstein in 1905 referring to results of Max Planck's work [15, 16]. The W and Z boson as they are known today were predicted in the context of the electroweak model [17–21]. They were discovered in 1983 at the UA1 and UA2 experiments at CERN [22–25]. Experimental evidence for the existence of the gluon was found for the first time in 1979 at DESY [26–29]. For simplicity, the principle of local gauge invariance is demonstrated in the context of QED [13]:

The Dirac Lagrangian

$$\mathcal{L} = \underbrace{i\bar{\psi}\gamma^\mu\partial_\mu\psi}_{\text{kinetic term}} - \underbrace{m\bar{\psi}\psi}_{\text{mass term}} \quad (1.1)$$

1.1 The Standard Model of elementary particle physics

is required to be invariant under the local U(1) gauge transformation

$$\psi \longrightarrow e^{-iq\theta(x)}\psi , \quad (1.2)$$

where ψ is a spinor field representing fermions, q is the charge of the involved fermion, corresponding to the U(1) gauge group, $\theta(x)$ is a real function of the space-time x and γ^μ ($\mu = 0, \dots, 3$) are the Dirac matrices. The mass term in Equation (1.1) is invariant under this transformation, but the kinetic term is not. To fix this, additional terms are included in the Lagrangian. The U(1)-gauge invariant Lagrangian is

$$\mathcal{L} = \underbrace{i\bar{\psi}\gamma^\mu\partial_\mu\psi - m\bar{\psi}\psi}_{\mathcal{L}_{\text{Matter}}} - \underbrace{(q\bar{\psi}\gamma^\mu\psi)A_\mu - \frac{1}{16\pi}F^{\mu\nu}F_{\mu\nu}}_{\mathcal{L}_{\text{Gauge,U(1)}}} . \quad (1.3)$$

Under the local U(1) gauge transformation, the new spin-1 field A_μ behaves like

$$A_\mu \longrightarrow A_\mu + \partial_\mu\theta(x) . \quad (1.4)$$

The last term of Equation (1.3) is the kinetic term for A_μ with $F^{\mu\nu} = \partial^\mu A^\nu - \partial^\nu A^\mu$. The particle associated with A_μ has to be massless because a mass term for A_μ would not be gauge invariant¹. Equation 1.3 can also be written as

$$\mathcal{L} = i\bar{\psi}\gamma^\mu D_\mu\psi - m\bar{\psi}\psi - \frac{1}{16\pi}F^{\mu\nu}F_{\mu\nu} , \quad (1.5)$$

with

$$D_\mu = \partial_\mu + iqA_\mu \quad (1.6)$$

being the so called *covariant derivative*. In terms of QED, Equation (1.3) describes spin 1/2 fields (fermions) interacting with Maxwell fields (photons). The charge q is the electric charge.

The strong (SU(3)) and weak (SU(2)) interaction can be described in a similar way, but with other charges and group generators. While photons and gluons have no mass, the electroweak gauge bosons W and Z have non-zero masses of [12]

$$m_W \approx 80.4 \text{ GeV} \quad \text{and} \quad m_Z \approx 91.2 \text{ GeV} . \quad (1.7)$$

As the photon couples to electric charge, the gluons couple to colour charge (red, blue,

¹A mass term can always be added by applying spontaneous symmetry breaking. Nevertheless, the gauge boson of the U(1) (namely the photon) is massless, but spontaneous symmetry breaking can be applied for the electroweak theory to assign mass to the Z and W bosons (see Section 1.1.3).

green) and the W and Z bosons couple to the third element of the weak isospin T^3 and to the weak hypercharge Y , see Table 1.1. The third element of the weak isospin, the weak hypercharge and the electromagnetic charge are connected by the relation

$$q = T^3 + \frac{Y}{2}. \quad (1.8)$$

1.1.2 Fermions

The fermions in the Standard Model are all spin-1/2 particles. They can be categorised as shown in Figure 1.1. Because parity is maximally violated in the weak interaction [30], it is necessary to treat chiral left-handed (for simplicity also called “left-handed”) and chiral right-handed (“right-handed”) fermions in a different way in the weak interaction. For the different charges of the left-handed and right-handed fermions, see Table 1.1. The left-handed quarks (up-type u_L , down-type d_L) of each generation, as well as the two left-handed leptons of each generation (charged lepton ℓ_L^- and the corresponding neutrino ν_L) are grouped in weak isospin doublets

$$Q = \begin{pmatrix} u_L \\ d_L \end{pmatrix}, \quad L = \begin{pmatrix} \nu_L \\ \ell_L^- \end{pmatrix}, \quad (1.9)$$

while the right-handed fermions are weak isospin singlets. The W bosons only couple to left-handed fermions. All right-handed particles are produced in the electromagnetic or the strong interaction because both of these interactions conserve parity. Right-handed neutrinos do not exist because they can be produced neither in the electromagnetic, nor the strong interaction. For the masses of the fermions, see Figure 1.1. Note that the quarks can only be measured in bound states (except for the top quark, see Section 1.2). Therefore, the masses of the light quarks are measured less precisely than the masses of the leptons and bosons.

Quarks Quarks participate in all interactions within the Standard Model. Their existence was proven by deep inelastic scattering experiments at the Stanford Linear Accelerator Center (SLAC) in 1968 [31–33]. The reason they also participate in the strong interaction is that quarks carry colour charge (red, blue or green), and antiquarks carry anticolour charge (antired, antiblue or antigreen). They exist in colour neutral bound states as mesons (quark and antiquark) and baryons (three quarks). Baryons and mesons are also called hadrons. The other charges of the quarks can be seen in Table 1.1, right.

Lepton	T	T ³	q	Y	Quark	T	T ³	q	Y
ν_L	1/2	1/2	0	-1	u_L	1/2	1/2	2/3	1/3
ℓ_L^-	1/2	-1/2	-1	-1	d_L	1/2	-1/2	-1/3	1/3
					u_R	0	0	2/3	4/3
ℓ_R^-	0	0	-1	-2	d_R	0	0	-1/3	-2/3

Table 1.1: Weak isospin T (with the third component T^3), electric charge q and hypercharge Y quantum numbers of leptons and quarks [14]. Additionally, quarks carry colour charge (red, green, blue), while leptons do not carry any colour charge and thus do not participate in the strong interaction.

The quarks of the first generation, the up (u) and down (d) quarks, are the lightest quarks and the building blocks of protons (uud) and neutrons (udd). Together with the down-type quark of the second generation, the strange quark, they were the quarks proposed by Gell-Mann [34] and Zweig [35, 36] in 1964. The up-type quark of the second generation, called charm quark, was proposed shortly afterwards to explain the small branching ratio of the process² $K_L \rightarrow \mu^+ \mu^-$ [38, 39]. It was discovered in 1974 as a constituent of the J/Ψ -meson at Brookhaven National Laboratory [40] and at the SPEAR storage ring at SLAC [41]. The third generation of quarks, including the down-type bottom quark and the up-type top quark, was proposed in 1973 by Kobayashi and Maskawa to explain CP violation [42]. The bottom quark was discovered in 1977 [43] and the top quark (see Section 1.2) was discovered in 1995 [1, 2], both of them at FERMILAB.

Leptons In contrast to quarks, leptons do not carry any colour charge and thus do not participate in the strong interaction. The charged leptons have electric charges of -1 and the neutrinos are electrically neutral. The other charges of leptons can be seen in Table 1.1, left. In the simplest version of the Standard Model, neutrinos are assumed to be massless. Nevertheless, neutrinos have in fact a very small mass, which is discussed in Section 1.1.5.

J.J. Thompson is often credited for the discovery of the electron in 1897 [44], which is the charged lepton of the first generation. The corresponding electron neutrino was proposed by Wolfgang Pauli to be able to describe the nuclear beta decay in an energy, momentum and spin conserving theory [45, 46]. It was finally discovered in 1956 by

²This small branching ratio is explained by the GIM (Glashow, Iliopoulos and Miani) mechanism: Without the charm quark, the leading order diagram of the process $K_L \rightarrow \mu^+ \mu^-$ is a box diagram with an up quark in the loop and the exchange of two W bosons. Introducing an additional box diagram with a charm quark instead of the up quark almost cancels the contribution of the first diagram to the branching ratio and explains its low value [37, 38].

1 Fundamentals

Clyde Cowan and Frederick Reines in a nuclear reactor experiment [47]. The charged lepton of the second generation, called muon, was discovered in 1936 by experiments with cosmic radiation [48, 49]. The corresponding muon neutrino was discovered in 1962 by Leon M. Lederman, Melvin Schwartz and Jack Steinberger at the Alternating Gradient Synchrotron (AGS) of the Brookhaven National Laboratory [50]. The tau lepton, being the third charged lepton, was discovered around 1975 at the SPEAR collider at SLAC [51]. The corresponding tau neutrino was discovered at the DONUT experiment at FERMILAB in the year 2000 [52].

1.1.3 Mass generation with a toy theory

Lagrangians describing massive gauge bosons have to contain mass terms. This is the case for the massive electroweak gauge bosons W and Z . Simply including a mass term as a term of second order in the gauge field would violate local gauge invariance. Assuming a toy theory $U(1)$ including a massive photon, it can easily be seen that a mass term

$$\mathcal{L}_{\text{mass}} = \frac{m^2}{8\pi} A_\mu A^\mu \quad (1.10)$$

would violate local $U(1)$ gauge invariance. The same holds for all other Standard Model symmetries. In addition, mass terms for fermions also violate local $U_Y(1) \times SU(2)$ invariance, because they couple left-handed to right-handed fields.

Including local gauge invariant mass terms is achieved by applying spontaneous symmetry breaking to the respective Standard Model symmetry. Returning to the massive $U(1)$ toy theory, assume a complex scalar field $\phi(x) = \phi_1(x) + i\phi_2(x)$ that is invariant under local $U(1)$ transformations. The Lagrangian of this scalar field can be written as

$$\mathcal{L}_{\text{toy}} = \frac{1}{2} (D_\mu \phi)^* (D^\mu \phi) - \underbrace{\left(-\frac{1}{2} \mu^2 (\phi^* \phi) + \frac{1}{4} \lambda^2 (\phi^* \phi)^2 \right)}_{V(\phi)}, \quad (1.11)$$

where D_μ is the covariant derivative for the $U(1)$ and $V(\phi)$ is the potential, which is minimal at $v := |\phi| = \mu/\lambda$ for $\mu^2 > 0$ and $\lambda^2 > 0$. The minimum v is also called *vacuum expectation value* (VEV). To be able to apply perturbative calculus, it is necessary to transform the origin of the coordinate system into the minimum of the potential by the relations

$$\phi_1(x) = h(x) + v, \quad \phi_2(x) = \xi(x). \quad (1.12)$$

1.1 The Standard Model of elementary particle physics

Around the origin of this new coordinate system, the potential is not invariant under local U(1) transformation. This is called *spontaneous symmetry breaking*. Writing Equation (1.11) in the coordinates of 1.12, a scalar field $h(x)$ with the mass $m_h = \sqrt{2}\mu$ and a massless scalar field, called Goldstone boson, arises. Because it is massless, the Goldstone boson would always be easily detectable. Nevertheless, in case of the “realistic” theory of electroweak symmetry breaking, it does not exist because it would have been already discovered. This problem can be solved by using the local gauge invariance of the Lagrangian and implying the transformation

$$\phi \rightarrow e^{-i\xi(x)/v} \phi , \quad (1.13)$$

which causes the Goldstone boson to vanish from the Lagrangian. This is called unitary gauge. The scalar field couples to the U(1) gauge boson via the covariant derivative. Therefore, if the mass term for the massive boson would be

$$\mathcal{L}_{\text{mass}} = \frac{1}{2}(qv)^2 A_\mu A^\mu . \quad (1.14)$$

This term looks like Equation (1.10) with a mass of $m = 2\sqrt{\pi} qv$ but is invariant under local U(1) transformations. The degree of freedom from the Goldstone boson is now the longitudinal degree of freedom of the massive gauge boson of the toy theory U(1) [13].

The same mechanism can be applied to the electroweak model in which it is used to describe the massive W and Z gauge bosons. The field ϕ has to be a complex doublet, which is referred to as the *Higgs field*. The three Goldstone bosons arising can be gauged away by implying local SU(2) invariance. The Higgs doublet for the electroweak symmetry breaking is [53–56]

$$\phi(x) = \frac{1}{\sqrt{2}} \begin{pmatrix} 0 \\ v + h(x) \end{pmatrix} . \quad (1.15)$$

The vacuum expectation value is determined as $v \approx 246$ GeV [12] via $v = (\sqrt{2}G_F)^{-2}$, where G_F is the Fermi coupling constant [37]. The mass generation for the W and Z bosons via spontaneous electroweak symmetry breaking while avoiding massless Goldstone bosons is also referred to as the *Higgs mechanism*³. The scalar field $h(x)$ plays the role of the Higgs boson in the electroweak symmetry breaking. The Higgs boson was discovered in 2012 by the ATLAS and CMS collaborations [57, 58].

³Actually, there is no exact definition which part of this mechanism the Higgs mechanism actually is.

1.1.4 The electroweak model within the Standard Model

Also known as the Glashow-Salam-Weinberg model [17–21], the electroweak model is the unification of the electromagnetic and the weak interaction. The resulting gauge bosons are the massless photon, as well as the massive W and Z gauge bosons. It is based on a $U_Y(1) \times SU(2)$ symmetry, where the $U_Y(1)$ is not to be confused with the $U(1)$ from QED. The charge corresponding to the $U_Y(1)$ group is the weak hypercharge Y , while the charge corresponding to the $SU(2)$ is the third element of the weak isospin T^3 , see Table 1.1 and Equation 1.8.

As for the $U(1)$ group in Section 1.1.1, it is possible to construct a local $U_Y(1) \times SU(2)$ gauge invariant Lagrangian by imposing local gauge invariance under transformation of the fermionic fields like

$$\psi \rightarrow \underbrace{\exp\left(i\frac{g'}{2}Y\alpha(x)\right)}_{U_Y(1) \text{ part}} \underbrace{\exp\left(ig\vec{\tau}\cdot\vec{\Lambda}(x)\right)}_{SU(2) \text{ part}} \psi, \quad (1.16)$$

where g' is the coupling strength corresponding to the $U_Y(1)$ group, g is the coupling strength corresponding to the $SU(2)$ group and $\vec{\tau}$ are the Pauli matrices as the generators corresponding to the $SU(2)$ group. The $SU(2)$ part represents a local rotation of the weak isospin T . Note that the $U_Y(1)$ group and the $SU(2)$ group are still “separated”. The $1/2$ and the switch of the sign in the exponent of the $U_Y(1)$ part in comparison to Equation (1.2) are conventional. It is obvious that left-handed fermionic fields transform differently than right-handed fields under this symmetry due to their different charges. The corresponding covariant derivative is

$$D_\mu = \partial_\mu + i\frac{g'}{2}Y B_\mu + ig\vec{\tau}\cdot\vec{W}_\mu, \quad (1.17)$$

where B_μ is the gauge field corresponding to the $U_Y(1)$ and W_1 , W_2 and W_3 are the gauge fields corresponding to the $SU(2)$ group.

Up to this point, all gauge fields are still massless. To assign mass to the gauge field, it is necessary to impose electroweak symmetry breaking like it is sketched in Section 1.1.3. The coupling of the Gauge fields to the Higgs field (for $h(x) = 0$) emerges from the

covariant derivative like in Equation (1.11)

$$\begin{aligned} & \left| \left(-i\frac{g}{2}\vec{\tau} \cdot \vec{W}_\mu - i\frac{g'}{2}B_\mu \right) \phi \right|^2 \\ &= \left(\frac{1}{2}vg \right)^2 W_\mu^+ W^{-\mu} + \frac{1}{8}v^2 \left(W_\mu^{(3)}, B_\mu \right) \begin{pmatrix} g^2 & -gg' \\ -gg' & g'^2 \end{pmatrix} \begin{pmatrix} W^{\mu(3)} \\ B^\mu \end{pmatrix}, \end{aligned} \quad (1.18)$$

with

$$W_\mu^\pm = 1/\sqrt{2} \left(W_\mu^{(1)} \pm iW_\mu^{(2)} \right). \quad (1.19)$$

To obtain a massless eigenstate for the photon and a massive eigenstate for another neutral boson (the Z boson), a rotation via the electroweak mixing angle θ_W , also called Weinberg angle, is necessary

$$\begin{aligned} A_\mu &= \cos \theta_W B_\mu + \sin \theta_W W_\mu^{(3)}, \\ Z_\mu &= -\sin \theta_W B_\mu + \cos \theta_W W_\mu^{(3)}, \end{aligned} \quad (1.20)$$

with $\tan \theta_W = g'/g$ and $\sin^2 \theta_W \approx 0.23$ [12]. The masses of the massive gauge bosons are

$$M_W = \frac{1}{2}vg \quad \text{and} \quad M_Z = \frac{1}{2}v\sqrt{g^2 + g'^2}. \quad (1.21)$$

Making use of the electroweak properties of the Higgs field, gauge invariant mass terms for the fermions can be constructed via Yukawa couplings to the Higgs field. The mass eigenstates of the quarks are not the same as their weak eigenstates. This is described by the CKM matrix which allows flavour changing charged currents across quark generations. The probability of the transition of a quark of the flavour x to the flavour y depends on the CKM matrix element V_{xy} . The 3×3 -dimensional structure of the unitary CKM matrix allows CP violation due to complex phases [42].

1.1.5 Limitations of the Standard Model

There are many phenomena that are not described by the current form of the Standard Model. The most popular ones are listed here [3, 12, 13, 59].

- Dark Matter: There are many hints due to gravitational behaviour that stable matter exists in the Universe which interacts mostly via gravity and not via the electromagnetic or strong interaction. Therefore, it is hard to detect. A possible candidate for dark matter is for example the lightest supersymmetric particle from supersymmetric theories.
- Higgs boson mass: Due to fermionic loop corrections, the mass of the Higgs boson at $\mathcal{O}(100 \text{ GeV})$ is purely accidental in the Standard Model. In the Standard Model, the bare mass and the loop corrections almost cancel but not completely, which causes this relatively low value. Supersymmetric models cancel these loop corrections by introducing a fermionic partner for each boson as well as a bosonic partner for each fermion. Proving supersymmetry right would give a natural explanation of the relatively low Higgs boson mass.
- Grand Unification: From an aesthetic point of view, all three gauge couplings should unite at a higher mass scale. This feature is not provided by the Standard Model, but by many of its extensions.
- Gravity: Gravity is the only fundamental force that is not included in the Standard Model. This is because there is no known way to describe general relativity consistently in quantum field theory and gravity does not play a role in current collider based experiments.
- Origin of electroweak symmetry breaking: Although electroweak symmetry breaking describes mass generation in the Standard Model, the origin of the breaking itself is still unknown.
- Neutrino masses and oscillation: There is experimental evidence that neutrinos in fact have mass. Assigning this mass to neutrinos, it is necessary to introduce new mechanisms to the Standard Model. Similar to the quarks, neutrino mass eigenstates are not their weak interaction eigenstates which leads to neutrino flavour oscillation. A further question closely related to the fact that neutrinos have non-zero mass is if neutrinos follow Dirac or Majorana statistics. The Majorana statistic implies that neutrinos would be their own antiparticles.

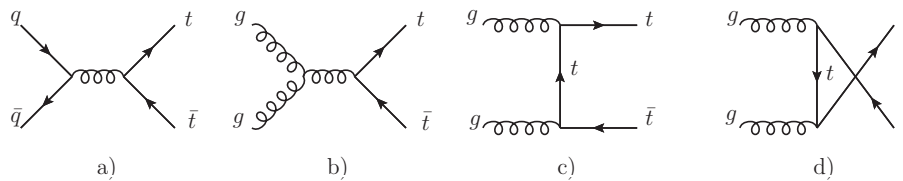


Figure 1.2: Leading order Feynman diagrams for the top quark pair production at hadron colliders. Diagram a) is called quark-antiquark annihilation. It was a dominant production mechanism at the TEVATRON. Diagrams b), c) and d) are gluon-gluon fusion processes, which are typical production mechanisms at the LHC.

1.2 The top quark

The top quark was discovered in 1995 by the CDF and DØ experiments at the TEVATRON proton-antiproton collider at a centre-of-mass energy of 1.8 TeV [1, 2]. With a mass of $173.34 \pm 0.27(stat.) \pm 0.71(syst.)$ GeV [60], it is the heaviest known elementary particle. It is assumed to be the third generation up-type quark, although the weak isospin of the top quark has not been measured yet. Its mass yields a Yukawa coupling to the Higgs field of almost unity⁴ which makes it an interesting candidate for investigating the electroweak symmetry breaking mechanism. The top quark is part of many theories of physics beyond the Standard Model as a decay product of “new” particles⁵ or as a particle that decays into “new” particles. Its mass, together with the W boson mass and the Higgs boson mass, can be used to probe the vacuum stability of the Standard Model at high energy scales [12, 61]. The only machine in service being capable of producing top quarks is the Large Hadron Collider (LHC) which is often referred to as a “top quark factory”, because it produced around one million top quarks during the 7 TeV run and around ten million top quarks during the 8 TeV run. Together with the TEVATRON, these were the only machines ever built being able to produce top quarks [12, 61].

Top quark decay Due to the high mass of the top quark, its lifetime of approximately 0.5×10^{-24} s is much shorter than the time of hadronisation of approximately 10^{-23} s [62]. Therefore, it decays before forming bound hadronic states and can be studied as a “bare” quark. It is the only quark that decays into a real W boson because the W boson is lighter than the difference of the top quark mass and the other decay product (the bottom quark). Because the element V_{tb} of the CKM matrix is almost unity, the top quark decays almost 100% of the time into a W boson and a bottom quark while the decay channels into a W

⁴The Yukawa coupling of fermions to the Higgs field is $g_f = \sqrt{2} \cdot m_f/v$, where m_f is the fermion mass and v is the vacuum expectation value of the Higgs field [37].

⁵In this context, “new particles” means particles only described by theories beyond the Standard Model.

boson and a down quark or a strange quark are heavily suppressed. With this assumption, the Lagrangian for the top quark decay vertex in the Standard Model can be written as

$$\mathcal{L} = -\frac{g}{\sqrt{2}} \bar{b} \gamma^\mu V_{tb} P_L t W_\mu^- + \text{h.c.} , \quad (1.22)$$

with the left-handed projection operator P_L . The fields for the top quark, the bottom quark and the W boson are represented by t , b and W_μ^- . The vertex described by this Lagrangian in the Standard Model is called the Wtb vertex. This vertex is not only present in the top quark decay, but in every process that involves a coupling of a top quark, a bottom quark and a W boson, for example electroweak top quark production, see Section 1.5 [12, 61].

Top quark pair production Top quark pair production occurs via the strong interaction in gluon-gluon fusion and quark-antiquark annihilation, see Figure 1.2. It was not yet possible to reach high enough energies at electron-positron-colliders to produce top quark pairs, so they were not yet produced in pairs via the electroweak interaction. At the TEVATRON, approximately 85% of the top quark pairs were produced via quark-antiquark annihilation. At higher centre-of-mass-energies the fraction of gluons contribute more and more to the parton density functions. Therefore at the LHC, approximately 80% (90%) of all top pairs are produced via gluon-gluon fusion at a centre-of-mass energy of 7 TeV (14 TeV).

The W boson can decay into quarks or leptons. Therefore, there are three kinds of decay channels for top pair events: The all-jets channel includes only jets emerging from six quarks in the final state of which two jets are b -jets⁶. The lepton+jets channel includes jets from four quarks of which two are b -jets, a charged lepton and large missing transverse momentum from the corresponding neutrino. The dilepton channel includes two b -jets and two charged leptons as well as large missing transverse momentum from both W bosons decaying leptonically. The ratio between the probabilities of this channels is⁷ 45.7% : 43.8% : 10.5% (all-jets : lepton+jets : dilepton). Figure 1.3 shows the prediction for the top-pair production cross section as a function of the centre-of-mass energy for proton-proton and proton-antiproton collisions compared to the latest experimental LHC and TEVATRON results [12, 61]. The latest LHC combination result for $\sqrt{s} = 8$ TeV, using ATLAS and CMS data (using 20.3 fb^{-1} and 5.3 fb^{-1} of data, respectively) is $\sigma(tt) = 241.5 \pm 8.5 \text{ pb}$ [70].

⁶ b -jets are jets originating from a decaying hadron containing a bottom quark.

⁷It is possible that the hadronic decay of a tau lepton looks like the hadronic decay of a W boson and therefore a dileptonic (lepton+jets) event is interpreted as lepton+jets (all-jets) event.

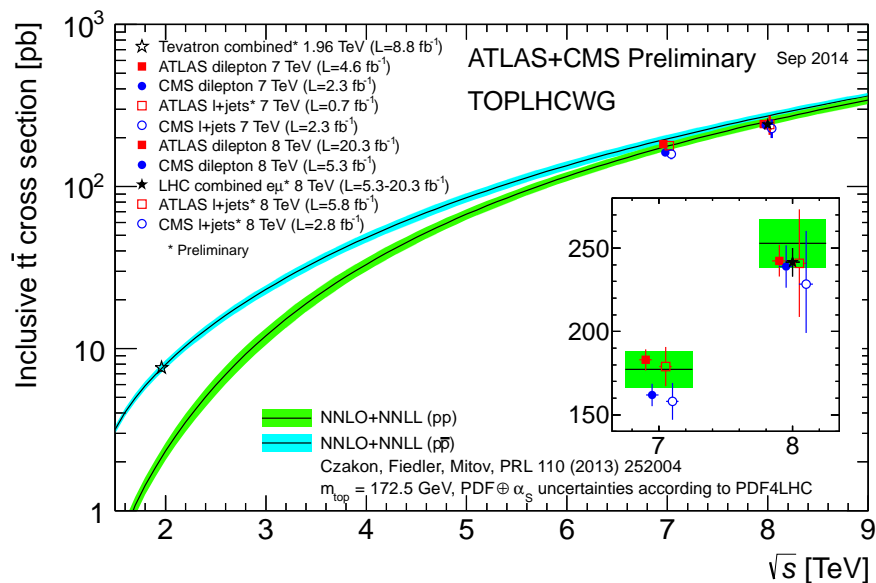


Figure 1.3: Theory prediction of the top quark pair production cross section in proton-proton and proton-antiproton collisions in dependence on the centre-of-mass energy \sqrt{s} and in comparison to LHC and TEVATRON results [63–73].

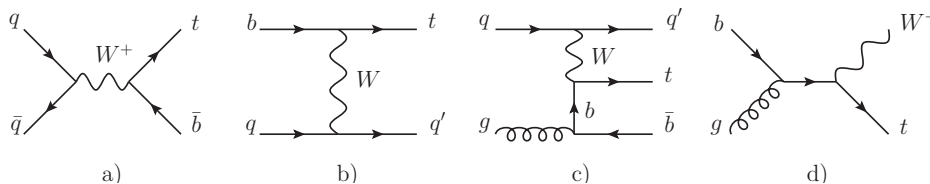


Figure 1.4: The single top quark production mechanisms: a) s -channel, b) t -channel $2 \rightarrow 2$, c) t -channel $2 \rightarrow 3$ and d) W -associated production.

Single top quark production The cross section for single top quark production is much lower than that for top quark pair production, because single top quarks are produced via the charged current weak interaction, see Figure 1.4. The three production channels are the s -channel, t -channel and the W -associated production channel. In all processes, $|V_{tb}|$ from the CKM matrix element is directly involved. The single top quark production cross sections in the different channels in dependence on the centre-of-mass energy and in comparison to the results of ATLAS measurements are shown in Figure 1.5. The approximate next-to-next-to leading order (NNLO) predictions for the single top cross

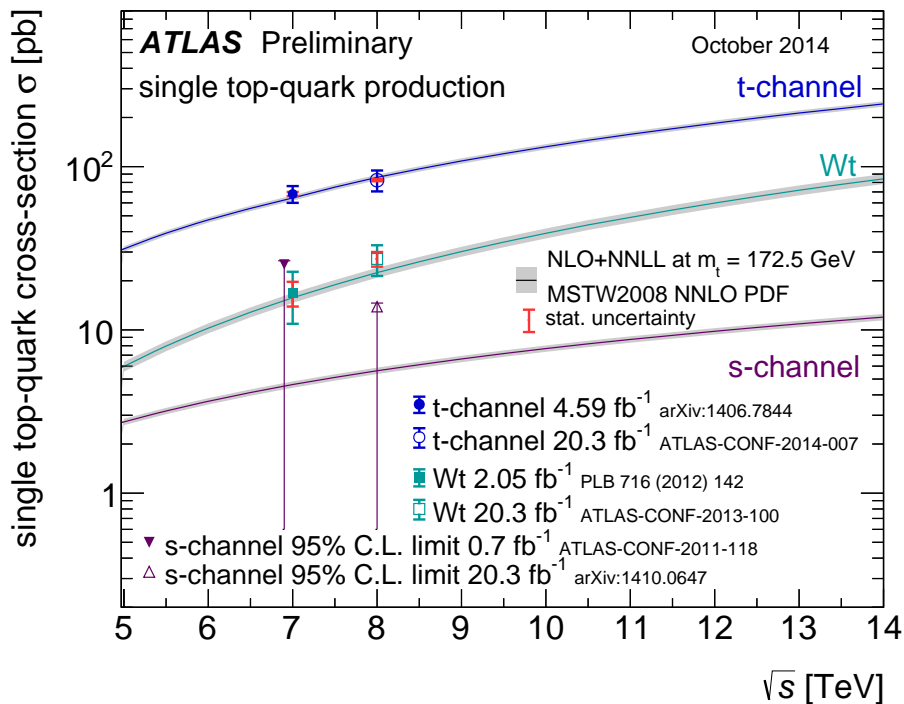


Figure 1.5: Theory prediction of the single top quark production cross sections in the different channels in dependence on the centre-of-mass energy \sqrt{s} and in comparison to the results of ATLAS measurements [7, 78–83].

sections in proton-proton collisions at a centre-of-mass energy of $\sqrt{s} = 7$ TeV are [74–76]

$$\sigma(t\bar{b}) = 3.1 \pm 0.1 \text{ pb} , \quad (1.23)$$

$$\sigma(\bar{t}b) = 1.4 \pm 0.1 \text{ pb} , \quad (1.24)$$

$$\sigma(tq) = 41.9_{-0.8}^{+1.8} \text{ pb} , \quad (1.25)$$

$$\sigma(\bar{t}q) = 22.7_{-1.0}^{+0.9} \text{ pb} , \quad (1.26)$$

$$\sigma(Wt) = 15.7 \pm 1.1 \text{ pb} , \quad (1.27)$$

where (1.23) and (1.24) are s -channel cross sections, (1.25) and (1.26) are t -channel cross sections (but only for the diagram 1.4 b)) and (1.27) is the cross section for the associated W production. The s -channel production was recently observed by the CDF and DØ collaborations at FERMILAB at $\sqrt{s} = 1.96$ TeV with a cross section of $\sigma_s = 1.29_{-0.24}^{+0.26}$ pb [77]. It has not yet been observed at the LHC, see Section 1.5. The W associated production (at ATLAS using 7 TeV data) was measured with a cross section of $\sigma_{Wt} = 16.8 \pm 2.9$ (stat) ± 4.9 (syst) pb [78]. The t -channel cross section is explained in further detail in Section 1.5. Its latest ATLAS measurement is described in Section 2.2 [12, 61].

1.3 Anomalous couplings at the Wtb vertex

Although the Standard Model is a very successful concept, the limitations described in Section 1.1.5 indicate that new particles and interactions exist at a yet inaccessible mass scale Λ below the Planck scale ($\sim 10^{19}$ GeV). In this case, the Standard Model only describes physics well up to the mass scale yet accessible. For higher energies, it becomes an effective low-energy theory where the heavy fields are integrated out. Physics up to energies of the order of Λ can then be described by an effective Lagrangian, like in the case of Fermi's interaction⁸ [45, 46]. Such a Lagrangian has to be invariant under Standard Model transformations and has to obey the known conservation laws. This effective Lagrangian can be expressed at mass scales accessible to current experiments as

$$\mathcal{L}_{\text{eff}} = \mathcal{L}_{\text{SM}} + \frac{1}{\Lambda} \mathcal{L}_1 + \frac{1}{\Lambda^2} \mathcal{L}_2 + \dots, \quad (1.28)$$

where \mathcal{L}_{SM} is the dimension-four Standard Model Lagrangian, containing the Standard Model gauge fields, Standard Model fermion fields, one Higgs doublet and their couplings. The Lagrangian \mathcal{L}_1 is of dimension five and \mathcal{L}_2 is of dimension six etc. [84].

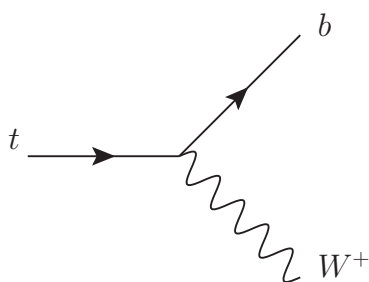


Figure 1.6: Feynman diagram of the Wtb vertex.

Because the mass of the top quark is higher than the mass of all other Standard Model fermions, it is expected that effective interactions of the top quark are much more sensitive to physics at higher mass scales than the effective interactions of other Standard Model fermions. Within this effective field theory, it is possible to construct a Lagrangian describing new physics occurring at energies much greater than 1 TeV introducing anomalous couplings at the vertex for the coupling of a top quark to a bottom quark and a W boson (called Wtb vertex, see Figure 1.6). The only term allowed by gauge invariance of dimension five from Equation (1.28) describes the Majorana mass terms for neutrinos [84]. Therefore, the Lagrangian for anomalous couplings at the Wtb vertex contains only additional terms of dimension six and higher. Because the mass scale Λ is expected to be large, all terms of a higher dimension than dimension six are not considered here [85]. The five dimension-six operators that have significant effects at order $1/\Lambda^2$ on anomalous couplings at the Wtb

⁸Fermi's interaction is a low-energy description of the weak interaction.

1 Fundamentals

vertex are [9, 86]

$$O_{\phi q}^{(3)} = i(\phi^\dagger \tau^I D_\mu \phi) (\bar{q}_L \gamma^\mu \tau^I q_L) , \quad (1.29)$$

$$O_{\phi\phi} = i(\tilde{\phi}^\dagger D_\mu \phi) (\bar{t}_R \gamma^\mu b_R) , \quad (1.30)$$

$$O_{uW} = (\bar{q}_L \sigma^{\mu\nu} \tau^I t_R) \tilde{\phi} W_{\mu\nu}^I , \quad (1.31)$$

$$O_{dW} = (\bar{q}_L \sigma^{\mu\nu} \tau^I b_R) \phi W_{\mu\nu}^I , \quad (1.32)$$

$$O_{qW} = (\bar{q}_L \gamma^\mu \tau^I D^\nu q_L) W_{\mu\nu}^I , \quad (1.33)$$

where q_L is the left-handed quark doublet of the 3^{rd} generation, b_R and t_R are the right-handed bottom- and top quark singlets. The field ϕ ($\tilde{\phi} = i\tau^2 \phi^*$) is the Higgs boson doublet. D_μ is the covariant derivative including the Standard Model gauge fields. $W_{\mu\nu}^I = \partial_\mu W_\nu^I - \partial_\nu W_\mu^I + g\epsilon_{IJK} W_\mu^J W_\nu^K$ is the W boson field strength [85]. τ^I ($I = 1, 2, 3$) are the Pauli matrices and $\sigma^{\mu\nu} = i/2(\gamma^\mu \gamma^\nu - \gamma^\nu \gamma^\mu)$, where γ^μ ($\mu = 0, \dots, 3$) are the Dirac matrices. The Lagrangian from Equation (1.28) can be written in a different form for the Wtb vertex [8]:

$$\begin{aligned} \mathcal{L} = & -\frac{g}{\sqrt{2}} \bar{b} \gamma^\mu (V_L P_L + V_R P_R) t W_\mu^- \\ & -\frac{g}{\sqrt{2}} \bar{b} \frac{i\sigma^{\mu\nu} q_\nu}{M_W} (g_L P_L + g_R P_R) t W_\mu^- + \text{h.c.} , \end{aligned} \quad (1.34)$$

with the left- and right-handed projection operators P_L and P_R and $q = p_t - p_b$. The coefficients V_L and V_R describe the left- and right-handed vector couplings, g_L and g_R describe the left- and right handed tensor couplings and M_W is the W boson mass. The Standard Model values at tree level are

$$V_L = V_{tb} \approx 1 \quad \text{and} \quad V_R = g_L = g_R = 0 , \quad (1.35)$$

where V_{tb} is the CKM matrix element for the Wtb vertex. Deviations from these values emerge within the Standard Model at the one loop level [87] but are small enough to be neglected. The deviations from the Standard Model values of V_L , V_R , g_L and g_R in terms of dimension-six operators can be written as [9, 84, 86]

$$\begin{aligned} \delta V_L &= \left(C_{\phi q}^{(3)*} + \frac{g}{2} \text{Re} C_{qW} \right) \frac{v^2}{\Lambda^2} , & \delta g_L &= \sqrt{2} C_{dW}^* \frac{v^2}{\Lambda^2} , \\ \delta V_R &= \frac{1}{2} C_{\phi\phi}^* \frac{v^2}{\Lambda^2} , & \delta g_R &= \sqrt{2} C_{uW} \frac{v^2}{\Lambda^2} , \end{aligned} \quad (1.36)$$

where $C_{\phi q}^{(3)}$, $C_{\phi\phi}$, C_{uW} , C_{dW} , and C_{qW} are the coefficients⁹ corresponding to the dimension-

⁹The contribution of the dimension-six operator O_{xy} to the dimension-six Lagrangian \mathcal{L}_2 is $C_{xy} O_{xy}$.

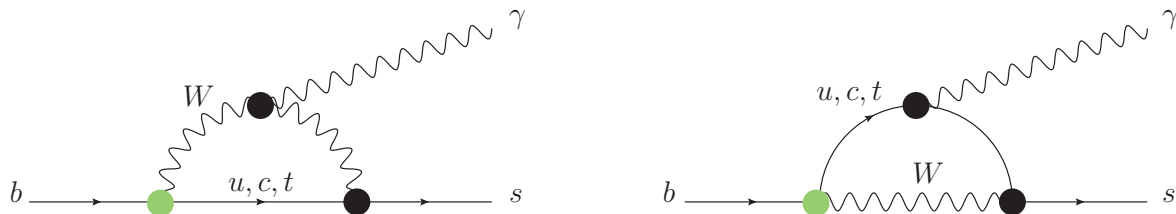


Figure 1.7: The Feynman diagrams of the two possible leading order processes for the decay $b \rightarrow s\gamma$ within the Standard Model. In the case of a top quark running inside the loop, the green dots mark the Wtb vertices within these Feynman diagrams.

six operators (1.29) - (1.33). For the following investigations, V_L , V_R , g_L and g_R are assumed to be real.

Anomalous Wtb couplings can be probed in the measurements of top quark decay and production processes, as well as in B -physics measurements. The top quark observables that can be used for probing these anomalous couplings are for instance single top quark cross sections, W boson helicity fractions and ratios, angular asymmetries related to the W helicity fractions, the energy distribution of the charged lepton from the W decay and CP-violation asymmetries in the top quark decay [8, 86]. Possible measurements from B -physics for probing anomalous Wtb couplings are $B_{d,s} - \bar{B}_{d,s}$ oscillation observables, the branching ratios of $B_s \rightarrow \mu^+\mu^-$ and $B \rightarrow K^{(*)}\nu\bar{\nu}$, the forward-backward asymmetry in $B \rightarrow K^*l^+l^-$, as well as observables from the $B \rightarrow X_sl^+l^-$ and $B \rightarrow X_s\gamma$ decay modes [11, 88]. In this thesis, the measurement of the branching ratio of the process $\bar{B} \rightarrow X_s\gamma$ is used to further constrain anomalous Wtb couplings. Because flavour changing neutral currents at tree level are not allowed in the Standard Model, the leading order of the corresponding process $b \rightarrow s\gamma$ is the one-loop level. This loop can contain a Wtb vertex with a virtual top quark and a virtual W boson, see Figure 1.7. For further explanation, see Section 5.6. The Feynman diagrams of the other B -physics processes mentioned here also include Wtb vertices with virtual particles.

The latest ATLAS results for anomalous couplings at the Wtb vertex derived by a W boson helicity measurement at a centre-of-mass energy of $\sqrt{s} = 7$ TeV [89] are

$$\begin{aligned} \text{Re}(V_R) &\in [-0.20, 0.23] , \\ \text{Re}(g_L) &\in [-0.14, 0.11] \quad \text{and} \\ \text{Re}(g_R) &\in [-0.08, 0.04] , \end{aligned}$$

at 95% C.L., taking only one of the couplings non-zero at a time. See Figure 1.8 for the two-dimensional fit in the g_L - g_R plane. The two-dimensional limits on g_L and g_R from the latest LHC combination at $\sqrt{s} = 7$ TeV are shown in Figure 1.9 [89–92].

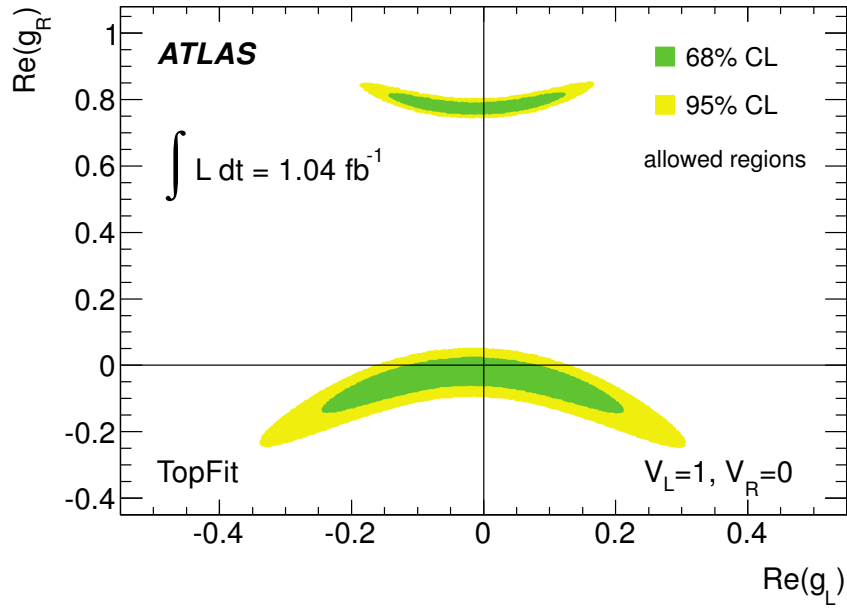


Figure 1.8: Allowed regions for the anomalous couplings g_L and g_R from the latest W helicity measurement from the ATLAS collaboration [89]. The vector couplings are fixed to $V_L = 1$ and $V_R = 0$. In the notation of this report, $\text{Re}(g_L)$ corresponds to g_L and $\text{Re}(g_R)$ corresponds to g_R .

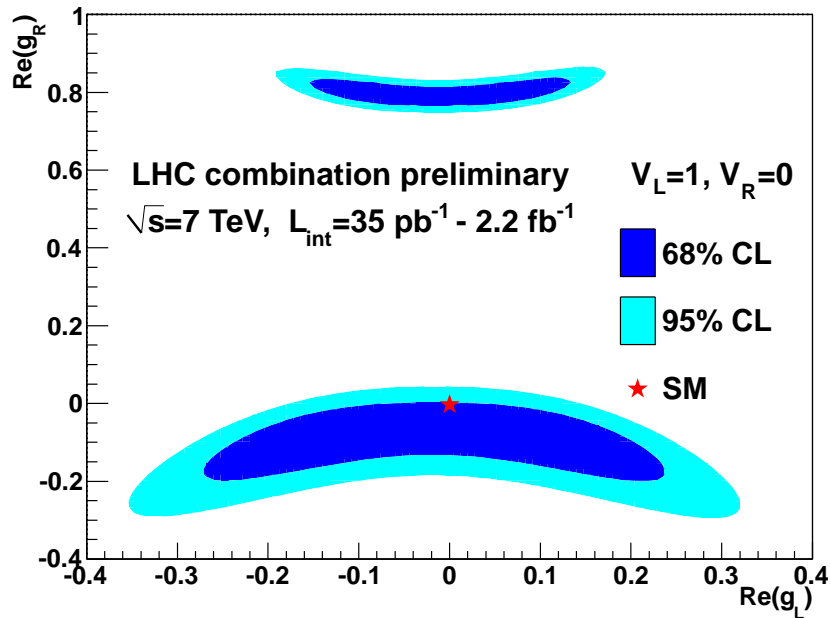


Figure 1.9: Allowed regions for the anomalous couplings g_L and g_R from the latest LHC combination of W helicity measurements at $\sqrt{s} = 7$ TeV [89–92]. The vector couplings are fixed to $V_L = 1$ and $V_R = 0$. In the notation of this report, $\text{Re}(g_L)$ corresponds to g_L and $\text{Re}(g_R)$ corresponds to g_R .

1.4 W helicity fractions

The top quark decays at almost 100% of the time into a bottom quark and a real W boson via the electroweak interaction. This interaction has a (V - A) structure¹⁰. The polarisation (helicity) of the produced W boson can be longitudinal, left-handed or right-handed. The fractions of W bosons produced in top quark decays with a certain polarisation are called *W helicity fractions*. The longitudinal, left-handed and right-handed W helicity fractions are denoted as F_0 , F_L and F_R . In the Standard Model, the fraction of top quarks decaying into longitudinally polarised W bosons increases for a bigger Yukawa coupling of the top quark to the Higgs field due to the *Goldstone boson equivalence theorem*¹¹ [93–95]. Therefore, a higher top quark mass results in a higher longitudinal W helicity fraction. The helicity fractions in the Standard Model are [12]

$$F_L \approx \frac{2 \frac{m_W^2}{m_t^2}}{1 + 2 \frac{m_W^2}{m_t^2}} \approx 30\% , \quad F_0 \approx \frac{1}{1 + 2 \frac{m_W^2}{m_t^2}} \approx 70\% , \quad F_R \approx 0\% , \quad (1.37)$$

assuming the mass of the bottom quark to be approximately zero compared to the top quark mass. The next-to-next-to-leading order predictions for the W helicity fractions are $F_0 = 0.687 \pm 0.005$, $F_L = 0.311 \pm 0.005$ and $F_R = 0.0017 \pm 0.0001$ [96].

Considering only the leptonic decays of the W boson, its helicity fractions are determined by the distribution of the decay products of the top quark:

$$\frac{1}{\sigma} \frac{d\sigma}{d \cos \theta^*} = \frac{3}{4}(1 - \cos^2 \theta^*) F_0 + \frac{3}{8}(1 - \cos \theta^*)^2 F_L + \frac{3}{8}(1 + \cos \theta^*)^2 F_R , \quad (1.38)$$

where θ^* is the angle between the momentum direction of the charged lepton from the W decay and the reversed momentum direction of the bottom quark from the same top quark in the W boson rest frame [89, 97].

The different helicity arrangements for the W helicity fractions can be seen in Figure 1.10. The positively charged lepton from the decay of the W^+ is always right-handed because of the (V - A) structure of the decay. In addition, the z -components of the spin of the charged lepton and the neutrino have to sum up to spin 1 (the spin of the W boson). If

¹⁰The weak vertex factor contains the term $\gamma^\mu(1 - \gamma^5)$, where γ^μ are the so called *Dirac matrices* ($\mu = 0, \dots, 3$). The term γ^μ represents a vector coupling, whereas the term $\gamma^\mu\gamma^5$ represents an axial vector coupling. Therefore, “(V - A)” stands for “vector-minus-axial-vector coupling” [13].

¹¹The Goldstone bosons, turned into the longitudinal polarization mode of the massive gauge bosons by the Higgs mechanism, still influence the amplitude for emission and absorption of longitudinal polarized gauge bosons in the high-energy limit [93].

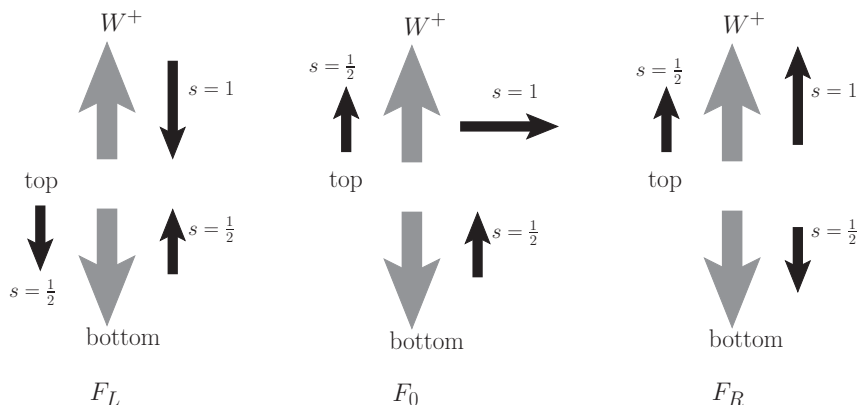


Figure 1.10: Helicity arrangement in the top quark rest frame for the different W boson helicity fractions [97]. The grey arrows indicate the momentum directions of the particles, while the black arrows indicate their spin orientations.

the W^+ -boson from the top decay is polarised left-handedly, the charged lepton is emitted dominantly in the opposite direction of the momentum direction of the W^+ boson in the W rest frame¹². Therefore, the momentum direction of the charged lepton should be dominantly the same as the momentum direction of the bottom quark from the same top quark decay in the W rest frame. This causes $(1 - \cos \theta^*)^2$ to be maximal. If the W^+ -boson from the top decay is polarised right-handedly, the charged lepton is emitted dominantly in the momentum direction of the W^+ boson in the W -bosons rest frame. Therefore, the momentum direction of the charged lepton should be dominantly the opposite of the momentum direction of the bottom quark from the same top quark decay in the W rest frame. This causes $(1 + \cos \theta^*)^2$ to be maximal. Because the bottom quark mass is very small compared to the top quark mass and the bottom quark is required to be right-handed¹³, this W helicity fraction is approximately zero in the Standard Model. If the W^+ -boson from the top decay is longitudinally polarised, the charged lepton is emitted dominantly in a 90° angle with respect to the momentum direction of the W^+ boson in the W rest frame. Therefore, the momentum direction of the charged lepton and the momentum direction of the bottom quark from the same top quark decay should be dominantly in a 90° angle in the W rest frame, which causes $(1 - \cos^2 \theta^*)$ to be maximal [89, 97].

Because the observed W boson emerges from the top quark decaying into a bottom

¹²Here “the momentum direction of the W boson in the W rest frame” means the momentum direction of the W boson which is not completely in the W rest frame, but an infinitesimal amount boosted towards the top quark rest frame to be able to refer to a momentum direction of the W boson.

¹³In the Standard Model, the bottom quark is produced with a left-handed helicity in the top quark rest frame due to the $(V - A)$ structure of the Wtb vertex. Nevertheless, due to its mass the bottom quark can undergo a spin flip, allowing a non-zero right-handed W helicity fraction.

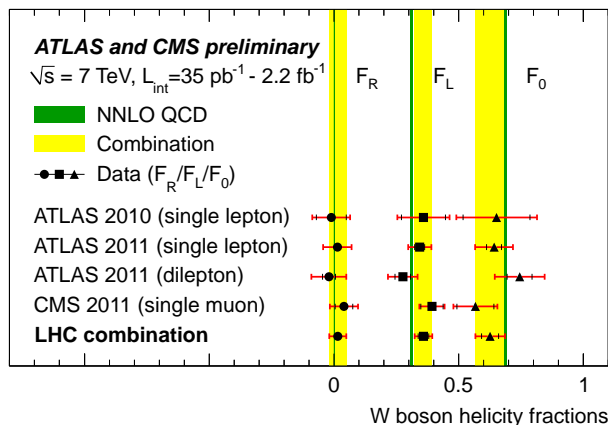


Figure 1.11: Latest results of W helicity fraction measurements at $\sqrt{s} = 7$ TeV [89–92].

quark and the W boson, this observable is predestined for probing anomalous couplings at the Wtb vertex [8, 85]. Figure 1.11 shows the latest results of W helicity fraction measurements at $\sqrt{s} = 7$ TeV [89–92]. The CMS collaboration recently published a W helicity measurement at $\sqrt{s} = 8$ TeV [98]. The ATLAS measurement of the W helicity fractions used for the combination presented in this thesis is described in Section 2.1.

1.5 t -channel single top quark production cross section

The t -channel single top quark production takes place via charged weak currents. It is the single top quark production process with the highest cross section of all single top quark productions for proton-proton collisions at $\sqrt{s} = 7$ TeV, see Section 1.2. This cross section is much higher than the s -channel single top quark production cross section due to the virtuality of the exchanged W boson. In the Standard Model, it is proportional to the square of the coupling at the Wtb vertex given by its CKM matrix element V_{tb} multiplied by the electroweak coupling constant. Therefore, a measurement of the t -channel single top quark production cross section (for simplicity also called “ t -channel cross section”) can be used to determine V_{tb} [7]. Two processes are contained within this channel: the $2 \rightarrow 2$ process (also called “five-flavour scheme”, see Figure 1.4 b)) and the $2 \rightarrow 3$ process (also called “four-flavour scheme”, see Figure 1.4 c)).

In the $2 \rightarrow 3$ process, a gluon splits into a bottom-antibottom quark pair. One of these two quarks interchanges a virtual W boson with the light quark also taking part in the collision. This results in the production of a light down-type quark, an antibottom quark

and a top quark or a light up-type quark, a bottom quark and an antitop quark [99].

The t -channel $2 \rightarrow 2$ single top production (see Figure 1.4 b)) is the process used for this combination. At leading order quantum chromodynamics, it takes place either if an up quark from one proton interacts with a bottom quark from the other proton to a top quark and a down quark or if a down quark interacts with an antibottom quark to an antitop quark and an up quark. In this process, the bottom quark is considered as a constituent of the proton. Therefore, the $2 \rightarrow 2$ process depends strongly on the parton distribution functions¹⁴ (PDFs) of the bottom quarks inside the colliding protons and can be used to constrain these bottom quark PDFs [7].

Since the up quark density inside the proton is approximately twice as high as the down quark density, the top quark production is about twice as high as the antitop quark production in the t -channel [7]. The cross section of this channel is sensitive to many new physics models such as extra heavy quarks, gauge bosons or scalar bosons [100]. Separate measurements of the top and antitop quark cross section in this channel can be used to test the up and down quark PDFs. Because of the exchange of a virtual W boson, it can also be used to investigate anomalous couplings at the Wtb vertex [85]. The results of the latest ATLAS measurements of the t -channel cross section are shown in Figure 1.3. The latest ATLAS measurement at $\sqrt{s} = 7$ TeV used for this combination is presented in Section 2.2.

1.6 The Large Hadron Collider and the ATLAS experiment

The *Large Hadron Collider* (LHC) at the European Organisation for Nuclear Research (CERN) located near Geneva, Switzerland is a superconducting accelerator and collider for proton-proton and lead-lead ion beams. Its main objectives are to probe the Standard Model at the TeV energy scale, to search for physics beyond the Standard Model and to find and measure the properties of the Higgs boson, which was finally observed in 2012 by the ATLAS and CMS collaborations [57, 58]. It is located in the former tunnel of the *Large Electron Positron Collider* (LEP) with a circumference of 26.7 km and lies roughly 100 m below the surface. The LHC hosts four main detectors: the two multi purpose, 4π detectors *A Toroidal LHC Apparatus* (ATLAS) and *Compact Muon Solenoid* (CMS), as well as *A Large Ion Collider Experiment* (ALICE), which is designed for the

¹⁴The parton distribution functions express the distribution of parton momenta within the proton [37].

1.6 The Large Hadron Collider and the ATLAS experiment

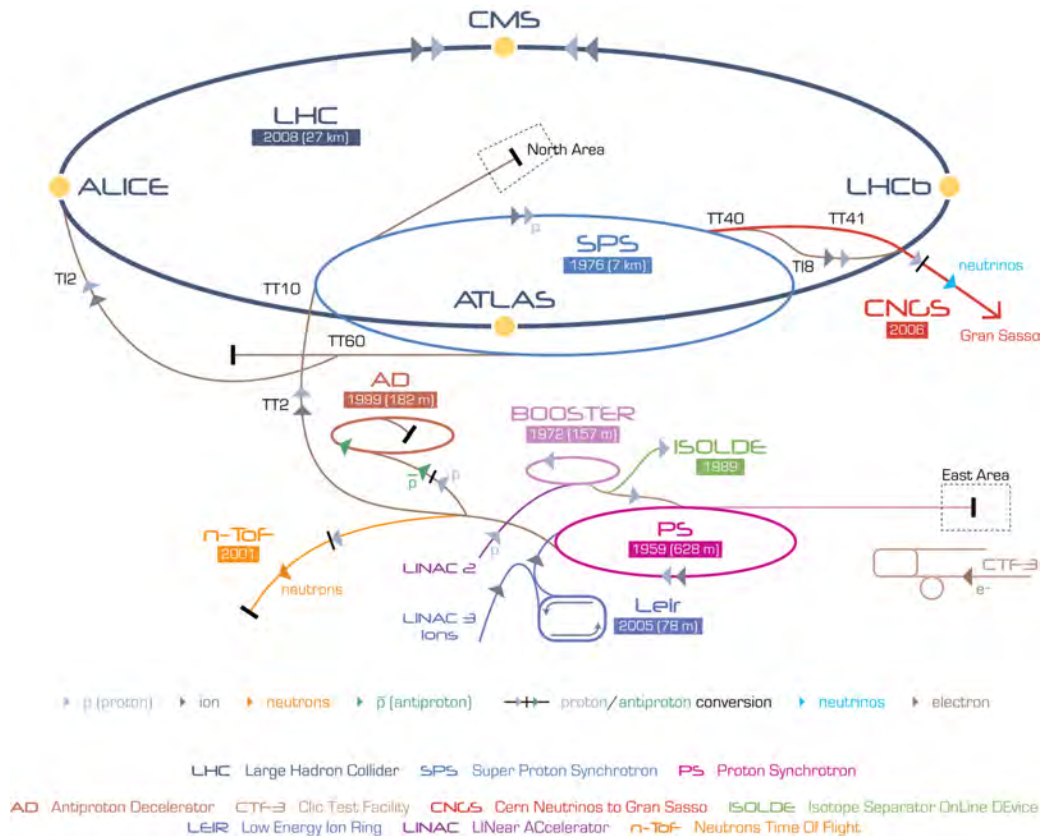


Figure 1.12: Schematic layout of the CERN accelerator complex including the circumference and the year of the first operation of each accelerator © CERN.

lead-lead collisions to study the quark-gluon-plasma and the *Large Hadron Collider beauty* experiment (LHCb) to study the decay of hadrons consisting of charm or bottom quarks. The centre-of-mass energy for proton-proton collisions was 7 TeV in the years 2010 to 2011 and 8 TeV in 2012. From 2013 to 2015, the LHC undergoes an upgrade with the aim to reach a centre-of-mass energy of 13 TeV in proton-proton collisions. It is planned to reach a centre-of-mass energy of 14 TeV later on in the second run. To accelerate the hadrons to the desired energies and luminosities, the CERN accelerator chain is used (see Figure 1.12). Protons are first accelerated in the LINAC 2, then in the Proton Synchrotron Booster, the Proton Synchrotron, the Super Proton Synchrotron and are finally injected into the LHC [101].

Compared to circular lepton accelerators of the same size and energy per beam, the energy loss due to synchrotron radiation of a proton accelerator (like the LHC) is much lower because the accelerated particles are heavier. This makes it possible for the LHC to reach for much higher centre-of-mass energies than a circular lepton collider of the same radius, making it an ideal machine to search for new physics at high energy scales. On the other hand, the energy of the colliding partons inside the protons circulating in the LHC

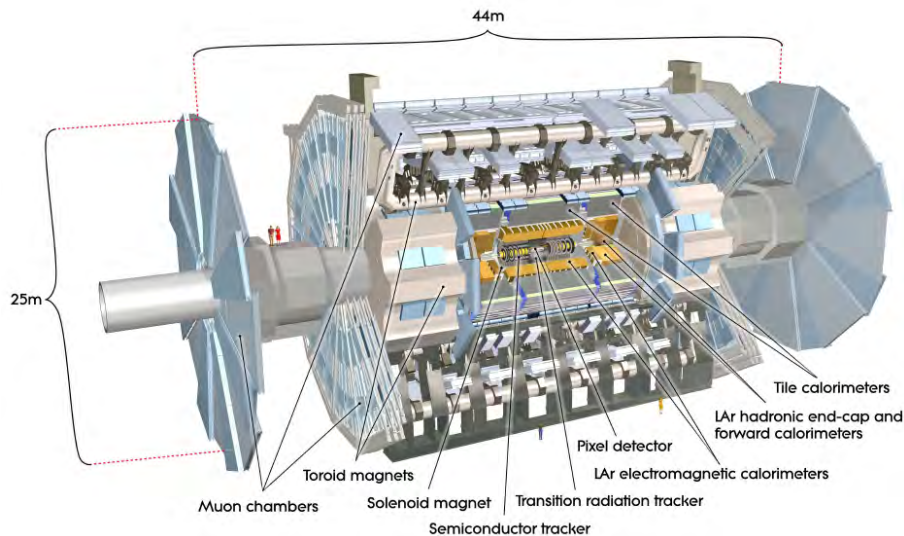


Figure 1.13: Cut-away view of the ATLAS detector [103].

is not exactly determined¹⁵, making it difficult to determine the energy at which observed particles are produced [102].

The ATLAS detector, see Figure 1.13, is a multipurpose detector for hadron collisions at the TeV scale, covering almost 4π of the solid angle around the interaction point. It is designed to deal with bunches containing up to 10^{11} protons colliding 40 million times per second at a centre-of-mass energy up to 14 TeV and with luminosities larger than $10^{34} \text{ cm}^{-2} \text{ s}^{-1}$ [102, 103]. Its main tasks are, like for CMS, to record events including heavy particles for top quark physics, Higgs physics and searches for physics beyond the Standard Model, but also for B -physics. The ATLAS detector consists of the following detector units (from the inside to the outside) [103]:

The *Inner Detector* (see Figure 1.14 left) consists of three subdetectors. The detector with the closest distance from the collision point is the *Pixel Detector*. It localises the decay vertices of hadrons and leptons which is important for example for b -tagging¹⁶. The next detectors are the *Semi-Conductor Tracker* (SCT) and then the *Transition Radiation Tracker* (TRT). Both are used to reconstruct the trajectories of charged particles passing the detector. The TRT is also used to distinguish charged leptons from hadrons via tran-

¹⁵They can be estimated from parton distribution functions.

¹⁶ b -tagging is the method of identifying a decay vertex as a decay vertex of a hadron containing a bottom quark (secondary vertex). Due to the small CKM matrix elements V_{ub} and V_{cb} , decays of such hadrons are suppressed, so the hadron containing the bottom quark has a longer lifetime than the particles immediately decaying at the interaction point (primary vertex). Secondary vertices that are well separated from the primary vertices are expected to contain a heavy flavour quark (charm or bottom). This is very important for detecting top quark decay because they include a W boson and a bottom quark at almost 100% of the time.

sition radiation. Together with the 2 Tesla solenoid magnet (see below) surrounding the Inner Detector, the momentum of charged particles can be determined by the curvature of their trajectories passing the Inner Detector.

The *calorimeter system* (see Figure 1.14 right) is used to determine the energy of particles, such as electrons, photons and hadrons, via the measurement of the energy deposition of electromagnetic and hadronic showers. The calorimeter system consists of two calorimeters (from the inside to the outside): first an *electromagnetic calorimeter* filled with liquid argon. The next calorimeter is the *hadronic calorimeter* consisting of liquid argon (hadronic endcap calorimeter and forward calorimeter) and scintillating tiles combined with steel absorbers (tile calorimeter).

The *muon system* (see Figure 1.15 left) identifies muons, which could pass the detector without depositing their energy in the calorimeter system¹⁷, using trigger chambers. It also measures their momentum by the curvature of the tracks inside the field of the toroid (see below) using high-precision tracking chambers. To provide nearly 4π detection capabilities, the muon detectors are arranged in three cylindrical layers around the beam axis (central muon system) and in planes perpendicular to the beam (transition and end-cap regions).

The *magnet system* (see Figure 1.15 right) is used to determine the momentum of charged particles via the curvature of their tracks. It consists of the already mentioned *solenoid*, providing the 2 Tesla axial magnetic field for the Inner Detector, and superconducting air-core *toroids*. The toroids consist of a barrel toroid producing a toroidal magnetic field of approximately 0.5 Tesla in the central muon system and end cap toroids producing toroidal magnetic fields of approximately 1 Tesla for the muon detectors in the end-cap regions.

¹⁷This is possible because, in the case of muons in the ATLAS detector, the cross section decreases with the increasing mass of the interacting particle and the muons have a long enough lifetime not to decay inside the detector.

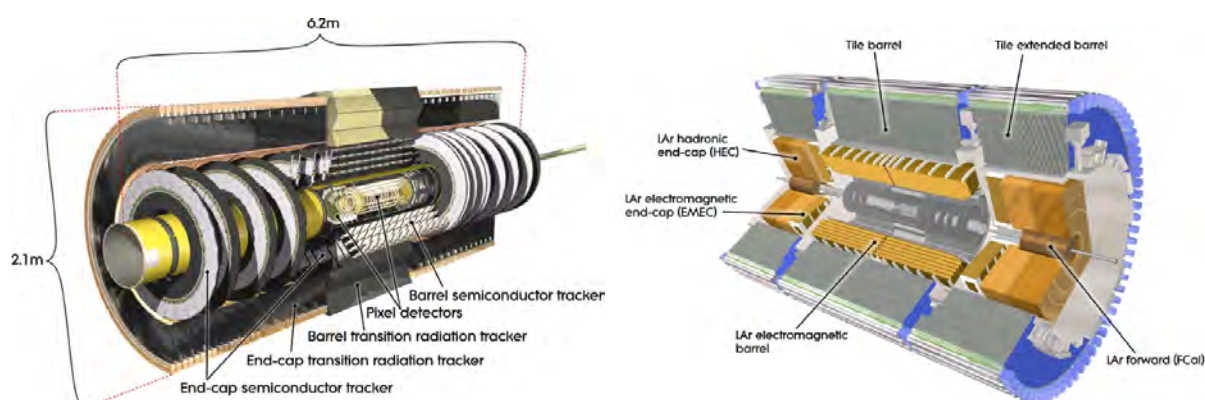


Figure 1.14: Left: Cut-away view of the ATLAS Inner Detector. Right: Cut-away view of the ATLAS calorimeter system [103].

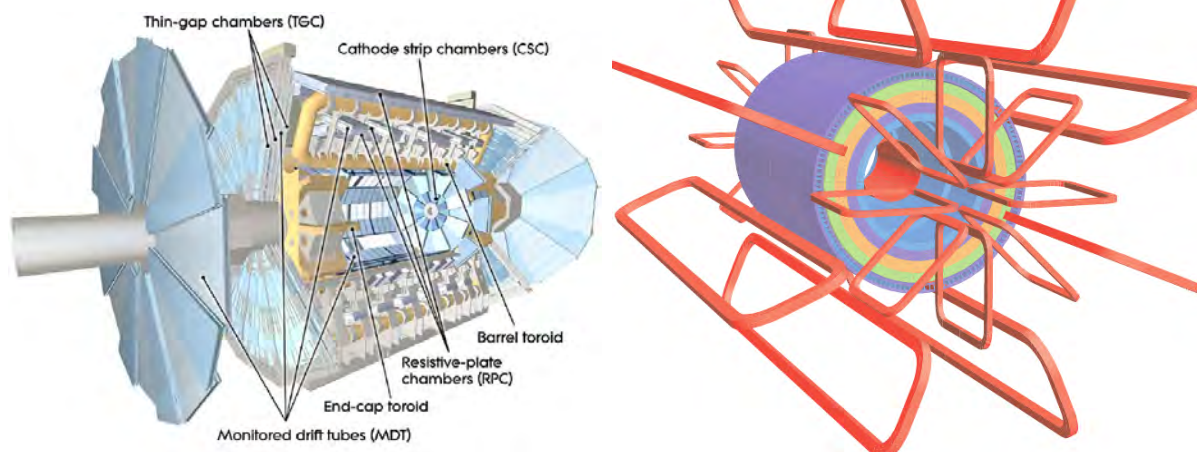


Figure 1.15: Left: Cut-away view of the ATLAS muon system. Right: ATLAS magnet system (displayed in red). The toroid system lies outside and the solenoid system lies inside the calorimeter system [103].

2 Current measurements

In this chapter, the top quark measurements used for the combination are presented. Both measurements use data from the ATLAS experiment, taken in the year 2011 at a centre-of-mass energy of 7 TeV with approximately the same integrated luminosity. While the measurement of the t -channel single top production cross section has recently been published [7], the measurement of the W helicity fractions is not yet published [6]. In addition, this chapter includes a description of how the systematic uncertainties are categorised for the combination presented in this thesis. This categorisation can deviate from the description within the references of these two measurements. Otherwise, it would not be possible to create proper correlation and covariance matrices for the combination.

2.1 W helicity fractions

The W boson helicity fractions and the corresponding uncertainties used in this combination are the results of an analysis presented in Reference [6]. This reference is a master's thesis and the results are not yet published neither on a preprint server, nor in a peer reviewed journal. Therefore, these values may differ from the values in the final publication. The results are

$$\begin{aligned} F_0 &= 0.634 \pm 0.031 \text{ (stat. } \oplus \text{ syst.)}, \\ F_L &= 0.337 \pm 0.022 \text{ (stat. } \oplus \text{ syst.)}, \\ F_R &= 0.030 \pm 0.024 \text{ (stat. } \oplus \text{ syst.)}. \end{aligned} \tag{2.1}$$

This analysis uses the full 2011 ATLAS data set corresponding to an integrated luminosity of 4.7 fb^{-1} taken at a centre-of-mass energy of 7 TeV from $t\bar{t}$ events in the lepton+jets (or “single-lepton”) channel. The event selection requires exactly one high energetic and isolated electron or muon, at least four high energetic jets with at least one identified as a b -jet and missing transverse momentum.

2 Current measurements

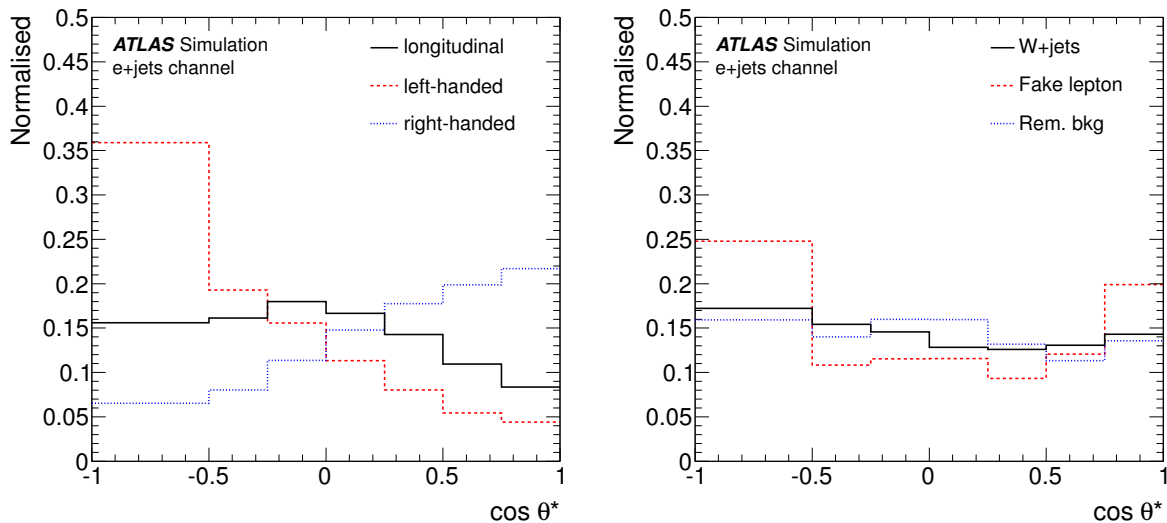


Figure 2.1: Templates of $\cos \theta^*$ distributions for the different helicity state signal processes from Reference [6]. Left: signal templates for the electron+jets channel. Right: background templates for the electron+jets channel. Similar templates also exist for the μ +jets channel

The W helicity fractions are determined using the template method¹. In this method, templates of the $\cos \theta^*$ distributions (see Figure 2.1; see also Section 1.4 for the definition of $\cos \theta^*$) for the left-handed, right-handed and longitudinally polarised W boson events as well as the background processes are fitted to the measured $\cos \theta^*$ distribution using a combined profile likelihood fit. The measured $\cos \theta^*$ distribution is reconstructed using a kinematic likelihood approach implemented in the *KL Fitter* package [104]. The background contributions are either determined by Monte Carlo simulations or data driven methods.

The fit is performed in four channels: both electron+jets and muon+jets channels are divided into a channel with exactly one b -tagged jet and a channel with at least two b -tagged jets. Three background templates are fitted: W +jets, multijet and “remaining background”². The W helicity fractions F_i ($i = 0, L, R$) are calculated via

$$F_i = \frac{\hat{N}_i}{\hat{N}_0 + \hat{N}_L + \hat{N}_R}, \quad (2.2)$$

where \hat{N}_i are the best model parameters of the total number of W bosons measured with a certain helicity, obtained by the profile likelihood fit.

The uncertainty from the profile likelihood fit is used as the total uncertainty of the mea-

¹Another common method for determining the W helicity fractions is the method using angular asymmetries, which is used in several other analyses such as [89]. It is described in Appendix A.2.

²“Remaining background” contains the background processes single top quark, diboson and Z +jets.

surement. Nevertheless, knowing the influence of each source of systematic uncertainty on the result is important in order to combine the two measurements taking into account correlations between the sources of systematic uncertainties. This information is not provided by the profile likelihood fit. However, the uncertainties obtained by ensemble tests, which are also conducted³ in Reference [6], are used to study the individual influence of each systematic source on F_0 , F_L and F_R . These uncertainties are larger than the ones quoted in (2.1), which are obtained from the profile likelihood fit.

In this ensemble test, pseudo data is obtained from Monte Carlo simulations by separately varying the sources of systematic uncertainties up and down within one standard deviation (1σ) of their uncertainties. From this data, ensembles are created by fluctuating each bin of the pseudo data distribution according to Poissonian statistics. For each ensemble, a template fit is performed to determine the total number of W bosons measured with a certain helicity N_i [105]. This is also called a “pseudo measurement”. The fitted parameters of N_i are written into histograms. From this template fit, the W helicity fractions F_i ($i = 0, L, R$) are calculated by

$$F_i = \frac{\langle N_i \rangle}{\langle N_0 \rangle + \langle N_L \rangle + \langle N_R \rangle}, \quad (2.3)$$

where $\langle N_i \rangle$ is the mean value of the N_i -distribution from the ensembles. The difference between the F_i with the value of a systematic source varied by $\pm 1\sigma$ of its uncertainty and the nominal sample is taken to be the corresponding systematic uncertainty. Figure 2.2 illustrates this procedure for the jet energy scale.

³In this reference, this was a test of the improvement of the profile likelihood fit towards the rather classical analysis using ensemble tests.

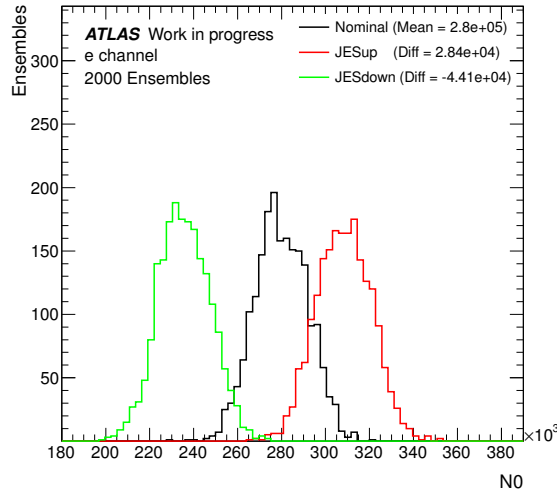


Figure 2.2: Example for the evaluation of systematic uncertainties for the W helicity measurement, taken from Reference [6]. It shows the distributions of the number of counted W bosons with a longitudinal polarisation from nominal pseudo data and pseudo data for the jet energy scale varied by $\pm 1\sigma$ (“JESup”/“JESdown”).

2.2 t -channel single top quark production cross section

The latest ATLAS measurement of the t -channel cross section at $\sqrt{s} = 7$ TeV uses a dataset corresponding to an integrated luminosity of 4.59 fb^{-1} , collected in 2011 [7]. Considering only the $2 \rightarrow 2$ process to contribute, the results are

$$\begin{aligned}
 \sigma_t &= 46 \pm 6 \text{ pb (stat. } \oplus \text{ syst.)}, \\
 \sigma_{\bar{t}} &= 23 \pm 4 \text{ pb (stat. } \oplus \text{ syst.)}, \\
 \sigma_t/\sigma_{\bar{t}} &= 2.04 \pm 0.18 \text{ pb (stat. } \oplus \text{ syst.)}, \\
 \sigma_{t+\bar{t}} &= 68 \pm 8 \text{ pb (stat. } \oplus \text{ syst.)},
 \end{aligned}
 \tag{2.4}$$

where σ_t and $\sigma_{\bar{t}}$ are the total top and antitop quark production cross sections and $\sigma_{t+\bar{t}}$ is the inclusive production cross section. The preselection includes events with one charged lepton (electron or muon), large missing transverse momentum and two or three jets with high transverse momentum. The cross sections are obtained using a binned maximum-likelihood fit to the output distributions of neural networks. The main background processes are W +jets production and top quark pair production. This measurement also provides differential t -channel cross sections for the top and antitop quark as a function of

2.2 t -channel single top quark production cross section

the transverse momentum and the absolute value of the rapidity of the (anti)top quark, as well as a determination of the CKM matrix element of the Wtb vertex to $|V_{tb}| = 1.02 \pm 0.07$. Cross section measurements are basically counting experiments. The neural network trained with simulated events, discriminates between signal and background events. The number of signal events is determined by fitting the output distributions for signal and background from the neural network to the selected data set. Dividing this total number of signal events N by the integrated luminosity of the dataset $\int \mathcal{L}$, the branching fraction of the observed decay channel $BR(t \rightarrow \dots)$, as well as by the efficiency and acceptance⁴, the cross section σ can be calculated by the formula (e.g. [97])

$$\sigma = \frac{N}{\epsilon \cdot BR(t \rightarrow \dots) \cdot \int \mathcal{L}} . \quad (2.5)$$

To determine the systematic uncertainties for each source of systematic uncertainty i , a distribution δ_i of a certain number of values is generated according to a standard normal distribution. Each value of δ_i specifies the strength (and sign) of a systematic deviation. The systematic deviation for each process⁵ j arises from the scaling with the corresponding acceptance uncertainties ϵ_{ij+} (and ϵ_{ij-}). These are the relative differences in the acceptance between the nominal samples and the samples in which the source of systematic uncertainty is shifted up (and down), normally by one standard deviation of its uncertainty. The distributions ν_{ij} of the number of events of the process j depending on the source of systematic uncertainty i is

$$\nu_{ij} = \tilde{\nu}_j \cdot [1 + |\delta_i| \cdot (H(\delta_i)\epsilon_{ij+} + H(-\delta_i)\epsilon_{ij-})] , \quad (2.6)$$

where $\tilde{\nu}_j$ is the predicted number of events for the process j . The function $H(\delta_i)$ is the Heaviside function. If one value of ν_{ij} turns out to be negative, δ_i is calculated again. For the source of systematic uncertainty i , the maximum-likelihood fit is performed for all values of the distribution of ν_{ij} for each process j . This fit yields a scale factor

$$\beta_i = \frac{\sigma_i}{\tilde{\sigma}} , \quad (2.7)$$

where σ_i is the distribution of the cross section depending on the source of systematic uncertainty i and $\tilde{\sigma}$ is the predicted value of the cross section. The corresponding systematic uncertainty $(\Delta\sigma/\sigma)_i$ is the standard deviation⁶ of the distribution of β_i [106].

⁴The latter two are merged here into the coefficient ϵ for simplicity

⁵These are the signal and background processes contributing to the determination of the cross section.

⁶In the data used here, the statistical uncertainty is included in each of these distributions, so it has to be subtracted quadratically from the standard deviation.

2.3 Categorisation of the uncertainties

For both of the measurements described above, different conventions for describing the systematic uncertainties were chosen by the authors. To be able to compare these measurements in terms of the uncertainties, it is necessary to order the sources of systematic uncertainties in a reasonable way. 19 categories for the systematic uncertainties are created, containing several sources of systematic uncertainties each. These categories are listed in Table 2.1. Appendix A.1 contains lists of which source of systematic uncertainty belongs to which of these 19 categories. To obtain the size of the uncertainty of each category, the uncertainties of all systematic sources within the category are added quadratically. In addition, one category for the statistical uncertainties and one category for the uncertainties of the predicted Standard Model values are included in the total uncertainty of each observable.

The total systematic uncertainties are taken from the references of the two measurements [6, 7]. For the t -channel cross section, the total systematic and statistical uncertainties are given separately⁷. For the W helicity fraction measurement, the total uncertainty is taken from the profile likelihood fit, while the correlations of the systematic uncertainties can only be determined using data from the ensemble test, see Section 2.1. The uncertainties from the profile likelihood fit are much smaller than the ones from the ensemble test and do not provide any information about the individual uncertainties of the categories. To determine the “total systematic uncertainties” of the W helicity fraction measurement, the statistical uncertainties from the ensemble tests are subtracted quadratically from the uncertainties from the profile likelihood fit. This was done to treat the correlations of the statistical uncertainties properly. Note that these “total systematic uncertainties” are not actually the total systematic uncertainties from the profile likelihood fit but adding the statistical uncertainties quadratically yields the total uncertainties of the observables using profiling.

The biggest systematic uncertainties stem from the jet energy scale, the jet energy resolution, lepton uncertainties (only cross section, “other lepton uncertainties”), jet reconstruction uncertainties, missing transverse energy, PDF uncertainties (only cross section) and Monte Carlo uncertainties (only cross section).

⁷See Table III in Reference [7].

2.3 Categorisation of the uncertainties

#		ΔF_0	ΔF_L	$\Delta\sigma_t/\sigma_t$	$\Delta\sigma_{\bar{t}}/\sigma_{\bar{t}}$
1)	JES	0.0352	0.0158	0.073	0.087
2)	BJES	0.0030	0.0051	0.008	0.008
3)	JER	0.0351	0.0234	0.021	0.013
4)	lepton identification	0.0039	0.0023	0.004	0.003
5)	other lepton uncertainties	0.0088	0.0017	0.028	0.030
6)	jet reco uncertainties	0.0190	0.0080	0.020	0.025
7)	missing E_T	0.0157	0.0062	0.021	0.034
8)	W +jets heavy flav. comp.	0.0066	0.0025	-	-
9)	W +jets shape variation	-	-	0.003	0.005
10)	JVF scale factor	0.0002	0.0002	0.006	0.003
11)	ISR/FSR Whel	0.0072	0.0024	-	-
	ISR/FSR Xsec	-	-	0.002	0.004
12)	template statistics	0.0106	0.0064	-	-
13)	top quark mass	0.0020	0.0130	0.010	0.013
14)	background normalisation	-	-	0.011	0.026
15)	multijet bkg. Whel	0.0100	0.0062	-	-
	multijet bkg. Xsec	-	-	0.011	0.017
16)	PDF	0.0020	0.0010	0.033	0.057
17)	Monte Carlo Whel	0.0075	0.0022	-	-
	Monte Carlo Xsec	-	-	0.031	0.039
18)	luminosity	-	-	0.015	0.012
19)	underlying event	0.0053	0.0038	-	-
	total systematic unc.	0.0218	0.0170	0.120	0.149
	statistical unc.	0.0220	0.0140	0.031	0.054
	unc. of SM prediction	0.0050	0.0050	0.039	0.043
	TOTAL unc.	0.0314	0.0226	0.130	0.164

Table 2.1: The 19 different categories for the systematic uncertainties plus the total systematic uncertainties taken from the References [6] and [7], the statistical uncertainties and the uncertainty of the predicted Standard Model (SM) value for each observable. This table also includes the total uncertainty for each observable.

2 Current measurements

It has to be mentioned that some categories have the same or similar names as in the references of the two measurement but yield different values for the uncertainties. This has several reasons:

- The sources of systematic uncertainties are sometimes categorised differently from the categorisations in the two references. Often, categories from the references are separated into two or merged into one category.
- Sometimes the data for the uncertainties provided by the authors is handled differently in the corresponding measurements than it is done in this combination.

Some categories of the two measurements are not correlated and some are also composed of slightly different systematics. These categories are listed separately in Table 2.1 for each measurement. Some categories only exist for one measurement. The reason is that some systematic uncertainties only play a role for one measurement (template statistics), are included in another category for one measurement (background normalization and luminosity) or are neglected in the analysis (underlying event). The categories “ W +jets heavy flavour composition” and “ W +jets shape variation” are treated as one category without correlation (see below). The categories for the sources of systematic uncertainties are:

1) Jet energy scale Collimated sprays of energetic hadrons, called jets, are produced by fragmentation of quarks and gluons and play an important role in high energy proton-proton collisions at the LHC. It is necessary to calibrate the jet energy corresponding to the stable particles in the ATLAS detector. It needs to be consistent in all regions of the detector and independent of additional events produced at high energy and high luminosity. The jet energy scale (JES) is the systematic uncertainty of the energy measurement of the jets in the calorimeter. It is dependent on the transverse momentum p_T and the pseudorapidity⁸ η of the jet. For the 4.6 fb^{-1} of data taken in 2011 with the ATLAS detector at a centre-of-mass energy of $\sqrt{s} = 7 \text{ TeV}$, the calibration is conducted using photons and Z bosons as reference objects. The smallest JES uncertainty is less than 1% for jets with $|\eta| < 1.2$ and $55 \leq p_T \leq 500 \text{ GeV}$. The resulting uncertainty is the largest for low- p_T jets at $|\eta| = 4.5$ and amounts to 6% [107, 108].

For the W helicity measurement, the uncertainty stemming from the JES uncertainty is evaluated by conducting ensemble tests, varying the JES within its uncertainties [6]. The

⁸The pseudorapidity $\eta = -\ln[\tan(\theta/2)]$ is a coordinate describing the position inside the detector, where θ is the angle between the beam axis and the line between the position in the detector and the collision point. In the highly relativistic limit, the difference in pseudorapidity of two particles is Lorentz invariant for boosts along the beam axis.

influence on the t -channel cross sections is evaluated by scaling the energy of each jet up and down by 1σ , propagating this change to the missing transverse energy and conducting the measurement with these varied values [106].

2) b -jet energy scale The b -jet energy scale (bJES) is similar to the JES, but for jets induced by bottom (b) quarks. The bJES does not only influence energy measurements, it also influences the b -tagging calibration. The knowledge of the properties of the b -jets emerging from the top quark decay is necessary for conducting precise top quark measurements. The bJES is determined using Monte Carlo simulations and tracks associated to b -tagged jets in the data set used for calibration [107–109]. The influence of its uncertainty on the observables, which is evaluated in the same way as for the JES, is about one order of magnitude smaller than of the other JES uncertainties together [6, 106].

3) Jet energy resolution The jet energy resolution (JER) is determined using in situ methods [110]. For the W helicity measurement, this uncertainty was obtained by smearing the jet momenta in Monte Carlo with a Gaussian function, according to a 10% uncertainty⁹. It is a one-sided uncertainty because the resolution cannot be improved after simulation. For better handling of the data, the uncertainty is symmetrised [6, 110]. For the cross section measurement, a similar method is used [106].

Lepton uncertainties: “4) lepton identification” and “5) other lepton uncertainties” These are the uncertainties due to the lepton scale factors, which scale the Monte Carlo description to match the lepton trigger/ID efficiencies in data. Their uncertainties only affect measurements using leptonic decay channels including electrons and/or muons. Some of them are applied especially for one of these two leptons [6]. The lepton scale factors are split into “lepton identification” and “other lepton uncertainties”. “Lepton identification” includes the uncertainties related to the lepton identification efficiencies. “Other lepton uncertainties” includes uncertainties of the lepton reconstruction and trigger efficiencies, as well as electron energy scales and resolutions, the muon energy resolution systematic smearing in the Inner Detector and muon spectrometer, the uncertainty of the charge measurement of electrons and other systematic uncertainties [6, 106]. In the W helicity measurement, the lepton energy scales are determined by the comparison with the corrections from $Z \rightarrow e^+e^-$ and $Z \rightarrow \mu^+\mu^-$ events [111, 112]. These events are also used to determine the lepton scale factors. The lepton energy resolution is obtained

⁹This is the relative difference of the JER in real data and Monte Carlo data.

2 Current measurements

by smearing Monte Carlo data to match the resolution in data [6]. In the cross section measurement, the lepton energy scales are determined by scaling the transverse momenta of the leptons by $\pm 1\sigma$ and re-applying the event selection. The uncertainties of the scale factors applied to the lepton trigger and ID efficiencies are evaluated by re-computing the predicted Monte Carlo event yields and acceptances using shifted scale factors [106].

6) Jet reconstruction (reco) uncertainties Usually, the jet reconstruction uncertainty includes the jet energy resolution, the jet reconstruction efficiency (JEFF) and the jet vertex fraction (JVF) scale factors [6]. However, for the combination presented in this thesis, the category “jet reconstruction uncertainties” contains the JEFF and the b -tagging scale factor uncertainties for the W helicity measurement, as well as the scale factors for light-, charm- and b -tagging (flavour tagging scale factors) for the cross section measurement. The uncertainties on the JVF scale factors are not included in this uncertainty. The flavour tagging scale factors are corrected by the tagging and mistagging efficiencies of the different quark flavours [106]. In the W helicity measurement, the b -tagging scale factor uncertainties are evaluated by investigating the influence of the eigenvectors of the uncertainty matrix on the $\cos\theta^*$ -distribution. The cross section measurement uses a profile likelihood fit to determine the uncertainty from the b -tagging scale factors. The cross section measurement also includes the uncertainty due to different acceptances between b -jets and anti- b -jets. The JEFF takes into account that the jet reconstruction of the detector is not perfectly modelled. It is determined by randomly dropping reconstructed jets from the events before the event selection is performed. This uncertainty is also one-sided and is symmetrised for better handling of the data [6, 106].

7) Missing transverse momentum The total momentum of the collision products of elementary particles colliding head-on with the same energy each would be zero. Because protons are not elementary particles, the energy and momentum of two colliding partons within the colliding protons at the LHC is unknown. Therefore, even though both colliding protons at the LHC have the same energy, the total momentum of the collision products is typically different from zero. Another criterion is the momentum transverse to the beam axis, called transverse momentum (\vec{p}_T). Assuming the colliding partons to have approximately no momentum transverse to the beam axis, the total transverse momentum of the collision products should be zero. In the highly relativistic limit the *transverse energy* is $E_T = |\vec{p}_T|$. Therefore, E_T is often referred to as the “magnitude of the transverse momentum” or simply as the “transverse momentum” in high energy physics.

Some particles cannot be detected by the ATLAS detector systems. The only Standard Model particles that behave like this are neutrinos. Other examples could be the electrically neutral lightest supersymmetric particle (LISP) from supersymmetric extensions of the Standard Model or dark matter particles in general. If some of these particles are produced, the reconstructed total transverse momentum is different from zero. The deviation from zero is called missing transverse momentum (\cancel{E}_T). It cannot only be caused by non-interacting particles, but also by dead material or gaps in the detector and by very forward particles escaping the detector under very high rapidities or even escaping into the beam pipe.

For both measurements, the uncertainty for the missing transverse momentum is determined from the cell-out term variations¹⁰, assuming them to be fully correlated with the soft-jet uncertainties¹¹. Additionally for the W helicity measurement, they contain pile-up variations¹² [6, 106].

W +jets uncertainties The W +jets process is one of the main backgrounds for both of the combined measurements. Estimating the contribution of this process incorrectly can have a huge influence on the results. The W helicity measurement and the t -channel cross section measurement treat the sources of systematic uncertainties from the W +jets estimation in different ways. Therefore, this category does not have a correlation between both measurements. The categories for the two measurements are:

8) W +jets heavy flavour composition: The uncertainty for the W helicity measurement includes six components modifying the shape of the W +jets background templates. They stem from the uncertainty on the W +jets heavy flavour scale factors. These scale factors are used to determine the heavy flavour composition of the associates jets. Especially the fractions of the processes $Wb\bar{b}$ +jets, $Wc\bar{c}$ +jets, Wc +jets and W +light jets have high uncertainties [6].

9) W +jets shape variation: This uncertainty for the t -channel cross section measurement is determined by varying several parameters in the generation of the W +jets background samples, reweighting them according to these parameters and taking the largest variation as systematic uncertainty [106].

¹⁰Uncertainty stemming from the global calibration scheme used for deposited energy in the calorimeter which cannot be associated with physics objects.

¹¹Calorimeter calibration uncertainty for jets with low p_T .

¹²Uncertainty stemming from the multiple interaction per bunch crossing.

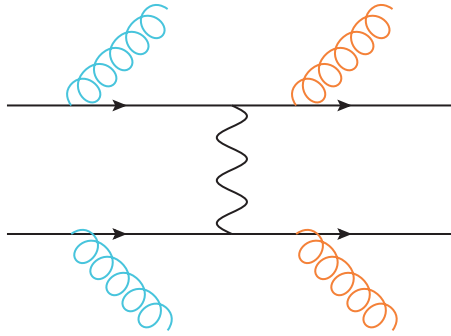


Figure 2.3: Illustration of ISR/FSR shown for an arbitrary process. The blue curled lines (left) show possible gluons emerging from initial state radiation. The red curled lines (right) show possible gluons emerging from final state radiation.

10) Jet vertex fraction (JVF) scale factor The jet vertex fraction (JVF) is the summed transverse momentum of all tracks matched to a certain vertex divided by the total transverse momentum of the tracks matched to a certain jet in the calorimeter. It measures the probability that a jet originates from a particular vertex [113, 114]. For 2011 data, as it is used for both measurements, $|JVF| > 0.75$ is required to reject jets from pileup. The JVF scale factors are corrections for the efficiency and miss-tag efficiencies of the JVF cut [6].

11) Initial and final state radiation (ISR/FSR) This systematic uncertainty describes the influence of additional jets from initial and final state radiation on the background processes. Initial/final state radiation is the radiation of gluons in the initial/final state resulting in additional jets in the event, see Figure 2.3. The amount of these additional jets is dependent on the strong coupling α_s . In the W helicity measurement and the t -channel cross section measurement, there are two different categories for the ISR/FSR, because the expected background processes and their generators differ from each other. For the W helicity measurement, the QCD cut-off parameter Λ_{QCD} , which is directly related to α_s , is varied between $0.5 \cdot \Lambda_{\text{QCD}}$ and $2 \cdot \Lambda_{\text{QCD}}$ for the Monte Carlo event generation. The systematic uncertainties are the resulting differences divided by two for each helicity fraction [6]. For the t -channel cross section measurement, a similar approach is used [106].

12) Template statistics These are the uncertainties of the templates used for the fit to the measured $\cos \theta^*$ distribution of the W helicity measurement. Therefore, this category does not exist for the t -channel cross section measurement. The uncertainties stem from the limited statistics of the Monte Carlo samples and the binning of the $\cos \theta^*$ distribution.

To evaluate this uncertainty, the templates are normalised to the Monte Carlo luminosity and the individual bin contents are fluctuated within Poissonian probability. Ensemble tests with simultaneously fluctuating templates and fixed pseudo data are performed. The widths of the parameter distributions from the resulting fit are taken as the uncertainties. The templates of F_0 and W +jets cause the largest uncertainties [6].

13) Top quark mass The uncertainties on the W helicity fractions, caused by the choice of the top quark mass in the analysis, are obtained by ensemble tests at different top quark masses¹³ and a linear fit on the resulting helicity fractions. The result is the slope multiplied by¹⁴ 1.4 GeV [6]. For the t -channel cross section measurement, the dependence of the observables on the top quark mass is described by the function

$$\sigma_{t/\bar{t}}(172.5 \text{ GeV} + \Delta m_t) = \sigma_{t/\bar{t}}(172.5 \text{ GeV}) + p_1 \cdot \Delta m_t + p_2 \cdot \Delta m_t^2, \quad (2.8)$$

where $\sigma_{t/\bar{t}}(m_t)$ is the measured top or antitop cross section in dependence on the top quark mass used for the analysis. For the top quark cross section, the coefficients are $p_1 = -0.27$ [pb/GeV] and $p_2 = -0.04$ [pb/GeV²], and for the antitop cross section, the coefficients are $p_1 = -0.19$ [pb/GeV] and $p_2 = -0.02$ [pb/GeV²] [7]. For an easy comparison with the W helicity measurement, the uncertainty due to the choice of the top quark mass for the t -channel cross section measurement is chosen to be

$$\left(\frac{\Delta \sigma_{t/\bar{t}}}{\sigma_{t/\bar{t}}} \right)_{m_t} = \frac{\sigma_{t/\bar{t}}(172.5 \text{ GeV} + 1.4 \text{ GeV}) - \sigma_{t/\bar{t}}(172.5 \text{ GeV})}{\sigma_{t/\bar{t}}(172.5 \text{ GeV})}. \quad (2.9)$$

14) Background normalisation This is an uncertainty for the t -channel cross section measurement due to the normalisation of the different background processes. The uncertainties of the event yields of the processes $Wb\bar{b}$, $Wc\bar{c}$, W +light jets, Wc +jets, $t\bar{t}$, Z +jets, diboson, as well as for the W -associated production and s -channel single top production are included in this uncertainty, as well as the uncertainties of the ratio W +2 jets/ W +3 jets for the different flavours [106]. For the W helicity measurement, this uncertainty is included in the statistical uncertainty [6].

¹³The different top quark masses used are 167.5 GeV, 170 GeV, 172.5 GeV, 175 GeV and 177.5 GeV.

¹⁴This is the uncertainty of the LHC top mass combination at the time this W helicity analysis was conducted [115].

15) Multijet background This category describes the uncertainties stemming from the multijet background, often also referred to as the “QCD background”. Both measurements are not correlated with respect to this uncertainty, because it is treated separately for the W helicity measurement and for the t channel cross section measurement. For the W helicity measurement, the uncertainties are studied separately for the electron+jets and the muon+jets channel using ensemble tests. For the muon+jets channel, two different methods are compared, which differ in the estimation of the real efficiencies and the fake efficiencies. For the electron+jets channel, the variations of the real efficiencies and fake efficiencies are determined separately and added up quadratically [6]. For the t -channel cross section measurement, systematic uncertainties stemming from the choice of multijet background estimates, the different treatment of forward and central electrons and the different charge estimations in the multijet background are taken into account [106].

16) Parton distribution functions (PDFs) This category describes the uncertainties stemming from the parton distribution functions. For the t -channel cross section measurement, simulated events are reweighed according to the PDF uncertainty eigenvectors and the uncertainties are calculated according to Equation 43 in Reference [116]. Then, the envelope is calculated as the final PDF uncertainty [106]. For the W helicity measurement, a similar approach is used [6].

17) Monte Carlo This category describes the systematic uncertainties caused by the Monte Carlo generators and parton shower algorithms, as well as by the different renormalisation and factorisation scales of the different Monte Carlo generators. It is treated in two different categories for the W helicity measurement and the t -channel cross section measurement, because the single top and $t\bar{t}$ Monte Carlo samples are not correlated. For the t -channel cross section measurement, this category also includes the uncertainty due to the limited size of the Monte Carlo samples of the t -channel cross section measurement¹⁵. For the W helicity measurement, the uncertainties are determined by creating ensembles from different generators to compare the uncertainties due to the Monte Carlo generator and the showering algorithm. The uncertainties due to the choice of $t\bar{t}$ generators are obtained by taking the difference of F_i ($i = 0, L, R$) between MC@NLO and ALPGEN + HERWIG (both full detector simulation) for each helicity fraction. The uncertainties from the choice of the showering algorithms are determined in the same way by taking the difference of the ensemble test results from POWHEG + PYTHIA and POWHEG + HERWIG

¹⁵For the measurement of the W helicity fractions, the Monte Carlo statistics are included in the template statistics.

(both fast detector simulation) [6]. For the t -channel cross section measurement, these uncertainties are determined in a similar way. The uncertainties for the generator choice and the showering are determined by comparing POWHEG-Box interfaced to PYTHIA with aMC@NLO + HERWIG, showered with HERWIG and JIMMY.

The renormalisation scale is a momentum scale μ_R chosen to avoid singularities during renormalisation [93]. The factorisation scale μ_F corresponds to the resolution with which the hadron is being probed: each parton carries a fraction x of the momentum of the hadron, with a number density $f(x, \mu_F)$ [117]. For the W helicity fractions, the corresponding uncertainties are determined by varying the renormalisation and factorisation scales within MC@NLO up and down. Ensemble tests according to Section 2.1 are then conducted to determine the uncertainties [6]. For the t -channel cross section measurement, the uncertainties of the renormalisation and factorisation scales¹⁶ μ_R and μ_F are calculated by varying both independently by factors of 0.5 and 2.0 for POWHEG-Box interfaced with PYTHIA. The scale of the parton shower is varied according to the renormalisation scale as well. The resulting uncertainty is the envelope of all variations. The Monte Carlo uncertainty of the $t\bar{t}$ background is determined by comparing POWHEG-Box interfaced to PYTHIA with ALPGEN interfaced to HERWIG [7].

18) Luminosity This is a source of systematic uncertainty for the t -channel cross section measurement. It is determined by van der Meer scans using calorimeter-based techniques conducted in References [118] and [119]. The uncertainty of the luminosity for the data from 2011 is 1.8%. The values shown in Table 2.1 (1.5% for the top quark cross section and 1.2% for the antitop quark cross section), stemming from the data provided from the authors of Reference [7], deviate from these values, although a value of 1.8% is also quoted in Reference [7]. Nevertheless, the values shown in Table 2.1 are also the ones used for the analysis from Reference [7], assuming the deviations to cancel together with other effects [106]. For the W helicity measurement, the luminosity uncertainty is included in the treatment of the statistical uncertainty and therefore not listed here [6, 120].

¹⁶For the determination of these uncertainties on the cross section measurement, the renormalisation and factorisation scales μ_R and μ_F are set to $\mu_R = \mu_F = 4 \cdot \sqrt{m_b^2 + p_{T,b}^2}$, where m_b is the bottom quark mass and $p_{T,b}$ is the transverse momentum of the bottom quark.

19) Underlying event Multiple parton interactions cause soft-scale events, called underlying events (UE). For the W helicity measurement¹⁷, pseudo data with different tunes for UE is generated using POWHEG + PYTHIA. The uncertainty for the underlying events is determined by conducting ensemble tests as described in Section 2.1 [6]. For the t -channel cross section measurement, the influence of this source of systematic uncertainty is too small to be mentioned [106].

Statistical uncertainties The statistical uncertainties have a big influence on the total uncertainties of both measurements. For the W helicity measurement, the influence of the binning of the $\cos\theta^*$ distribution¹⁸ and the estimators of the likelihood fit are main sources of statistical uncertainties. The statistical uncertainties are determined for this measurement by conducting the template fit without nuisance parameters [6]. For the t -channel cross section measurement, pseudo measurements with a different amount of entries are generated. With these pseudo measurements, a distribution β_i according to Equation (2.7) is calculated. The RMS of the β_i -distribution is the statistical uncertainty [106].

Uncertainties of the Standard Model prediction This category includes the uncertainties of the Standard Model predictions from References [96] and [74]. It is not included in the evaluations of the original measurements but is added for this combination to take into account the uncertainties of the actual Standard Model values in the model of the observables in dependence on anomalous couplings, see Section 3.2. It describes how the results can vary if the reference value of the Standard Model, which causes $(V_L, V_R, g_L, g_R) = (1, 0, 0, 0)$, varies. The uncertainties are symmetrized by taking the largest absolute value of the upper- and lower limits of each uncertainty. For the t -channel cross section measurement, the Standard Model uncertainties are divided by the measured cross sections to be consistent with the convention in Table 2.1.

¹⁷The values of the uncertainties are twice as big as quoted in the reference [6]. This deviation occurs because the results of the ensemble tests are divided by two in the reference. Nevertheless, the author recommended not to do this and to simply take the ensemble test results as they are [120].

¹⁸The binning of the $\cos\theta^*$ distribution is a source of statistical uncertainty because less bins lead to less shape sensitivity, causing a higher statistical uncertainty [6].

3 Combination and fitting framework

This chapter describes the framework used in this analysis to obtain bounds on anomalous Wtb couplings from the combination of the two top quark measurements presented in Chapter 2. Section 3.1 describes the method to combine both measurements. Section 3.2 presents the models describing the W helicity fractions and the t -channel cross section in terms of the anomalous couplings. Section 3.3 explains the method used to obtain the correlations between both measurements in terms of their sources of uncertainties.

3.1 The Bayesian method for the combination of measurements

For the combination of the two measurements, setting bounds on anomalous Wtb couplings, a method based on a Bayesian interpretation similar to the *best linear unbiased estimate* (BLUE) method [121] is used¹. This method is implemented using the C++ software package *Bayesian Analysis Toolkit* (BAT) [5]. The method is described in this section.

Assume N free predictions of observables²

$$\vec{y}(V_L, V_R, g_L, g_R) = (y_1(V_L, V_R, g_L, g_R), \dots, y_N(V_L, V_R, g_L, g_R)) \ , \quad (3.1)$$

depending on the model parameters, which are in this case the anomalous couplings. The corresponding posterior probability in dependence on the n measurements from the data

¹Nevertheless, the BLUE method is based on a frequentist interpretation and therefore, it is difficult to include prior information in this method.

²These are in this case the W helicity fractions and the single top t -channel production cross section as described in Section 3.2. In additional studies, the branching ratio of the process $\bar{B} \rightarrow X_s \gamma$ will be combined with the two top quark measurements in this way, see Sections 5.6 and 6.1.2 .

3 Combination and fitting framework

set $\vec{x} = (x_1, \dots, x_n)$ is determined via the equation of Bayes and Laplace [122]

$$p(\vec{y}(V_L, V_R, g_L, g_R)|\vec{x}) = \frac{p(\vec{x}|\vec{y}(V_L, V_R, g_L, g_R)) \cdot p(\vec{y}(V_L, V_R, g_L, g_R))}{p(\vec{x})}. \quad (3.2)$$

The term $p(\vec{x})$ is a normalisation constant referred to as the evidence. $p(\vec{y}(V_L, V_R, g_L, g_R))$ is the prior probability of the predictions $\vec{y}(V_L, V_R, g_L, g_R)$. It can contain constraints from previous analyses³. If the prior is set to unity, the global mode of the posterior corresponds to the BLUE solution. The Likelihood is constructed as

$$p(\vec{x}|\vec{y}(V_L, V_R, g_L, g_R)) = \int p(\vec{x}|\vec{y}) \cdot \delta(\vec{y} - \vec{y}(V_L, V_R, g_L, g_R)) d\vec{y}. \quad (3.3)$$

The term $p(\vec{x}|\vec{y})$ inside the integral is again a likelihood for a more general form of \vec{y}

$$-2 \ln p(\vec{x}|\vec{y}) = \sum_{i=1}^n \sum_{j=1}^n [\vec{x} - U\vec{y}]_i \mathcal{M}_{ij}^{-1} [\vec{x} - U\vec{y}]_j, \quad (3.4)$$

where $\mathcal{M}_{ij} = cov[x_i, x_j]$ is the positive-semidefinite covariance matrix and the elements U_{ij} of the $n \times N$ -matrix U are unity if the measurement x_i corresponds to the prediction y_j and zero otherwise. The likelihood $p(\vec{x}|\vec{y})$ from Equation (3.4) has a multidimensional Gaussian shape. If the prior has no uniform probabilities or if the observables or the model parameters are constrained, it is possible that the posterior differs from the Gaussian shape. If there are M sources of uncertainties, the covariance matrix is a sum of contributions of each source

$$\mathcal{M}_{ij} = \sum_{k=1}^M cov^{(k)}[x_i, x_j] = \sum_{k=1}^M \rho_{ij}^{(k)} \sigma_i^{(k)} \sigma_j^{(k)}, \quad (3.5)$$

where $\rho_{ij}^{(k)}$ is the correlation between the i^{th} and the j^{th} measurement with respect to the k^{th} uncertainty (note that $\rho_{ii}^{(k)} = 1$) and $\sigma_i^{(k)}$ is the size of the k^{th} uncertainty of the i^{th} measurement [4].

The impact of each measurement can be determined by removing it from the combination and calculating the relative increase of uncertainty⁴ of the posterior with respect to the complete combination. The same can be done with the impact of each uncertainty by comparing the relative loss of uncertainty of the posterior while removing it from the correlation [4].

³For the studies presented in this thesis, the priors are set to unity.

⁴This can be determined by the change of the volume of the smallest hyper-sphere covering a certain amount of the posterior probability.

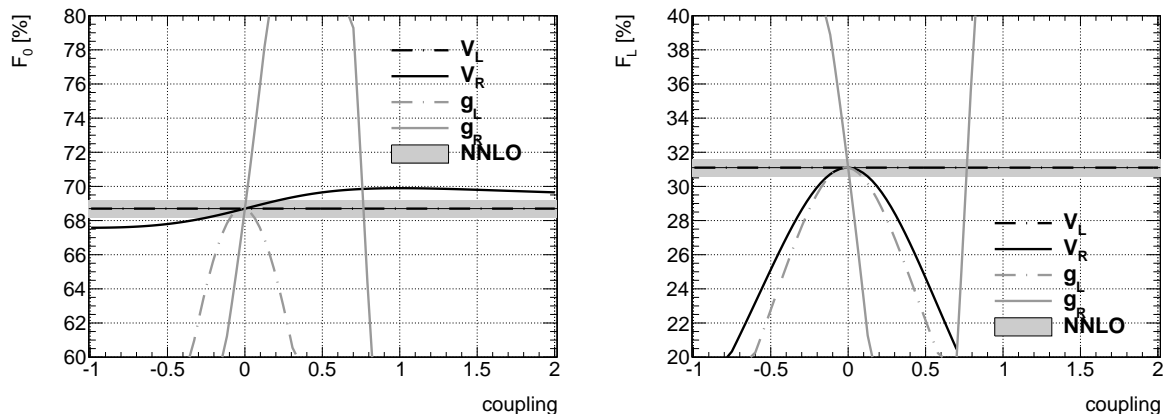


Figure 3.1: Dependence of the W boson helicity fractions F_0 (left) and F_L (right) on the anomalous couplings V_L , V_R , g_L and g_R with three couplings fixed at their Standard Model values at a time. This model is taken from Reference [8]. The wide grey band shows the expected region from NNLO calculations [96] with the black line as the favoured value. The function is matched in a way that it is equal to this prediction at $V_L = 1$ and $V_R = g_L = g_R = 0$.

3.2 Modelling of the observables

To conduct the combination as presented in Section 3.1, it is necessary to model the observables as functions of the anomalous couplings V_L , V_R , g_L and g_R . This section describes the modelling for both the W boson helicity fractions F_0 and F_L , as well as the $2 \rightarrow 2$ t -channel production cross section for top and antitop quarks. For the calculation of the models, the following parameters were used:

$$m_t = 172.5 \text{ GeV}, \quad m_b = 4.8 \text{ GeV}, \quad m_W = 80.4 \text{ GeV}, \quad \sqrt{s} = 7 \text{ TeV}, \quad (3.6)$$

where m_t , m_b and m_W are the masses of the top quark, the bottom quark and the W boson and it is assumed that the four couplings are real.

W helicity fractions The model used in the combination can be found in Reference [8]. It is used in the latest W helicity measurement from ATLAS [89] (see also Figure 1.8). The distributions for F_0 and F_L are multiplied by a constant in order to match the favoured value of the NNLO predictions [96] at $V_L = 1$ and $V_R = g_L = g_R = 0$. Assuming the couplings to be real, the expressions of the helicity fractions in this model are power series of second order in the anomalous couplings.

The dependencies of the W boson helicity fractions F_0 and F_L on the anomalous couplings in this model can be seen in Figure 3.1 with three couplings fixed at their Standard Model values at a time. The wide grey band shows the expected region from NNLO calculations

3 Combination and fitting framework

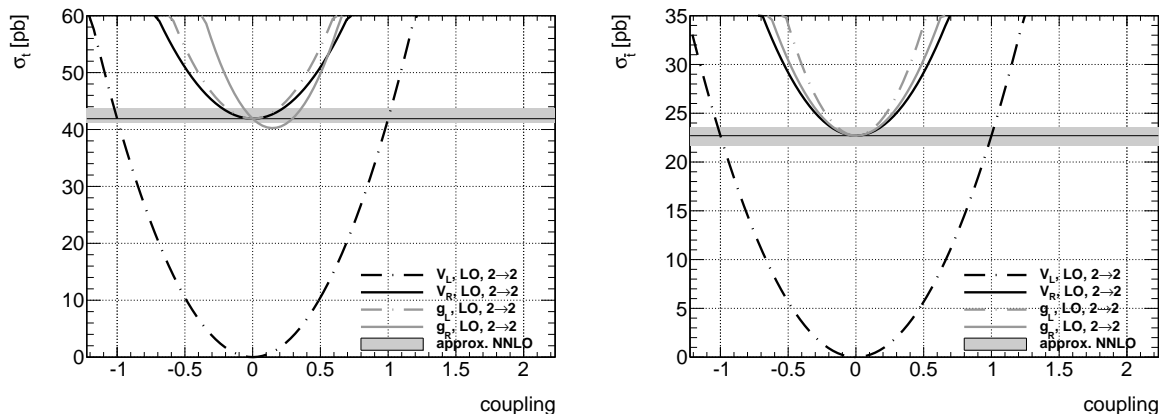


Figure 3.2: Dependence of the $2 \rightarrow 2$ t -channel production cross section for a single top (left) and antitop (right) quark on the anomalous couplings V_L , V_R , g_L and g_R with three couplings fixed at their Standard Model values at a time. This model is taken from Reference [9]. The wide grey band shows the expected region from approximate NNLO calculations [74] with the black line as the favoured value. The function is matched in a way that it is equal with this prediction at $V_L = 1$ and $V_R = g_L = g_R = 0$.

with the black line as the favoured value. The dependence of the W helicity fractions on V_L is too small to be visible in the figures and the dependence of the longitudinal fraction F_0 on V_R is also weak. In contrast, the dependence on the tensor couplings g_L and g_R (as well as on the vector coupling V_R for F_L) is much stronger. The helicity fractions as a function of g_R acquire the values of the NNLO prediction twice: at $g_R \sim 0$ and at $g_R \sim 0.75$. This explains the two areas for the tensor couplings from the latest W helicity measurement from ATLAS [89] in Figure 1.8.

$2 \rightarrow 2$ t -channel top production cross section The model used in the combination can be found in Reference [9]. The coefficients are obtained via a LO calculation using Whizard [123]. Like in the case of the W helicity fractions, the distributions are multiplied by a constant in order to match the favoured value of the approximate NNLO predictions [74] at $V_L = 1$ and $V_R = g_L = g_R = 0$. The dependence of the $2 \rightarrow 2$ t -channel top and antitop production cross sections on the anomalous couplings in this model can be seen in Figure 3.2 with three couplings fixed at their Standard Model values at a time. The wide grey band shows the expected region from approximate NNLO calculations with the black line as the favoured value.

Unlike the model of the W helicity fractions, the model of the t -channel cross section is strongly dependent on all four anomalous couplings. Additionally, this model does not allow the right-handed tensor coupling to have a value of about $g_R \sim 0.75$. Nevertheless, the model of the t -channel cross sections has an additional allowed region around $V_L \sim -1$, where it acquires the Standard Model values.

3.3 Strategy for the combination of the measurements

In this section, the strategy for obtaining the correlations between the W helicity measurement and the t -channel single top quark production cross section measurement⁵ is presented. The conventions for naming and sorting the sources of systematic uncertainties differ for the two measurements and the correlations are defined in a different way. Therefore, a way to compare the sources of systematic uncertainties of the two measurements is included in this strategy. Sorting the sources of systematic uncertainties was already done in Section 2.3.

The correlation matrix

$$\begin{aligned} \underline{\underline{\rho}} &= \begin{pmatrix} \rho(F_0, F_0) & \rho(F_0, F_L) & \rho(F_0, \sigma_t) & \rho(F_0, \sigma_{\bar{t}}) \\ \rho(F_L, F_0) & \rho(F_L, F_L) & \rho(F_L, \sigma_t) & \rho(F_L, \sigma_{\bar{t}}) \\ \rho(\sigma_t, F_0) & \rho(\sigma_t, F_L) & \rho(\sigma_t, \sigma_t) & \rho(\sigma_t, \sigma_{\bar{t}}) \\ \rho(\sigma_{\bar{t}}, F_0) & \rho(\sigma_{\bar{t}}, F_L) & \rho(\sigma_{\bar{t}}, \sigma_t) & \rho(\sigma_{\bar{t}}, \sigma_{\bar{t}}) \end{pmatrix} \\ &= \begin{pmatrix} \underline{\underline{\mathbf{A}}} & \underline{\underline{\mathbf{C}}} \\ \underline{\underline{\mathbf{C}}^T} & \underline{\underline{\mathbf{B}}} \end{pmatrix} \end{aligned} \quad (3.7)$$

is a 4×4 matrix describing the correlations between the sources of systematic uncertainties of the four observables F_0 (helicity fraction for the longitudinally polarised W bosons), F_L (helicity fraction for the left-handedly polarised W bosons), σ_t (t -channel top quark production cross section) and $\sigma_{\bar{t}}$ (t -channel antitop quark production cross section), where $\rho(x, y) = \rho(y, x)$ is the correlation between the observables x and y ($\rho(x, x) = 1$) with respect to their sources of uncertainties. The matrix $\underline{\underline{\rho}}$ can be divided into four 2×2 matrices: $\underline{\underline{\mathbf{C}}}$ and its transpose, $\underline{\underline{\mathbf{A}}}$ and $\underline{\underline{\mathbf{B}}}$. The matrices $\underline{\underline{\mathbf{A}}}$ and $\underline{\underline{\mathbf{B}}}$ describe the correlation between the two observables of one measurement, whereas $\underline{\underline{\mathbf{C}}}$ describes the correlations between two observables of the two different measurements⁶. The main challenge is the

⁵This is an abbreviation of the expression “the correlations between the measurements with respect to their sources of uncertainties”, as it is used in this thesis.

⁶The two measurements are the W helicity measurement containing the two observables F_0 and F_L , as well as the t -channel cross section measurements, containing the two observables σ_t and $\sigma_{\bar{t}}$. Therefore, $\underline{\underline{\mathbf{A}}}$ describes the correlation between F_0 and F_L and $\underline{\underline{\mathbf{B}}}$ describes the correlation between σ_t and $\sigma_{\bar{t}}$. Every element of the matrix $\underline{\underline{\mathbf{C}}}$ describes the correlation between one observable of the W helicity measurement and one observable of the t -channel cross section measurement.

3 Combination and fitting framework

determination of the matrix $\underline{\mathbf{C}}$. One 4×4 correlation matrix has to be determined for each source of systematic uncertainty and these matrices have to be combined in order to obtain the total correlation matrix.

To be able to determine the correlations between the sources of systematic uncertainties of the different observables, it is important to develop a general expression for the influence of each source of systematic uncertainty on the observables. If varying the effect of one source of systematic uncertainty up causes two observables to increase, then the two observables have a positive correlation (“are correlated”) with respect to this source. On the other hand, if increasing one source of systematic uncertainty causes one of the two observables to increase and the other one to decrease, the two observables have a negative correlation (“are anticorrelated”) with respect to this source.

The sets of sources of systematic uncertainties are different for the t -channel cross section measurement and the measurement of the W helicity fractions. Before matching these sources of systematic uncertainties into categories equivalent for both measurements, it is necessary to determine the influence of each source of systematic uncertainty on each observable to be able to determine the correlations between the sources of systematic uncertainties of the two different measurements. To achieve this, it is necessary to introduce a parameter τ , called “trend”. The trend τ is an integer that can take either the value “+1” or “-1”. If varying the effect of one source of systematic uncertainty up (down) causes the observable to increase (decrease), the trend is $\tau = +1$ and if varying the effect of one source of systematic uncertainty up (down) causes the observable to decrease (increase), the trend is $\tau = -1$. This is an approximation to be able to determine the correlations between the sources of systematic uncertainties of the different measurements. This approximation is necessary because these correlations cannot be determined exactly due to the different categorization and treatment of the systematic uncertainties of the two measurements.

The trends τ of the sources of systematic uncertainties of the two measurements are determined in the following way:

- Correlation for the W helicity measurement: The influence of the variations of the sources of systematic uncertainties on the W helicity fractions is determined using ensemble tests. Different ensembles are produced where one source of systematic uncertainty at the time is either varied up or down by 1σ , see Section 2.1. This variation causes the mean value of the observable to vary. If this variation of the

3.3 Strategy for the combination of the measurements

source of systematic uncertainty is positively correlated (negatively correlated)⁷ with the variation of the mean value of the observable, the trend of this source is set to $\tau = +1$ ($\tau = -1$) for this systematic uncertainty and this observable. There are two exceptions from this rule:

1. There are some sources of systematic uncertainties that can only be varied in one direction (called “one-sided”) because the nominal value is assigned to the optimum. Two examples for these sources are the jet energy resolution and the jet reconstruction efficiency. If a one-sided variation causes the observable to increase (decrease), the trend of this source is set to $\tau = +1$ ($\tau = -1$) for this observable.
 2. There is a correlation between the different helicity fractions because the denominator in Equation (2.2) in Section 2.1 is the same for all helicity fractions and is dependent on all three of them. This leads to the case that it is possible that both increasing and decreasing the source of systematic uncertainty leads to a variation of a helicity fraction in the same direction. In this case, the trend has to be set to $\tau = 0$.
- Correlation for the t -channel cross section measurement: The systematic uncertainties are calculated as described in Section 2.2. If the correlation between the distributions δ_i and β_i is bigger than 0.01, the trend is set to $\tau = +1$ and if the correlation is smaller than -0.01 , the trend is set to $\tau = -1$. If the correlation lies between -0.01 and 0.01 , the trend is set to $\tau = 0$ to avoid taking into account δ_i - β_i -correlations that are only non-zero due to the statistical uncertainties of the δ_i - and β_i -distributions.

The next step is to obtain the correlation and covariance matrices. First, the 2×2 correlation matrices $\underline{\mathbf{A}}$ and $\underline{\mathbf{B}}$ and the corresponding covariance matrices are computed separately for each source of systematic uncertainty. For the W helicity fractions, the

⁷In this case, “positively correlated” means that varying the source of systematic uncertainty up (down) causes the mean value of the observable to increase (decrease) and “negatively correlated” means that varying the source of systematic uncertainty up (down) causes the mean value of the observable to decrease (increase).

3 Combination and fitting framework

correlation between F_0 and F_L is determined via the formula⁸

$$\rho(F_L, F_0) = \frac{\Delta F_R^2 - \Delta F_L^2 - \Delta F_0^2}{2\Delta F_L \Delta F_0}, \quad (3.8)$$

where ΔF_i ($i = 0, L, R$) is the uncertainty of the W helicity fraction F_i . To compute the off-diagonal elements of the correlation matrix for the t -channel cross section measurement $\rho(\sigma_t, \sigma_{\bar{t}})$, the correlation factor between the δ_i distributions of the top and antitop cross section has to be determined for each source of systematic uncertainty i . The diagonal elements are set to one for both measurements.

The 2×2 covariance matrices corresponding to $\underline{\underline{\mathbf{A}}}$ and $\underline{\underline{\mathbf{B}}}$ are calculated by the formula

$$\mathcal{M}_{\text{diag}}(x, y) = \begin{pmatrix} (\Delta x)^2 & \rho(x, y) \cdot \Delta x \cdot \Delta y \\ \rho(y, x) \cdot \Delta y \cdot \Delta x & (\Delta y)^2 \end{pmatrix}, \quad (3.9)$$

where Δx and Δy are the uncertainties of the observables x and y (F_0 and F_L or σ_t and $\sigma_{\bar{t}}$) corresponding to the source of systematic uncertainty. For the W helicity fractions (not one-sided), they are symmetrised by taking the highest uncertainty as the value for up and down. For the cross section and one-sided W helicity uncertainties, the value is taken for the up and down uncertainty.

For each category⁹, the 2×2 covariance matrices of the related sources of systematic uncertainties are summed up for both measurements. The uncertainties of the categories are the square roots of the diagonal elements of the two summed up covariance matrices, similar to Equation (3.9).

The next step is to compute the off-diagonal 2×2 correlation matrix

$$\begin{aligned} \underline{\underline{\mathbf{C}}} &= \begin{pmatrix} \rho(F_0, \sigma_t) & \rho(F_0, \sigma_{\bar{t}}) \\ \rho(F_L, \sigma_t) & \rho(F_L, \sigma_{\bar{t}}) \end{pmatrix} \\ &= \begin{pmatrix} \tau_{\text{imp}}(F_0) \cdot \tau_{\text{imp}}(\sigma(t)) & \tau_{\text{imp}}(F_0) \cdot \tau_{\text{imp}}(\sigma(\bar{t})) \\ \tau_{\text{imp}}(F_L) \cdot \tau_{\text{imp}}(\sigma(t)) & \tau_{\text{imp}}(F_L) \cdot \tau_{\text{imp}}(\sigma(\bar{t})) \end{pmatrix}, \end{aligned} \quad (3.10)$$

⁸This formula was derived assuming $F_R = 1 - F_0 - F_L$ and therefore $\Delta F_R^2 = \Delta F_L^2 + \Delta F_0^2 + 2\rho(F_L, F_0) \cdot \Delta F_L \Delta F_0$. In some cases (e.g. for small uncertainties, where fluctuations are of the same order of magnitude as the actual value), the correlation can be above (below) $(-)$ 1. In these cases, correlations above (below) $(-)$ 0.99 are set to $(-)$ 0.99. Higher (lower) correlations than $(-)$ 0.99 can lead to technical issues performing the combination.

⁹The categories of the sources of systematic uncertainties are defined in Section 2.3.

3.3 Strategy for the combination of the measurements

where $\tau_{\text{imp}}(x)$ is the trend of the “most important” source of systematic uncertainty of the category, corresponding to the observable x . For the W helicity fractions, $\Delta F_0^2 + \Delta F_L^2$ has to be maximal and for the t -channel cross section, $\Delta\sigma_t^2 + \Delta\sigma_{\bar{t}}^2$ has to be maximal to be the “most important” source of systematic uncertainty of the category. Due to its construction, the correlations $\rho(x, y)$ from the matrix $\underline{\mathbf{C}}$ can either be -1 , 0 or 1 . The trend τ is used to approximate the correlations between the sources of systematic uncertainties of the two measurement due to the fact that the systematic uncertainties are described in different ways in the references of the two measurements.

The corresponding 2×2 off-diagonal covariance matrix is determined by

$$\mathcal{M}_{\text{off}} = \begin{pmatrix} \rho(F_0, \sigma_t) \cdot \Delta F_0 \cdot \Delta\sigma_t & \rho(F_0, \sigma_{\bar{t}}) \cdot \Delta F_0 \cdot \Delta\sigma_{\bar{t}} \\ \rho(F_L, \sigma_t) \cdot \Delta F_L \cdot \Delta\sigma_t & \rho(F_L, \sigma_{\bar{t}}) \cdot \Delta F_L \cdot \Delta\sigma_{\bar{t}} \end{pmatrix}. \quad (3.11)$$

The 4×4 covariance matrix for each category of sources of systematic uncertainties constructed as

$$\mathcal{M}_{\text{sys}} = \begin{pmatrix} \mathcal{M}_{\text{diag}}(F_0, F_L) & \mathcal{M}_{\text{off}} \\ \mathcal{M}_{\text{off}} & \mathcal{M}_{\text{diag}}(\sigma_t, \sigma_{\bar{t}}) \end{pmatrix}. \quad (3.12)$$

The 4×4 covariance matrix for all sources of systematic uncertainties $\mathcal{M}_{\text{sys}}^{\text{tot}}$ is obtained by summing up all 4×4 covariance matrices of each category. The 4×4 correlation matrix of all sources of systematic uncertainties is computed by dividing the matrix elements of the covariance matrix $\mathcal{M}_{\text{sys}}^{\text{tot}}$ by the square roots of its diagonal elements, representing the total systematic uncertainties of all categories¹⁰, according to Equations (3.9) and (3.11). Next, the correlation matrices of the statistical uncertainties and the uncertainties of the Standard Model prediction are determined. For the statistical uncertainties, the correlation matrix from Table 3.1 is chosen. The correlation between the two statistical uncertainties of the W helicity fractions is determined via Equation (3.8), where $\Delta F_0^{\text{stat}} = 0.022$, $\Delta F_L^{\text{stat}} = 0.014$ and $\Delta F_R^{\text{stat}} = 0.010$ [6]. For the uncertainty of the Standard Model prediction, the correlation between F_0 and F_L is set to -0.99 in the same way¹¹ using $\Delta F_0^{\text{SM}} = 0.005$, $\Delta F_L^{\text{SM}} = 0.005$ and $\Delta F_R^{\text{SM}} = 0.0001$ [96]. The other off-diagonal entries of these correlation matrices are set to zero. To determine the results including these two additional uncertainties, the covariance matrices of the statistical and the Standard Model uncertainties are computed as shown in Equation (3.9) and (3.11) and added to the covariance matrix of all sources of systematic uncertainties. From this total

¹⁰Note that this is not the total systematic uncertainty quoted in Table 2.1, as explained in Section 2.3.

¹¹Actually, the correlation is -0.9998 but it is set to -0.99 to match the convention.

3 Combination and fitting framework

	F_0	F_L	σ_t	$\sigma_{\bar{t}}$
F_0	1	-0.942	0	0
F_L	-0.942	1	0	0
σ_t	0	0	1	0
$\sigma_{\bar{t}}$	0	0	0	1

Table 3.1: Correlation matrix for the statistical uncertainties of the four observables.

covariance matrix, the total correlation matrix and the total uncertainties can be obtained as described above (see again Equation (3.9) and (3.11)) for the systematic uncertainties.

This combination is an approximation due to the concept of the trend. However, this is necessary because the provided data does not allow an exact determination of the correlations between the sources of uncertainties of the W helicity and the cross section measurement. The choice of categorisation has an effect on the total off-diagonal correlation matrix $\underline{\underline{\mathbf{C}}}$. Splitting a category into two, e.g. JES and b-JES, causes the biggest uncertainty of each category to contribute to the total off-diagonal correlation matrix. If both categories would be merged into one, only be the biggest uncertainty of both categories together would contribute to the total off-diagonal correlation matrix and the other uncertainty would not. Nevertheless, the choice of categorisation does not affect the total on-diagonal correlation matrices $\underline{\underline{\mathbf{A}}}$ and $\underline{\underline{\mathbf{B}}}$ because the trend is not involved in the determination of their correlations. Therefore, categories only described by one measurement or with no correlation between the two measurements can be merged without loss of information.

4 Standard setup of the analysis

In this chapter, the total uncertainties, the total correlation matrix resulting from the combination and the ranges of the fits are presented. The total uncertainties and total correlation matrix are determined as described in Sections 2.3 and 3.3 and will be used from now on in the sensitivity studies (Chapter 5) and in the evaluation of the experimental values (Chapter 6). Some entries of the total correlation matrix are varied from these standard values for some of the sensitivity studies.

The total uncertainties of the observables are

$$\begin{aligned} \Delta F_0^{\text{total}} &= 0.0314, & \Delta F_L^{\text{total}} &= 0.0226, \\ \left(\frac{\Delta\sigma_t}{\sigma_t}\right)^{\text{total}} &= 0.130 & \text{and} & \left(\frac{\Delta\sigma_{\bar{t}}}{\sigma_{\bar{t}}}\right)^{\text{total}} = 0.164. \end{aligned} \quad (4.1)$$

They contain the total uncertainties of the measurements taken directly from the References¹ [6] and [7] and the uncertainties of the Standard Model prediction of the observables [74, 96], all shown in Table 2.1. The total correlation matrix is shown in Table 4.1. The correlation between the sources of uncertainties of the two W helicity fraction observables is as expected. Other values quoted for this correlation are e.g. -0.96 [89] and

	F_0	F_L	σ_t	$\sigma_{\bar{t}}$
F_0	1	-0.834	0.222	0.265
F_L	-0.834	1	-0.118	-0.164
σ_t	0.222	-0.118	1	0.375
$\sigma_{\bar{t}}$	0.265	-0.164	0.375	1

Table 4.1: Total correlation matrix between the sources of uncertainties of the four observables. It contains the combined systematic uncertainties, the statistical uncertainties and the uncertainties from the Standard Model prediction.

¹For the t -channel single top production cross section, the statistical and the total systematic uncertainties are added quadratically, while for the W helicity fraction measurement, the uncertainty from the profile likelihood fit is taken.

4 Standard setup of the analysis

-0.86 [92]. The correlation² between the sources of systematic uncertainties of the two measurements ranges from 11.8% to 26.5%.

Table 4.2 lists the different ranges of the one-, two- and four-dimensional fits used for the studies in the Chapters 5 and 6. The binning for the one- and two-dimensional fits is 400 bins for each dimension and for the four-dimensional fits, the binning is 200 bins for each dimension. The ranges of the plots are very important for fits of the W helicity measurement, because its observables are unconstrained in the direction of the left-handed vector coupling V_L . Therefore, the posterior distributions from the fits of this measurement including V_L are dependent on the range of these fits. The same applies to the ranges of the fits for the B -physics measurement³.

²The convention of how the alternating sign is treated is shown below in Table 5.3 in Section 5.4.

³This additional measurement is introduced in Section 5.6.

Fit	V_L	V_R	g_L	g_R
W helicity fractions only, 1D	$[-1.5, 1.5]$	$[-0.8, -0.8]$	$[-0.4, 0.4]$	$[-0.3, 1.0]$
t -channel cross section only, 1D	$[-1.5, 1.5]$	$[-1.0, -1.0]$	$[-0.8, 0.8]$	$[-0.7, 0.9]$
both combined, 1D	$[-1.5, 1.5]$	$[-0.8, -0.8]$	$[-0.4, 0.4]$	$[-0.2, 0.2]$
B -physics only, 1D	$[0.7, 1.3]$	$[-0.0045, 0.0055]$	$[-0.003, 0.0025]$	$[-1, 1.25]$
top and B -physics combined, 1D	$[0.75, 1.2]$	$[-0.005, 0.005]$	$[-0.0035, 0.003]$	$[-0.2, 0.2]$
W helicity fractions only, V_L - V_R , 2D	$[-1.5, 1.5]$	$[-1.125, 1.125]$		
W helicity fractions only, V_L - g_L , 2D	$[-1.5, 1.5]$		$[-0.75, 0.75]$	
W helicity fractions only, V_L - g_R , 2D	$[-1.5, 1.5]$			$[-2.3, 3.24]$
W helicity fractions only, V_R - g_L , 2D		$[-1.5, 1.5]$	$[-1.0, 1.0]$	
W helicity fractions only, V_R - g_R , 2D		$[-1.5, 1.5]$		$[-1.0, 1.2]$
W helicity fractions only, g_L - g_R , 2D			$[-1.0, 1.0]$	$[-1.0, 1.2]$
t -channel cross section only, V_L - V_R , 2D	$[-1.5, 1.5]$	$[-1.2, 1.2]$		
t -channel cross section only, V_L - g_L , 2D	$[-1.5, 1.5]$		$[-1.0, 1.0]$	
t -channel cross section only, V_L - g_R , 2D	$[-1.5, 1.5]$			$[-2.3, 3.24]$
t -channel cross section only, V_R - g_L , 2D		$[-1.6, 1.6]$	$[-1.33, 1.33]$	
t -channel cross section only, V_R - g_R , 2D		$[-1.6, 1.6]$		$[-1.0, 1.2]$
t -channel cross section only, g_L - g_R , 2D			$[-1.33, 1.33]$	$[-1.0, 1.2]$
both combined, V_L - V_R , 2D	$[-1.5, 1.5]$	$[-0.75, 0.75]$		
both combined, V_L - g_L , 2D	$[-1.5, 1.5]$		$[-0.45, 0.45]$	
both combined, V_L - g_R , 2D	$[-1.5, 1.5]$			$[-0.92, 0.81]$
both combined, V_R - g_L , 2D		$[-1.0, 1.0]$	$[-0.6, 0.6]$	
both combined, V_R - g_R , 2D		$[-1.0, 1.0]$		$[-0.4, 0.3]$
both combined, g_L - g_R , 2D			$[-0.6, 0.6]$	$[-0.4, 0.3]$
B -physics only, V_L - V_R , 2D	$[-1.5, 1.5]$	$[-0.06, 0.03]$		
B -physics only, V_L - g_L , 2D	$[-1.5, 1.5]$		$[-0.01, 0.03]$	
B -physics only, V_L - g_R , 2D	$[0.5, 1.5]$			$[-0.4, 0.4]$
B -physics only, V_R - g_L , 2D		$[-0.004, 0.004]$	$[-0.005, 0.005]$	
B -physics only, V_R - g_R , 2D		$[-0.01, 0.01]$		$[-0.5, 0.5]$
B -physics only, g_L - g_R , 2D			$[-0.005, 0.005]$	$[-0.5, 0.5]$
top and B -physics combined, V_L - V_R , 2D	$[-1.5, 1.5]$	$[-0.06, 0.03]$		
top and B -physics combined, V_L - g_L , 2D	$[-1.5, 1.5]$		$[-0.01, 0.03]$	
top and B -physics combined, V_L - g_R , 2D	$[0.5, 1.5]$			$[-0.4, 0.4]$
top and B -physics combined, V_R - g_L , 2D		$[-0.004, 0.004]$	$[-0.005, 0.005]$	
top and B -physics combined, V_R - g_R , 2D		$[-0.01, 0.01]$		$[-0.4, 0.3]$
top and B -physics combined, g_L - g_R , 2D			$[-0.005, 0.005]$	$[-0.4, 0.3]$
t -channel cross section only, 4D	$[-1.5, 1.5]$	$[-1.5, 1.5]$	$[-1.0, 1.0]$	$[-1.0, 1.0]$
both combined, 4D	$[-1.5, 1.5]$	$[-1.5, 1.5]$	$[-1.0, 1.0]$	$[-1.0, 1.0]$

Table 4.2: Ranges of the different one-, two- and four-dimensional (1D, 2D and 4D) fits. For the two-dimensional distributions, the fitted couplings are listed, while the other two couplings are fixed at their Standard Model values.

5 Sensitivity studies using pseudo data

This section shows studies of the framework described in Section 3 using pseudo data and ensemble tests, demonstrating its capabilities. The bounds on anomalous couplings resulting from such an ensemble test are the average bounds expected if the anomalous couplings would acquire their Standard Model values, allowing the results of the measurements to fluctuate according to their assumed uncertainties. Therefore, it is referred to as the “expected” distribution. The setup of these ensemble tests can be the standard setup described in Chapter 4 or a variation of it. Each set of pseudo data contains possible results of the measurements, conducted under the same conditions as the measurements presented in Chapter 2, assuming the anomalous couplings to acquire their Standard model values and allowing the results to fluctuate according to their uncertainties. The setup of the pseudo data sets can be the standard setup or a variation of it. Each set is therefore a part of the ensemble test.

Section 5.1 describes the generation of the pseudo data. In Section 5.2, it will be shown how much the smallest credibility level (C.L.) intervals of the two dimensional fits of the anomalous couplings improve by combining the W helicity fraction measurement with the t -channel cross section measurement. The next step, presented in Section 5.3, is to compare fits of some randomly chosen sets of pseudo data with the outcome of the ensemble test for the combination of the two top quark measurements to give some examples of typical deviations of (pseudo) measurements from the expectation. In Section 5.4, the effect of the correlations between the sources of uncertainties of the two measurements on the smallest C.L. intervals of g_L and g_R are studied to show the importance of an exact determination of these correlations. Following, in Section 5.5, it is discussed if it is necessary to treat the top and antitop cross section measurements as two different measurements or if both cross sections can be summed up to an inclusive cross section to treat the two measurements as one. The last section in this chapter (Section 5.6) contains the study on the combination of the two top quark measurements with the branching

ratio measurement of the process $\bar{B} \rightarrow X_s \gamma$ and its effect on the smallest C.L. intervals of the fits of the anomalous couplings. For all of these studies, the anomalous couplings are assumed to be real.

In this chapter, if not mentioned differently, “the Standard Model values” means in fact “the Standard Model values of the anomalous Wtb couplings”.

5.1 Generation of the pseudo data

Each sample of the pseudo data contains pseudo measurements. These are pseudo measurements of the observables F_0 , F_L , top and antitop t -channel cross section. For the studies conducted in Section 5.6, pseudo measurements for the branching ratio of the process $\bar{B} \rightarrow X_s \gamma$ are created, which is described in that section. The uncertainties and their correlations are taken from Chapter 4.

The pseudo data is created by choosing random numbers from a multidimensional Gaussian distribution $P(\vec{x})$ around zero

$$P(\vec{x}) = \frac{1}{(2\pi)^{n/2} \sqrt{|\mathcal{M}|}} \exp\left(-\frac{1}{2} \vec{x} \mathcal{M}^{-1} \vec{x}\right), \quad (5.1)$$

using the covariance matrix¹ \mathcal{M} obtained from the uncertainties and the correlation matrix in Chapter 4. The vector \vec{x} contains all n total uncertainties of the observables considered for the corresponding ensemble test. To obtain the mean value for each observable from the pseudo measurement, the corresponding random number is added to the “Standard Model” mean value of the observable. The size of the uncertainty is not affected by the random number.

The “Standard Model” mean values used for generating the pseudo data for the top quark observables are the values from the models in Section 3.2 with the couplings set to the Standard Model value ($V_L = 1$, $V_R = g_L = g_R = 0$). The Standard Model values are [74, 96]

$$\begin{aligned} F_0 &= 68.7\% , & F_L &= 31.1\% , \\ \sigma_t &= 41.9 \text{ pb} & \text{and} & & \sigma_{\bar{t}} &= 22.7 \text{ pb} . \end{aligned} \quad (5.2)$$

The ensemble tests consist of the fits of 1000 pseudo data sets each. To get the distributions of posterior probabilities from the ensemble test as the expectation of the fit, the obtained distributions from the fits of each pseudo data set are summed up.

¹The expression $|\mathcal{M}|$ is the determinant of the covariance matrix.

5.2 Combination of both observables

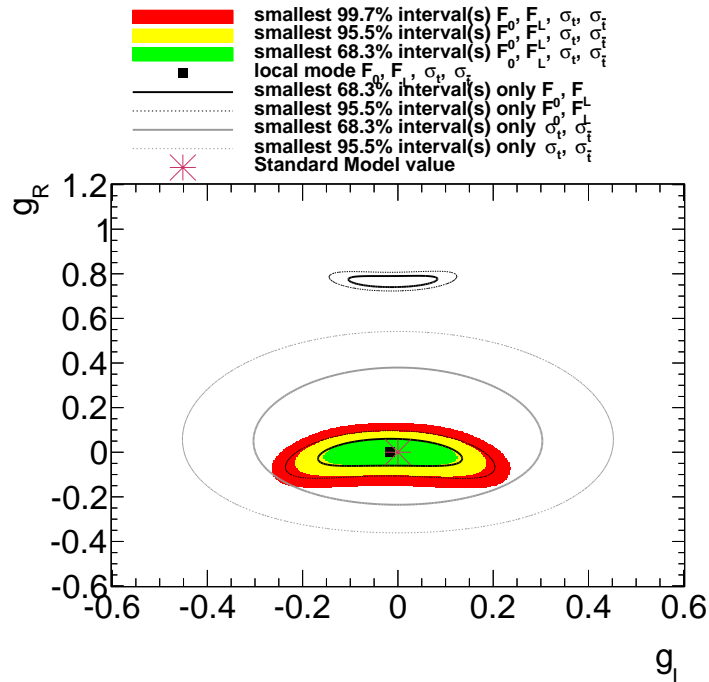


Figure 5.1: Comparison between the ensemble test results of the posterior probabilities of the g_L - g_R -distributions with $V_L = 1$ and $V_R = 0$ from the separate fits of the W helicity measurement (black lines), the t -channel cross section measurement (grey lines) and from the combination of both measurements (coloured contour plot), using the correlation matrix from Table 4.1.

In this section, the outcome of three different ensemble tests are compared. The first ensemble test describes the fit only of the W helicity measurement, the second one describes the fit only of the t -channel cross section measurement. The third ensemble test describes the fit of the combination of the two measurements.

Figure 5.1 shows the comparison between the posterior probabilities of the g_L - g_R -distributions (vector couplings set to $V_L = 1$ and $V_R = 0$) from the separate ensemble tests of the W helicity measurement, the t -channel cross section measurement and from the combination of both measurements, assuming the correlation matrix from Table 4.1. The combination was conducted as described in Section 3.1. The posterior probability from the W helicity fractions as the only input of the fit shows resemblances with the result from References [89] and [92], see Figures 1.8 and 1.9. In all three plots, the second “island” around $g_L \sim 0$, $g_R \sim 0.8$ is clearly visible, as predicted in Section 3.2, while the first “island” is consistent with the Standard Model values of the anomalous

couplings. For the posterior probability from the t -channel cross sections as the only input of the fit, this “island” does not exist, but the overall area of the smallest 68.3% C.L. interval, consistent with the Standard Model values, is much larger than for the W helicity fractions. When combining the two measurements, the second “island” from the fit to the W helicity measurement disappears and the posterior distribution around the Standard Model values gets narrower. Therefore, the combination of the measurements will exclude a large fraction of the available parameter space which both single measurements will not be able to exclude.

The comparison between the other two-dimensional distributions (with the other two couplings fixed to their Standard Model values) are shown in Figure 5.2. The posterior distributions from the W helicity measurement in the Subfigures 5.2a, 5.2b and 5.2c are dependent on the ranges of the fits because they are unconstrained in the direction of V_L . The range of these fits for V_L is chosen to be $[-1.5, 1.5]$. For all of the six two-dimensional plots, the improvement of the combination towards the fits of the separate measurements is clearly visible. Additional to the comparison of the g_L - g_R -distribution, which is also shown in Subfigure 5.2f, the comparisons of the other distributions yield the following conclusions:

- V_R - g_R -distribution (Subfigure 5.2e): This distribution looks similar to the g_L - g_R -distribution presented above, where the right-handed vector coupling V_R behaves similar to the left-handed tensor coupling g_L . The W helicity measurement also allows a second 68.3% C.L. region around $V_R \sim 0$ and $g_R \sim 0.8$, while the other 68.3% C.L. region is consistent with the Standard Model values. The smallest 68.3% C.L. region from the cross section measurement is wider than the smallest 68.3% C.L. region from the W helicity measurement but does not have a second “island” around $V_R \sim 0$ and $g_R \sim 0.8$. Combining these two measurements causes the second “island” from the fit to the W helicity fractions to vanish and the bounds on the couplings become much narrower compared to the fit to the t -channel cross sections.
- V_L - V_R -, V_L - g_L - and V_L - g_R -distributions (Subfigures 5.2a, 5.2b and 5.2c): The posterior distributions from the fits of the W helicity measurement are unconstrained in the direction of V_L , so the distributions depend on the ranges of the fits (see above). Nevertheless, the smallest 68.3% C.L. regions from the W helicity fractions are consistent with the Standard Model values for a fit with the range of $-1.5 \leq V_L \leq 1.5$. The cross section measurement allows two half-moon-shaped smallest 68.3% C.L. regions in each of the three plots. One of them is always consistent with $V_L \sim -1$, as predicted in Section 3.2, with the other coupling to be approximately

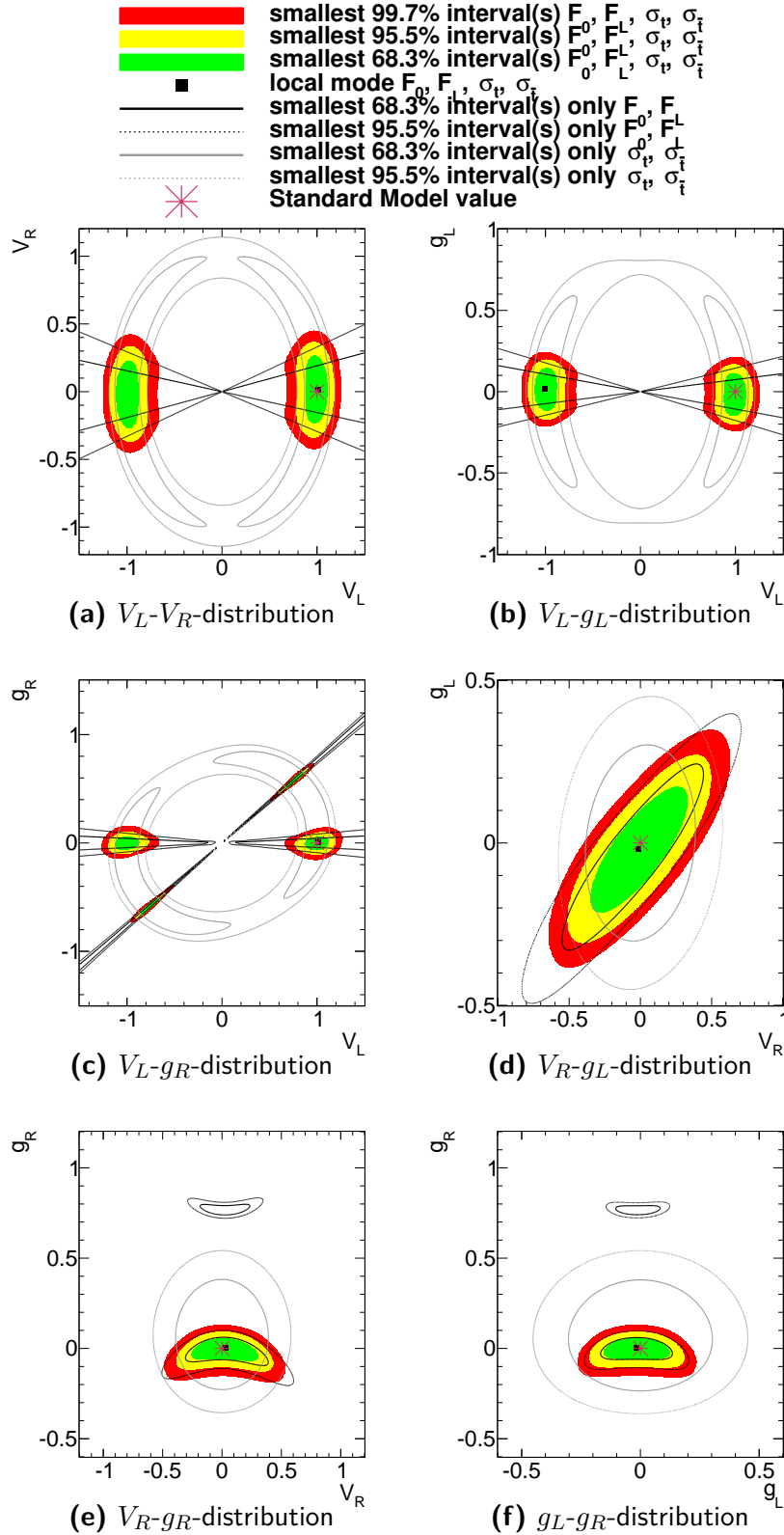


Figure 5.2: Comparison between the ensemble test results of the posterior distributions from the separate two-dimensional fits of the W helicity measurement (black lines), the t -channel cross section measurement (grey lines) and from the combination of both measurements (coloured contour plot), using the correlation matrix from Table 4.1. The other two couplings are fixed to their Standard Model values.

zero, while the other region is always consistent with the Standard Model values. The combination yields a big improvement: The cross section measurement constrains the distributions along the axis of V_L , while the W helicity measurement further constrains the distributions along the axis of the other couplings. For the V_L - V_R - and V_L - g_L -distributions, there are two smallest 68.3% C.L. regions each, which are much narrower than considering only the cross section measurement. One region is consistent with $V_L \sim -1$ and a vanishing of the other coupling, while the other one consistent with the Standard Model values. For the V_L - g_R -distribution, there are now four smallest 68.3% C.L. regions; one around $V_L \sim -1$ and $g_R \sim 0$, one around $V_L \sim -0.8$ and $g_R \sim -0.6$, one around $V_L \sim 0.8$ and $g_R \sim 0.6$ and one consistent with the Standard Model values.

- V_R - g_L -distribution (Subfigure 5.2d): The smallest 68.3% C.L. region for the combined measurements is much narrower than the smallest 68.3% C.L. regions for the separate measurements. The W helicity measurement constrains the left-handed tensor coupling g_L stronger than the cross section measurement, while the cross section measurement constrains the right handed vector coupling V_R stronger than the W helicity measurement. All three smallest 68.3% C.L. regions are consistent with the Standard Model values.

It can be seen in these figures that the local mode is not identical to the Standard Model value of the anomalous couplings, as it would be for the posterior distribution of measurements measuring exactly the Standard Model values. The reason is that the model of the W helicity fractions in dependence on the anomalous couplings is not symmetric around the Standard Model values, see Figure 3.1. This asymmetry has a stronger effect on V_R and g_L for smaller W helicity fractions, causing more asymmetric posterior distributions with a local mode deviating more from the Standard Model value than for bigger W helicity fractions². Half of the values for F_0 and F_L from the pseudo data are higher than the Standard Model value and the other half is smaller, so for the average distributions shown in Figures 5.1 and 5.2, the local mode is not identical with the Standard Model values of the couplings.

Table 5.1 shows the smallest 95% C.L. bounds from the one-dimensional fits of the anomalous couplings from these ensemble tests, where three couplings are fixed to their Standard Model values for each fit. It also includes the numerical uncertainties, estimated from the range and the binning of the posterior distributions. It shows again that the

²The model is also asymmetric in dependence on g_R but the effect on the local mode is too small to be visible in the plots. This is because the model in dependence on g_R does not have its maximum or minimum at the Standard Model value, as it is for V_R and g_L .

observables \rightarrow	$F_0, F_L, \sigma_t, \sigma_{\bar{t}}$		only F_0, F_L		only $\sigma_t, \sigma_{\bar{t}}$	
smallest 95% C.L. bounds	lower bounds	upper bounds	lower bounds	upper bounds	lower bounds	upper bounds
$V_L - 1$	-0.17(1)	0.17(1)	-	-	-0.19(1)	0.17(1)
	-2.16(1)	-1.82(1)			-2.17(1)	-1.81(1)
V_R	-0.27(1)	0.31(1)	-0.29(1)	0.33(1)	-0.52(1)	0.53(1)
g_L	-0.17(1)	0.14(1)	-0.18(1)	0.14(1)	-0.41(1)	0.41(1)
g_R	-0.085(1)	0.081(1)	-0.08(1)	0.08(1)	-0.31(1)	0.51(1)
			0.73(1)	0.80(1)		

Table 5.1: The smallest 95% C.L. bounds from the one-dimensional fits of the anomalous couplings from the ensemble tests of the W helicity measurement, the t -channel cross section measurement and both measurements combined, where three couplings are fixed to the Standard Model values at the time. The numerical uncertainties shown here are estimated from the range and the binning of the posterior distributions.

W helicity fractions are not sensitive to the left-handed vector coupling V_L and allow two smallest 95% C.L. regions for the right-handed tensor coupling g_R (around $g_R \sim 0$ and around $g_R \sim 0.8$). The t -channel cross sections again allow two regions for V_L (one around $V_L \sim 1$ and one around $V_L \sim -1$). The smallest 95% C.L. bounds on V_R , g_L and g_R from the W helicity measurement are narrower than the bounds from the cross section measurement. The combination of both measurements constrains all anomalous couplings. Furthermore, there are still two allowed regions for V_L but only one allowed region for g_R . Apart from this, the bounds on V_R , g_L and g_R compared to the fit to the W helicity fractions only, as well as on V_L compared to the fit to the t -channel cross sections do not get narrower within the numerical uncertainties. All of these bounds are consistent with the Standard Model values.

5.3 Expectation compared to pseudo data fits

If the distributions for the real measurement deviate from the expectation shown in Figure 5.1, it is still possible that this is caused by the deviations due to statistical and systematic uncertainties. This section shows how much the actual outcome of the fits can deviate from its expectation due to the uncertainties. Six pseudo data sets are randomly picked from the ensemble test. The outcome of the fits from each of these pseudo data sets is compared to the outcome of the ensemble test. The pseudo data used here represents the

Set #	F_0 [%]	F_L [%]	σ_t [pb]	$\sigma_{\bar{t}}$ [pb]
1	64.6	35.9	50.1	22.3
2	73.5	28.6	46.8	30.3
3	63.0	34.9	40.8	22.0
4	69.4	30.3	43.2	24.8
5	64.4	34.0	46.0	29.3
6	70.4	29.4	38.4	21.7
SM	68.7	31.1	41.9	22.7

Table 5.2: Mean values of the observables from the six randomly chosen pseudo data sets in comparison with the Standard Model values from References [74] and [96]. The uncertainties of these values, as well as the correlation matrix are shown in Chapter 4.

combination of the two top quark measurements with the setup presented in Chapter 4. Figure 5.3 (for the g_L - g_R -distributions), as well as Figures A.1-A.5, (for the other distributions) show comparisons between the outcome of the ensemble tests and the six randomly picked pseudo data sets. The mean values of the observables in these samples are shown in Table 5.2. The black lines indicate the smallest credibility level intervals of the ensemble test result while the coloured contour plots indicate the distributions from the fits of the randomly picked pseudo data sets.

The outcome of the ensemble test, being the average distribution, marks the expected result of a measurement in the case that the Standard Model values from References [74, 96] are the exact values existing in nature. The randomly picked pseudo data sets represent outcomes of measurements influenced by the uncertainties from (4.1). The deviation between the distributions from pseudo data and the ensemble test result makes it obvious that the outcome of the combination has a strong dependence on possible deviations due to the statistical and systematic uncertainties of the measurement. Nevertheless, all smallest 68.3% C.L. intervals from the single pseudo data sets and the ensemble test overlap in all of the six examples. For set #1, the Standard Model values of the anomalous couplings do not lie within the smallest 95.5% C.L. intervals for the g_L - g_R -, V_L - g_R - and V_R - g_R -distributions but they still lie inside the smallest 99.7% C.L. intervals. For the other distributions of the six pseudo data samples, the smallest 95.5% C.L. intervals are consistent with the Standard Model values of the anomalous couplings.

The distributions from the ensemble tests are slightly wider than the ones from the randomly picked pseudo data samples. The reason is that the distribution from the ensemble test is the average of 1000 distributions from pseudo data, which can in fact

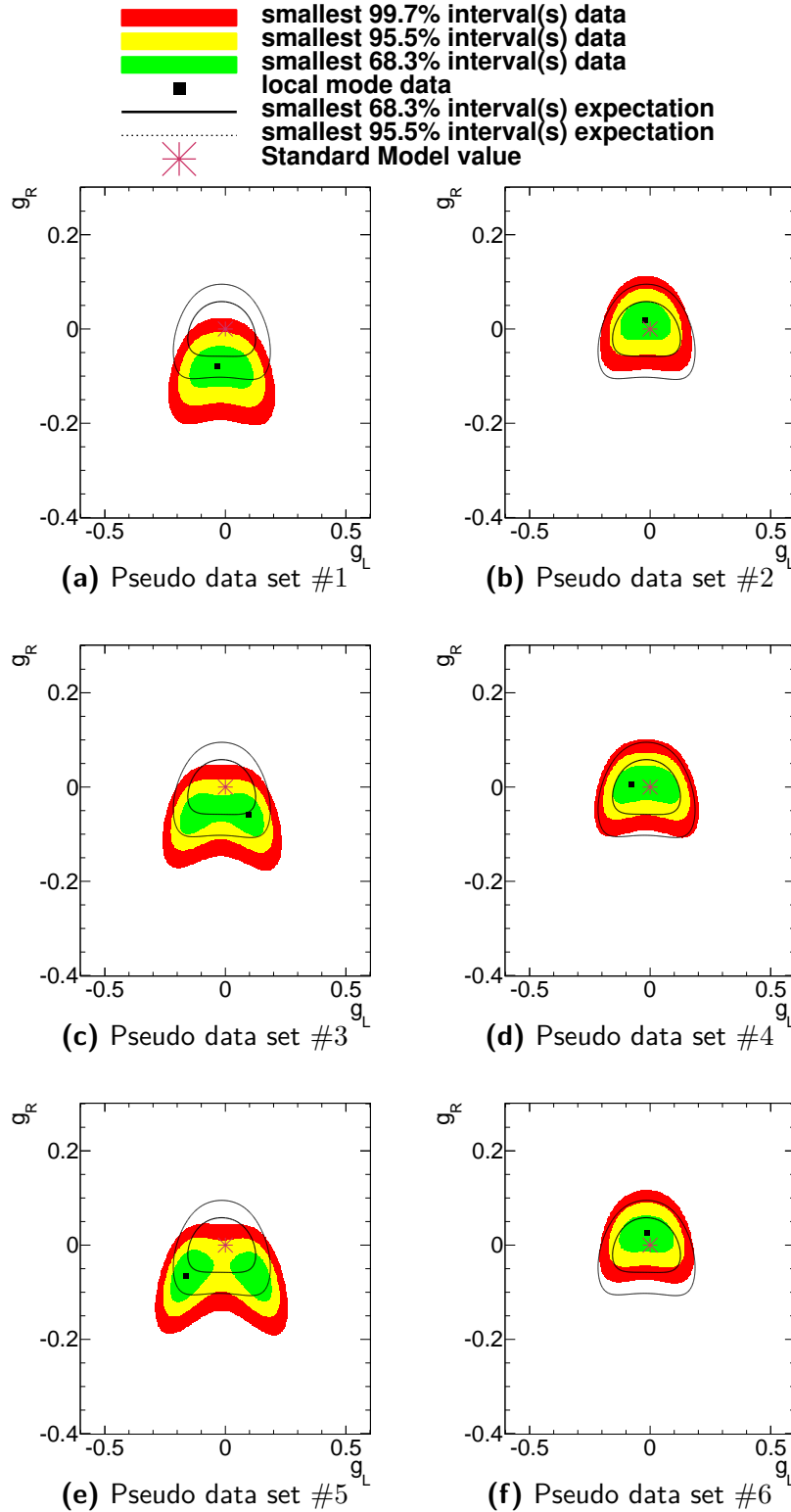


Figure 5.3: Comparison between the posterior probability from the two-dimensional fits of g_L and g_R with $V_L = 1$ and $V_R = 0$ from the ensemble test (“expectation”, black lines) and six randomly picked pseudo data sets (“data”, coloured contour plots). The mean values of the observables are shown in Table 5.2, the uncertainties and the correlation matrix in Chapter 4.

	σ_t	$\sigma_{\bar{t}}$
F_0	ρ	ρ
F_L	$-\rho$	$-\rho$

Table 5.3: Definition of the correlation ρ between the sources of uncertainties of the observables from the W -helicity measurement (F_0 and F_L) and the t -channel cross section measurement (σ_t and $\sigma_{\bar{t}}$) in Section 5.4. The minus sign appears because F_0 and F_L are anticorrelated.

be wider than a single distribution from a pseudo data set. This is acceptable, as long the ensemble test result is interpreted as the average result and not as the most likely distribution.

5.4 Effect of the correlation

An important feature of this combination is the determination of the correlations between the sources of systematic uncertainties of the W helicity and the t -channel cross section measurement as shown in Sections 2.3 and 3.3. In this section, the influence of this correlation is studied.

Figure 5.4 shows the smallest intervals from the two-dimensional fits of the anomalous left-handed and right-handed tensor coupling g_L and g_R in dependence on the correlation ρ (see Table 5.3) between the sources of uncertainties from the W helicity measurement and the cross section measurement³ using ensemble tests. The vector couplings are fixed to $V_L = 1$ and $V_R = 0$. While the one coupling is plotted in dependence of the correlation, the other coupling is integrated over to be removed from the plot. The correlation was varied from -70% up to 70% in steps of 10% . For each correlation, 1000 pseudo measurements were created. The widths of the smallest limits are maximal for a correlation of $\rho \sim -30\%$ and minimal for $\rho \sim 70\%$ inside the observed interval. This is an example of how correlations will affect the resulting bounds on anomalous couplings from the fits of the combination. Figure 5.5a shows the comparison between two two-dimensional fits of g_L and g_R from ensemble tests: The coloured contour plot is the distribution taking into account the correlation matrix from Table 4.1. The black line indicates the smallest credibility level intervals of the distribution setting the correlation ρ between the uncertainties of the

³Because F_0 and F_L are anticorrelated, the sign of the correlation differs between F_0 and the cross sections, and F_L and the cross sections. For simplicity, the value meant with “correlation between the sources of uncertainties of the W helicity fractions and the t -channel cross section ρ ” is in fact the correlation between F_0 and the two t -channel cross sections. The correlation between F_L and the two t -channel cross sections has exactly the opposite sign ($-\rho$).

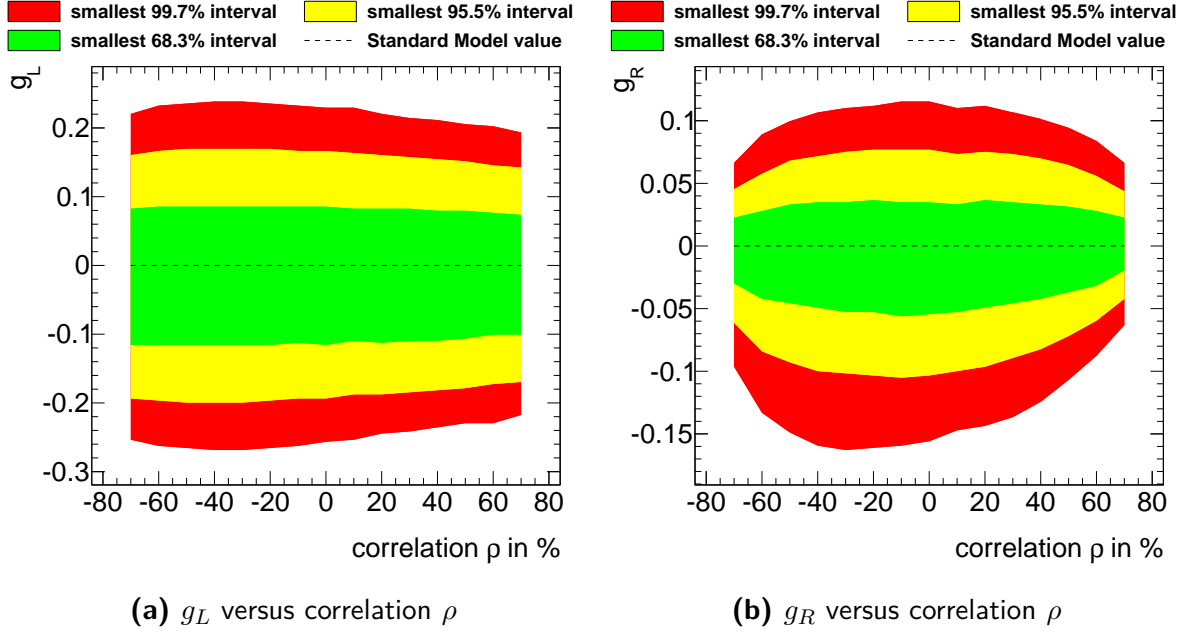
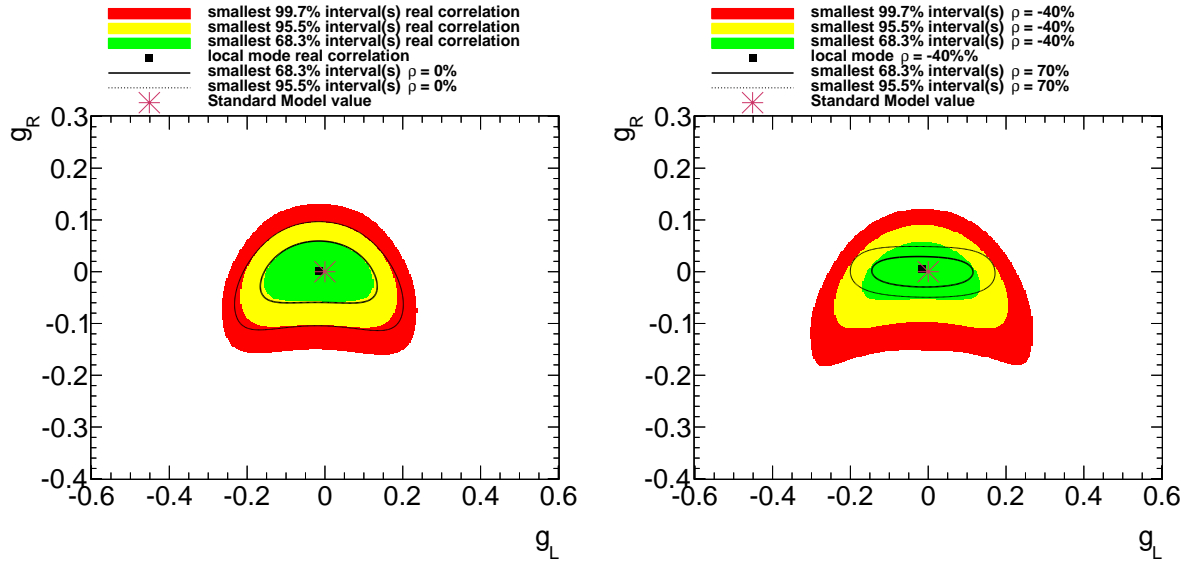


Figure 5.4: Smallest intervals of the anomalous left-handed (5.4a) and right-handed (5.4b) tensor couplings g_L and g_R in dependence on the correlations ρ (see Table 5.3) between the W helicity fraction measurement and t -channel cross section with respect to the systematic uncertainties using an ensemble test. The vector couplings are fixed to $V_L = 1$ and $V_R = 0$, while the coupling not shown is integrated over to be removed from the plot.

two measurements to zero. The average distribution from the ensemble test taking into account the real correlations is slightly narrower than the average distribution from the ensemble setting ρ to zero. This difference is relatively small because of the small correlation between the two measurements of the real correlation matrix of approximately $\rho \sim 20\%$. Figure 5.5b is a more extreme case. Here, the same ensemble test results, but for $\rho = -40\%$ and $\rho = 70\%$ are compared. The two distributions clearly have a different size and shape; the distribution for $\rho = 70\%$ is much narrower than the one for $\rho = -40\%$. This figure shows how much the posterior distributions can deviate due to the correlation between the two measurements with respect to their sources of uncertainties.

These studies show that the knowledge of the correlation between the sources of systematic uncertainties is necessary to set precise bounds on anomalous couplings at the Wtb vertex. This requires an insight into the analyses of the measurements.



(a) Coloured contour plot: correlation matrix (b) Coloured contour plot: $\rho = -40\%$, black lines: $\rho = 0\%$. black lines: $\rho = 70\%$.

Figure 5.5: Comparison between ensemble test results of the g_L - g_R -distributions with $V_L = 1$ and $V_R = 0$ from the combination of the W helicity fractions and the t -channel cross section for different correlations ρ between the measurements. For the correlation between F_L and F_0 , as well as the correlation between σ_t and $\sigma_{\bar{t}}$, the correlation was taken from Table 4.1.

5.5 Effect of merging the top and antitop cross sections into one observable

For the combination presented in this thesis, the t -channel top quark cross section and the t -channel antitop quark cross section are treated as two different observables. The effect of merging the two cross sections into one is studied in this section. An ensemble test is performed with only three observables: F_0 , F_L and the inclusive t -channel production cross section $\sigma_{t+\bar{t}}$ for both top and antitop quark together. For the generation of the pseudo data, the values of the cross sections are generated separately for top and antitop as described in Section 5.1. They are added to determine the inclusive cross section. Its uncertainty is determined by adding the uncertainties in quadrature, which leads to

$$\begin{aligned} \Delta\sigma_{t+\bar{t}} &= \sqrt{\Delta\sigma_t^2 + \Delta\sigma_{\bar{t}}^2 + 2 \cdot \rho(\sigma_t, \sigma_{\bar{t}}) \cdot \Delta\sigma_t \cdot \Delta\sigma_{\bar{t}}} \\ &\approx 8.18 \text{ pb} , \end{aligned} \quad (5.3)$$

taking into account the total correlation between the top and antitop cross section $\rho(\sigma_t, \sigma_{\bar{t}}) = 37.5\%$ from Table 4.1 in Chapter 4. This value is consistent with the uncertainty of the inclusive cross section in Reference [7]. Together with the experimental values of the top

5.5 Effect of merging the top and antitop cross sections into one observable

and antitop cross sections $\sigma_t^{\text{measured}}$ and $\sigma_{\bar{t}}^{\text{measured}}$ [7], the relative uncertainty is

$$\frac{\Delta\sigma_{t+\bar{t}}}{\sigma_{t+\bar{t}}} = \frac{\Delta\sigma_{t+\bar{t}}}{\sigma_t^{\text{measured}} + \sigma_{\bar{t}}^{\text{measured}}} \approx 0.119 , \quad (5.4)$$

which is smaller than both of the separate relative uncertainties, see Table 2.1. The correlations coefficients $\rho(F_0, \sigma_{t+\bar{t}})$ and $\rho(F_L, \sigma_{t+\bar{t}})$ between the W helicity fractions and the inclusive cross section are determined by taking the averages

$$\begin{aligned} \rho(F_0, \sigma_{t+\bar{t}}) &= \frac{\rho(F_0, \sigma_t) + \rho(F_0, \sigma_{\bar{t}})}{2} \quad \text{and} \\ \rho(F_L, \sigma_{t+\bar{t}}) &= \frac{\rho(F_L, \sigma_t) + \rho(F_L, \sigma_{\bar{t}})}{2} . \end{aligned} \quad (5.5)$$

The only difference between this approach and the one using the separate cross sections is that the correlations between the W helicity fractions and the two cross section observables are not treated separately for top and antitop in this approach.

The results of the ensemble test are shown in Figure 5.6. These are fits of all possible combinations, leaving two couplings free and fixing the other two at their Standard Model values. The black lines indicate the smallest intervals from the fits of the ensemble test using the inclusive cross section $\sigma_{t+\bar{t}}$. The coloured contour plots show the results of the ensemble test treating the top and the antitop cross sections as two different observables. It has to be resumed that taking the inclusive cross section as one observable does not result in changes visible in these plots. The reason is that the uncertainties of the W helicity measurement are much smaller than the uncertainties of the cross section measurement. Therefore, the influence of the W helicity measurement on the constraints on the anomalous couplings is much bigger and small changes in the posterior distributions from the cross sections do not have a big influence on the posterior distributions from the combined distributions.

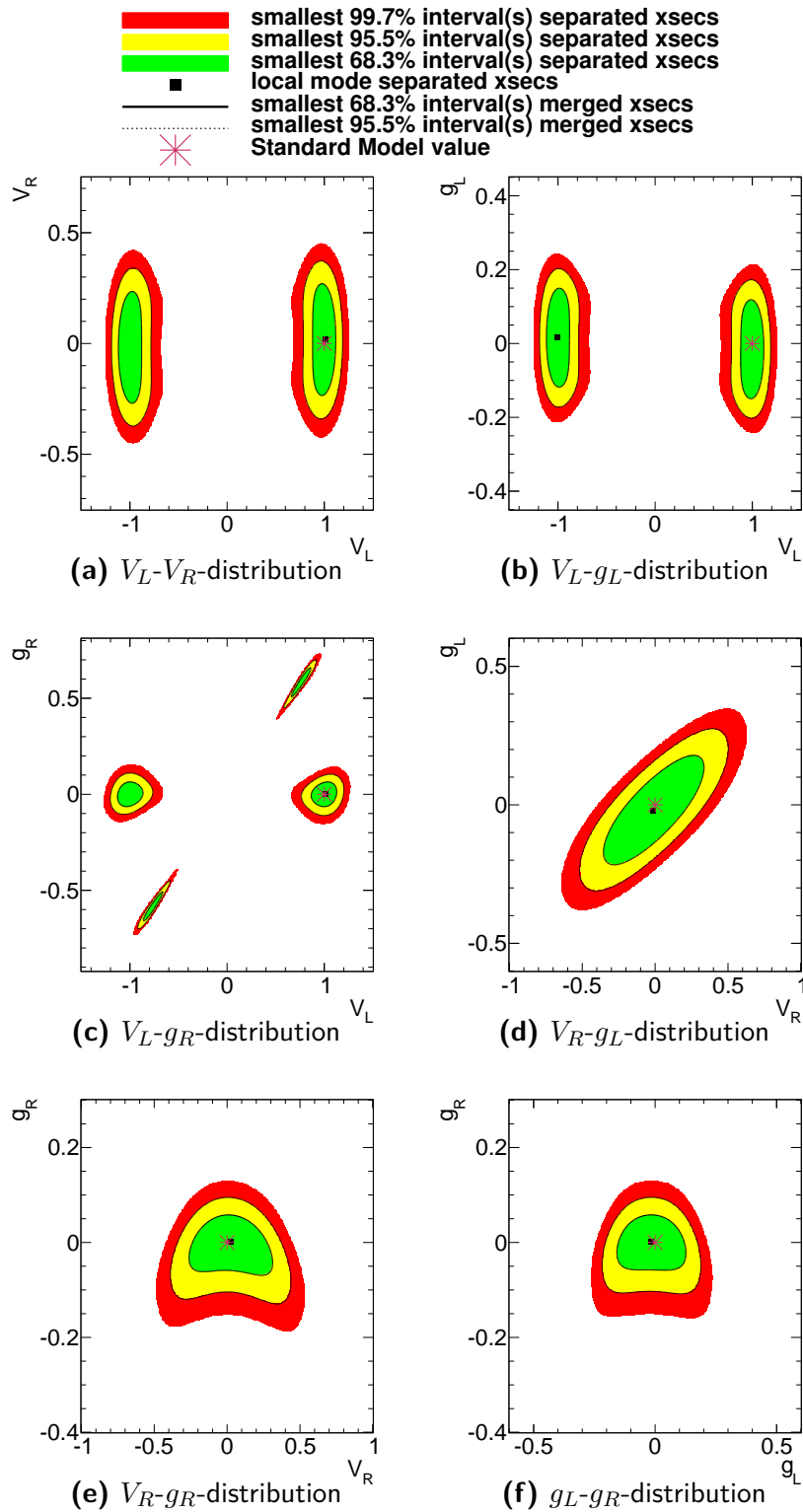


Figure 5.6: Two-dimensional fits for the comparison between the ensemble tests using the top and antitop cross section as two separate observables (coloured contour plot) and using the inclusive cross section $\sigma_{t+\bar{t}}$ (black lines).

5.6 Combination of the top quark measurements with a B -physics measurement

Some B -physics observables can be used to constrain anomalous Wtb couplings if the corresponding processes include Wtb vertices. Their measurements can be combined with the two top quark measurements in order to improve the bounds on anomalous couplings. Possible observables of these kind are $B_{d,s} - \bar{B}_{d,s}$ oscillation observables, the branching ratios of $B_s \rightarrow \mu^+\mu^-$ and $B \rightarrow K^{(*)}\nu\bar{\nu}$, the forward-backward asymmetry in $B \rightarrow K^*l^+l^-$, as well as observables from the $B \rightarrow X_s l^+l^-$ and $B \rightarrow X_s \gamma$ decay modes [11].

As a representative example of these observables, the branching ratio of the radiative penguin decay process $\bar{B} \rightarrow X_s \gamma$ is chosen⁴. This decay involves the process $b \rightarrow s \gamma$. Because flavour changing neutral currents on tree level are forbidden by the Standard Model, the leading order of this decay process is the one-loop level. Besides possible particles predicted by theories beyond the Standard Model that could contribute to this process via the loop, the loops including a W boson and a top quark are the dominant contributions from the Standard Model because of the large CKM matrix element V_{tb} . The corresponding Feynman diagrams are shown in Figure 1.7. It is assumed that no anomalous couplings for the other vertices in these Feynman diagrams exist [11, 88].

The model for describing this branching ratio in terms of anomalous couplings is shown in References⁵ [88] and [124]. Considering only the anomalous couplings V_L , V_R , g_L and g_R from this reference and using a top quark pole mass of 172.5 GeV instead of the 171.4 GeV used in the reference, the model of the branching ratio, requiring minimum photon energies⁶ above and at 1.6 GeV, is [124, 125]

$$\text{Br}(\bar{B} \rightarrow X_s \gamma) = [(3.15 \pm 0.23) - 8.16 \cdot (V_L - V_{tb}^*) + 428.51 \cdot V_R - 839.71 \cdot g_L + 1.93 \cdot g_R] \times 10^{-4}. \quad (5.6)$$

The CKM matrix element V_{tb}^* is set to be 1. For the calculation of the coefficients in Equation (5.6), the \overline{MS} mass of the top quark is used instead of its pole mass. The \overline{MS} mass used in Reference [124] is 161.9 GeV at a renormalisation scale of 160 GeV. To calculate an appropriate \overline{MS} mass for a pole mass of 172.5 GeV, this pole mass is scaled

⁴A neutral \bar{B} meson consisting of a bottom quark b and an anti-up quark decays into a hadron X_s containing a strange quark s and into a photon γ .

⁵Actually, there is a mistake in Equation (14) from Reference [88]. The correct one is Equation (14) in Reference [124].

⁶If not mentioned differently, this requirement is always assumed for this branching ratio from now on.

5 Sensitivity studies using pseudo data

down by a factor of $\frac{161.9 \text{ GeV}}{171.4 \text{ GeV}}$. The bottom quark pole mass is taken from the reference⁷. The value of $(3.15 \pm 0.23) \times 10^{-4}$ within Equation (5.6) is the theoretical Standard Model value and its uncertainty taken from Reference [126]. It has to be remarked that the branching ratio of the process $\bar{B} \rightarrow X_s \gamma$ is sensitive to more possible sources of physics beyond the Standard Model due to the high amount of vertices and virtual particles inside the loop than the two top quark measurements [8, 124].

This B -physics measurement is combined with the two top quark measurements. No correlations are assumed between the B -physics measurement and the top quark measurements because the value of the branching ratio considered for the fits of real data in Chapter 6 is not obtained from ATLAS measurements, but is a combination of measurements performed with the CLEO, Belle and BABAR detectors (see Appendix A.5) not located at the LHC. The correlations between the sources of uncertainties of the two top quark measurements are the same as usual, see Table 4.1.

To obtain the pseudo data, values are generated according to a Gaussian distribution around zero with the total uncertainty as the standard deviation. This total uncertainty is the quadratic sum of the uncertainty of the Standard Model theory prediction (2.3×10^{-5} [126]), the combined statistical and systematic uncertainty (2.4×10^{-5} [10]) and the systematic uncertainty of the average⁸ (0.9×10^{-5} [10]), which yields 3.4×10^{-5} . The randomly generated values are then added to the theoretical Standard Model value. This pseudo data generation is analogous to the generation of the top quark pseudo data described in Section 5.1 but is independent from it because no correlations occur between the B -physics measurement and the top quark measurements.

Table 5.4 shows the smallest 95% C.L. bounds from the one-dimensional fits of the couplings from the ensemble tests of the combination of the two top physics measurements, the B -physics measurement and the three measurements combined, where three couplings are fixed to the Standard Model values at the time. As it is also obvious from Equation 5.6, the B -physics observable is much more sensitive to the right-handed vector coupling V_R and the left-handed tensor coupling g_L than the combination of both top quark measurements. The smallest 95% C.L. bounds on V_R and g_L from the fit of the B -physics measurement are two orders of magnitude narrower than the smallest 95% C.L. bounds from the combination of the top physics measurements only. Furthermore, the sensitivity

⁷This inconsistency has to be accepted due to the large renormalisation scale of 160 GeV and due to the fact that the reference uses a $1S$ mass of 4.68 GeV, which is approximately as large as the pole mass used for the W helicity and cross section measurements, while the pole mass is around 4.16 GeV [125].

⁸For the combination of real measurements in Chapter 6, an average value from Reference [10] is used, see Appendix A.5.

5.6 Combination of the top quark measurements with a B -physics measurement

observables \rightarrow	top and B -physics measurements		only top physics measurements		only B -physics measurements	
	lower bounds	upper bounds	lower bounds	upper bounds	lower bounds	upper bounds
smallest 95% C.L. bounds						
$V_L - 1$	-0.094(1)	0.096(1)	-0.17(1) -2.16(1)	0.17(1) -1.82(1)	-0.12(1)	0.12(1)
V_R	-0.0022(1)	0.0022(1)	-0.27(1)	0.31(1)	-0.0022(1)	0.0022(1)
g_L	-0.0011(1)	0.0011(1)	-0.17(1)	0.14(1)	-0.0011(1)	0.0011(1)
g_R	-0.084(1)	0.079(1)	-0.085(1)	0.081(1)	-0.49(1)	0.50(1)

Table 5.4: The smallest 95% C.L. bounds from the one-dimensional fits of the anomalous couplings from the ensemble tests of the combination of the two top quark measurements, the B -physics measurement and the three measurements combined, where three couplings are fixed to the Standard Model values at the time. The numerical uncertainties shown here are estimated from the range and the binning of the posterior distributions.

to the left-handed vector coupling V_L is higher and V_L does not have a second “island” around $V_L \sim -1$ for the B -physics measurement. Only the smallest 95% C.L. region for the right-handed tensor coupling g_R from the combination of the top quark measurements is approximately five times narrower than the smallest 95% C.L. region from the fit of the B -physics observable. The combination of the two top quark measurements with the B -physics measurement yields even stricter bounds for V_L and the second “island” for $V_L \sim -1$ disappears. Furthermore, the bounds on V_R and g_L are the same⁹ as for the fit of the B -physics measurement alone and the bounds on g_R are the same⁹ as for the fit of the combination of only the two top quark measurements.

Figures 5.7 (for the g_L - g_R -distributions) and A.6 (for all distributions) show the two-dimensional fits only for the B -physics measurement and for the combination of the three measurements, where the other two couplings are fixed to their Standard Model values. All posterior distributions from the fits of the B -physics measurement have in common that they are unconstrained in one direction. The posterior distributions are therefore dependent on the ranges of the fits. This behaviour is due to the fact that the model for the branching ratio $\text{Br}(\bar{B} \rightarrow X_s \gamma)$ is linear in the couplings. Therefore, the branching ratio in dependence on two couplings is a flat, two-dimensional plane intersecting the plane described by the Standard Model value of the branching ratio. The intersection results in a line causing the behaviour seen in the figures. Combining the B -physics measurement with the two top quark measurement constrains these distributions much better due to the fact that the models for both top quark observables are of quadratic order. For the V_L - V_R -distribution (see Subfigure A.6a) and the V_L - g_L -distribution (see

⁹ They are the same within the numerical uncertainties.

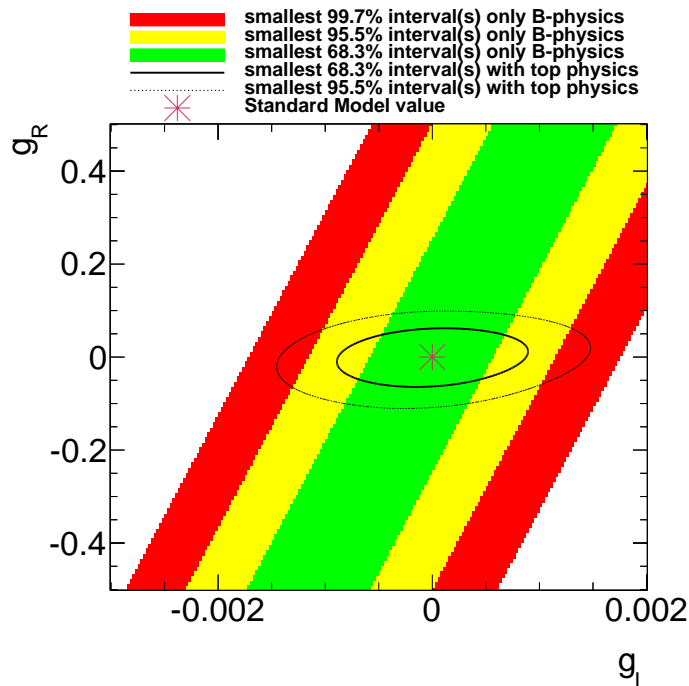


Figure 5.7: Posterior distributions of the two-dimensional fits of g_L and g_R with $V_L = 1$ and $V_R = 0$ for the ensemble test, including the $\text{Br}(\bar{B} \rightarrow X_s \gamma)$ measurement. The plot shows the comparison between the distribution only with the B -physics measurement (coloured contour plot) and with the B -physics measurement and the top physics measurements combined (black lines). The intervals resulting only from the B -physics measurement are dependent on the range of the plots since the distribution exceeds the range.

Subfigure A.6b), there are two smallest 68% C.L. intervals for each fit. One of them is consistent with the Standard Model values of the anomalous couplings, the other “island” is around $(V_L \sim -1, V_R \sim -0.04)$ and $(V_L \sim -1, g_L \sim 0.02)$, respectively. Because of the high sensitivity of the B -physics observable to V_R and g_L , the V_R - g_L -distribution is very narrow. Even though the posterior distribution from the ensemble test of the three combined measurements is constrained in all directions of the anomalous couplings, it does not fit into the plot completely. Therefore, the distribution from the combination of the three measurements looks the same as the distribution from the fit only to the B -physics measurement. In general, the combination of the B -physics measurement with the two top quark measurements constrains the anomalous couplings in all directions. All smallest 68.3% C.L. intervals are consistent with the Standard Model values. All distributions for the combination of the two top quark measurements with the B -physics measurement are narrower than the distribution with the two top quark physics measurements only. From the plots of the two-dimensional fits (Figures 5.7 and A.6), it can be seen that V_L and V_R , V_L and g_R , V_R and g_L , as well as g_L and g_R are correlated, while V_L and g_L , as well as V_R and g_R are anticorrelated. This behaviour is explained by Equation (5.6): For the

5.6 Combination of the top quark measurements with a B -physics measurement

two-dimensional fits, two couplings are varied at the time, while the other ones are fixed to their Standard Model values. For a fixed branching ratio, the couplings entering with a different sign in Equation (5.6) are correlated for these fits and the couplings entering with the same sign are anticorrelated.

In conclusion, the measurement of the branching ratio of the process $\bar{B} \rightarrow X_s \gamma$ sets much narrower one-dimensional bounds on V_R and g_L than the combination of the two top quark measurements. The combination of the three measurements helps to further constrain the one-dimensional limits of V_L and g_R from the B -physics measurement. It also constrains the two-dimensional distributions of the couplings which are all unconstrained in one direction for the fits only with the B -physics observable. On the other hand, the combination with the B -physics measurement further constrains the bounds from the two top quark measurements. As already mentioned, all bounds including the B -physics measurement can also be influenced by other physics beyond the Standard Model contributing to the loop of the process $b \rightarrow s \gamma$. They are therefore more sensitive to other new physics phenomena than the bounds including only the top quark measurements. Therefore, the bounds including the B -physics measurement have to be regarded with care.

This example also shows that it is relatively easy to combine the two top quark measurements with further measurements of observables sensitive to anomalous Wtb couplings, if these measurements and the two top quark measurements are uncorrelated with respect to the sources of systematic uncertainties. It can be considered for future studies to combine further uncorrelated measurements with these measurements.

6 Results

This chapter presents the results of one-, two- and four-dimensional fits to the measured values of the W helicity fractions [6] and the t -channel single top production cross section [7], as well as to the combination of both measurements using the combination method presented in this thesis (see Section 2.3 and Chapter 3). These fits set bounds on the anomalous couplings V_L , V_R , g_L and g_R at the Wtb vertex. The anomalous couplings are assumed to be real. The uncertainties and the total correlation matrix are shown in Chapter 4. In additional fits, the combination of the two top quark measurements with the average value of the branching ratio of the process $\bar{B} \rightarrow X_s \gamma$ is used to set further bounds on the anomalous couplings. In addition to these fits, a comparison between two other recent and similar results of the combination of top quark measurements, and the combinations presented in this thesis is performed. Also, the obtained bounds on anomalous couplings are used to estimate lower limits on new electroweak physics. In this chapter, if not mentioned differently, “the Standard Model values” means in fact “the Standard Model values of the anomalous Wtb couplings”.

6.1 Results of the fits to real data

This section presents the bounds on the anomalous couplings V_L , V_R , g_L and g_R using real data. These bounds are obtained from one-, two- and four-dimensional fits. The four-dimensional fits are conducted via Markov Chain Monte Carlo using the Metropolis algorithm¹, see References [5, 127–129]. The fits of the combination of the W helicity fractions with the t -channel cross section are performed using the experimental values from References [6] and [7], the correlation matrix and the uncertainties from Chapter 4 and the framework presented in Chapter 3. The combination of the two top quark measurements with the average value of the branching ratio of the process $\bar{B} \rightarrow X_s \gamma$

¹The reason why there is no ensemble test for the four-dimensional fit is that this fit takes much more CPU time because of the Metropolis algorithm. Also, there are no four-dimensional fits including the B -physics measurement due to numerical issues arising in these fits.

observables \rightarrow	$F_0, F_L, \sigma_t, \sigma_{\bar{t}}$		only F_0, F_L		only $\sigma_t, \sigma_{\bar{t}}$	
smallest 95% C.L. bounds	lower bounds	upper bounds	lower bounds	upper bounds	lower bounds	upper bounds
$V_L - 1$	-0.05(1) -2.17(1)	0.17(1) -1.94(1)	-	-	-0.09(1) -2.14(1)	0.15(1) -1.90(1)
V_R	-0.30(1)	0.31(1)	-0.29(1)	0.29(1)	-0.49(1)	0.49(1)
g_L	-0.19(1)	0.16(1)	-0.19(1)	0.16(1)	-0.37(1)	0.38(1)
g_R	-0.094(1)	0.029(1)	-0.08(1) 0.75(1)	0.04(1) 0.80(1)	-0.30(1)	0.46(1)

Table 6.1: The smallest 95% C.L. bounds on anomalous Wtb couplings from the one-dimensional fits of the W helicity measurement, the t -channel cross section measurement and both measurements combined, including their numerical uncertainties and using measured data from Reference [6] and [7]. Three couplings are fixed to the Standard Model values at a time. The numerical uncertainties shown here are estimated from the range and the binning of the posterior distributions.

taken from Reference [10] is also presented in this section.

6.1.1 Combination of the W helicity measurement with the t -channel cross section measurement

This subsection presents the results of the combination of the W helicity measurement with the t -channel single top production cross section measurement using the data from References [6] and [7]. The one-dimensional fit results, fixing the other three couplings at their Standard Model values, are presented in Table 6.1. All smallest 95% C.L. intervals are consistent with the Standard Model values. For the fits of the W helicity measurement, V_L is unconstrained and the right-handed tensor coupling has a second interval at $g_R \sim 0.8$. For the fits of the t -channel cross section measurement, there is a second 95% C.L. interval for V_L around $V_L \sim -1$. The combination of the two top quark measurements constrains V_L , allowing a second region around $V_L \sim -1$. The second interval around $g_R \sim 0.8$ allowed by the W helicity measurement does not exist. Apart from this, the bounds on V_R , g_L and g_R compared to the fit to the W helicity measurement only, as well as on V_L compared to the fit to the t -channel measurement do not get narrower within the numerical uncertainties. All of these bounds are consistent with the Standard Model values. The smallest 95% C.L. bounds overlap with the ones from the expectation shown in Table 5.1.

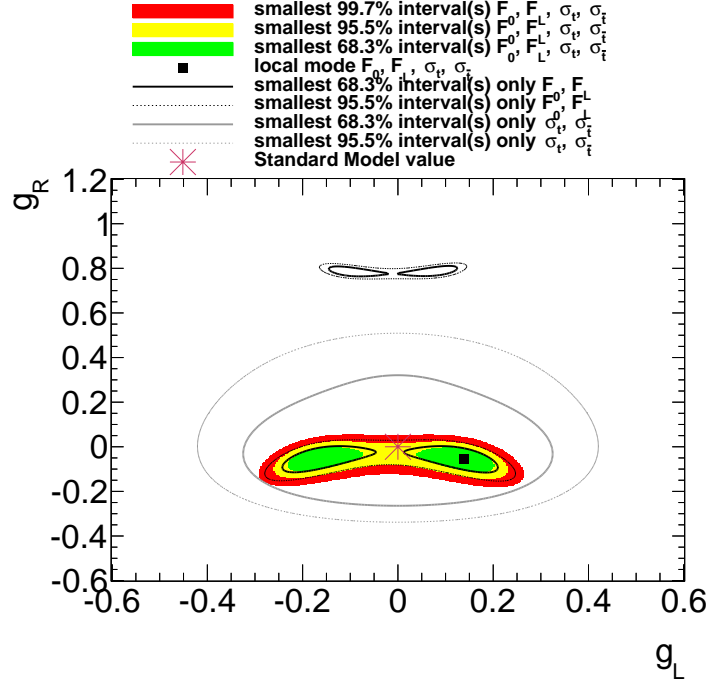


Figure 6.1: Comparison between the results of the posterior probabilities of the g_L - g_R -distributions with $V_L = 1$ and $V_R = 0$ from the separate fits of the W helicity fractions, the t -channel cross sections and from the combination of both measurements, using real data.

The two-dimensional fit results to real data are shown in Figure 6.1 and Figure 6.2, where the other two couplings are fixed to their Standard Model values. Their properties are the following:

- V_R - g_R - and g_L - g_R -distributions (Subfigures 6.2e and 6.2f, as well as Figure 6.1): The distributions from the fits of the W helicity measurement have a smallest 95.5% C.L. interval around $g_R \sim 0.8$ each, while the other smallest 95.5% C.L. intervals are consistent with the Standard Model values. The smallest 68.3% intervals of both distributions are not consistent with these Standard Model values. The smallest 68.3% intervals from the fits of the t -channel cross section measurement are much wider than the ones for the fit of the W helicity measurement for both fits. They are consistent with the Standard Model values and do not have a second region around $g_R \sim 0.8$. The combination of the two top quark measurements yields no second region around $g_R \sim 0.8$ and it causes the general areas to shrink with respect to the separate fits of the observables. The resulting smallest 95.5% C.L. intervals are consistent with the Standard Model values, but the smallest 68.3% C.L. intervals are not.

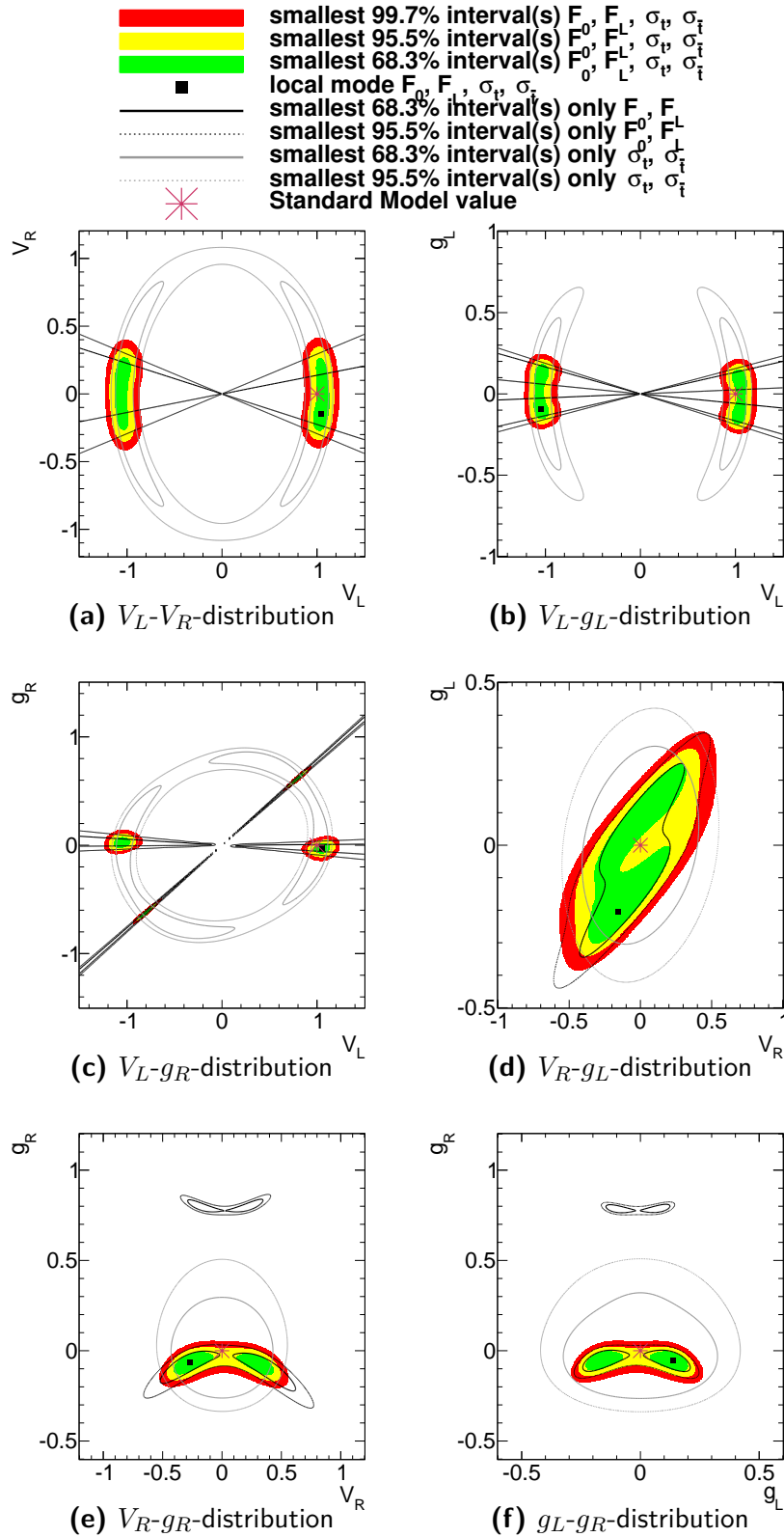


Figure 6.2: Comparison between the results of the two-dimensional fits of the measurements of the W helicity fractions, the t -channel cross sections and the combination of both measurements, using real data.

- V_L - V_{R^-} , V_L - g_{L^-} and V_L - g_{R^-} -distributions (Subfigures 6.2a, 6.2b and 6.2c): The posterior distributions from the fits of the W helicity measurement are unconstrained in the direction of V_L , so the distributions are dependent on the ranges of the fits. The range of these fits for V_L is chosen to be $[-1.5, 1.5]$. The smallest 95.5% C.L. intervals are all consistent with the Standard Model values for the given range of V_L , but the smallest 68.3% C.L. intervals of the V_L - g_{L^-} -distribution are not. For the fits of the t -channel cross section measurement only, there are two smallest 68.3% C.L. intervals each: one around the Standard Model values and one consistent with $V_L \sim -1$ and $V_{R^-}/g_{L^-}/g_{R^-} \sim 0$. For the V_L - g_{R^-} -distribution, both of these areas are slightly tilted, covering a relatively large area of the parameter space. The combination with the W helicity measurement causes these two intervals to shrink and for the V_L - g_{R^-} -distribution, the combination of both measurements yields four “islands”: one consistent with the Standard Model values, one consistent with $V_L \sim -1$ and $g_{R^-} \sim 0$, one consistent with $V_L \sim -0.8$ and $g_{R^-} \sim -0.6$ and one consistent with $V_L \sim 0.8$ and $g_{R^-} \sim 0.6$. The resulting smallest 95.5% C.L. intervals are all consistent with the Standard Model values, but the smallest 68.3% C.L. intervals of the V_L - g_{L^-} -distribution are not.
- V_{R^-} - g_{L^-} -distribution (Subfigure 6.2d): For the two fits of the separate measurements, the smallest 68.3% C.L. intervals are consistent with the Standard Model values and for their combination, the smallest 68.3% C.L. interval is not consistent with the Standard Model values, but the smallest 95.5% C.L. interval is.

The smallest 68.3% C.L. intervals from the two-dimensional fits of the combination of the two measurements, using real data, overlap with the ones of the expected distributions, determined by the ensemble tests presented in Chapter 5, see Figure 6.3 and Figure A.7. Even though some of the smallest 68.3% C.L. intervals of these fits are not consistent with the Standard Model values, it is possible that the deviation of the distributions from the expectation is due to the uncertainties of the measurement, see Section 5.3.

Figure 6.4 shows the plots of the four-dimensional fit for the combined measurements and for the cross section measurement only. The couplings not displayed in the different subfigures are integrated over. The distributions for the W helicity fractions are not shown here because they do not depend on V_L , so all plots would depend on the defined range of V_L . Taking into account only the cross section measurement, the smallest 68.3% C.L. intervals of the V_{R^-} - g_{R^-} - and g_{L^-} - g_{R^-} -distributions are not consistent with the Standard Model values, but their smallest 95.5% C.L. intervals are. For the combination of the two top quark measurements, all smallest 68.3% C.L. intervals are consistent with the

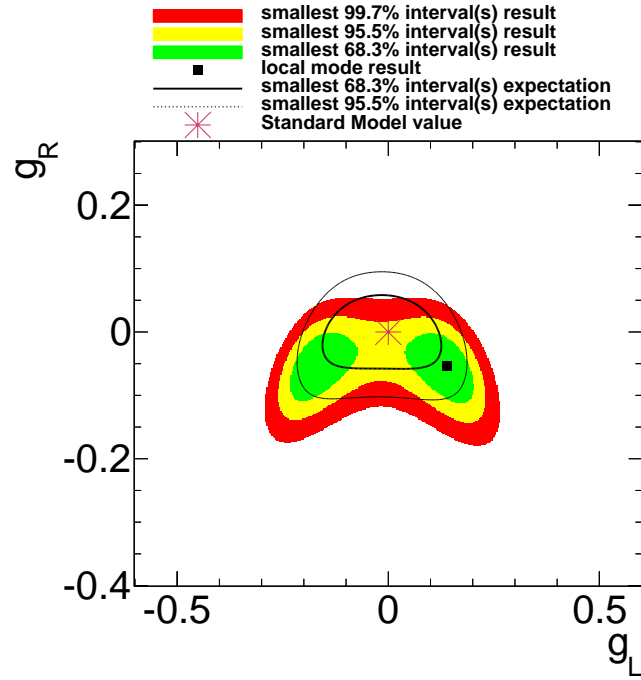


Figure 6.3: The posterior distribution from the two-dimensional fit of the two tensor couplings for the real measurements (coloured contour plot, vector couplings fixed to Standard Model value) in comparison to the posterior distribution of the ensemble test (black lines) presented in Chapter 5 as the expected outcome of the fit assuming the anomalous couplings acquiring their Standard Model values.

Standard Model values, except for the $V_R g_L$ -distribution. Nevertheless, the smallest 95.5% C.L. interval of the $V_R g_L$ -distribution is consistent with the Standard Model values. The combination with the W helicity measurement causes the bounds on the anomalous couplings to become narrower.

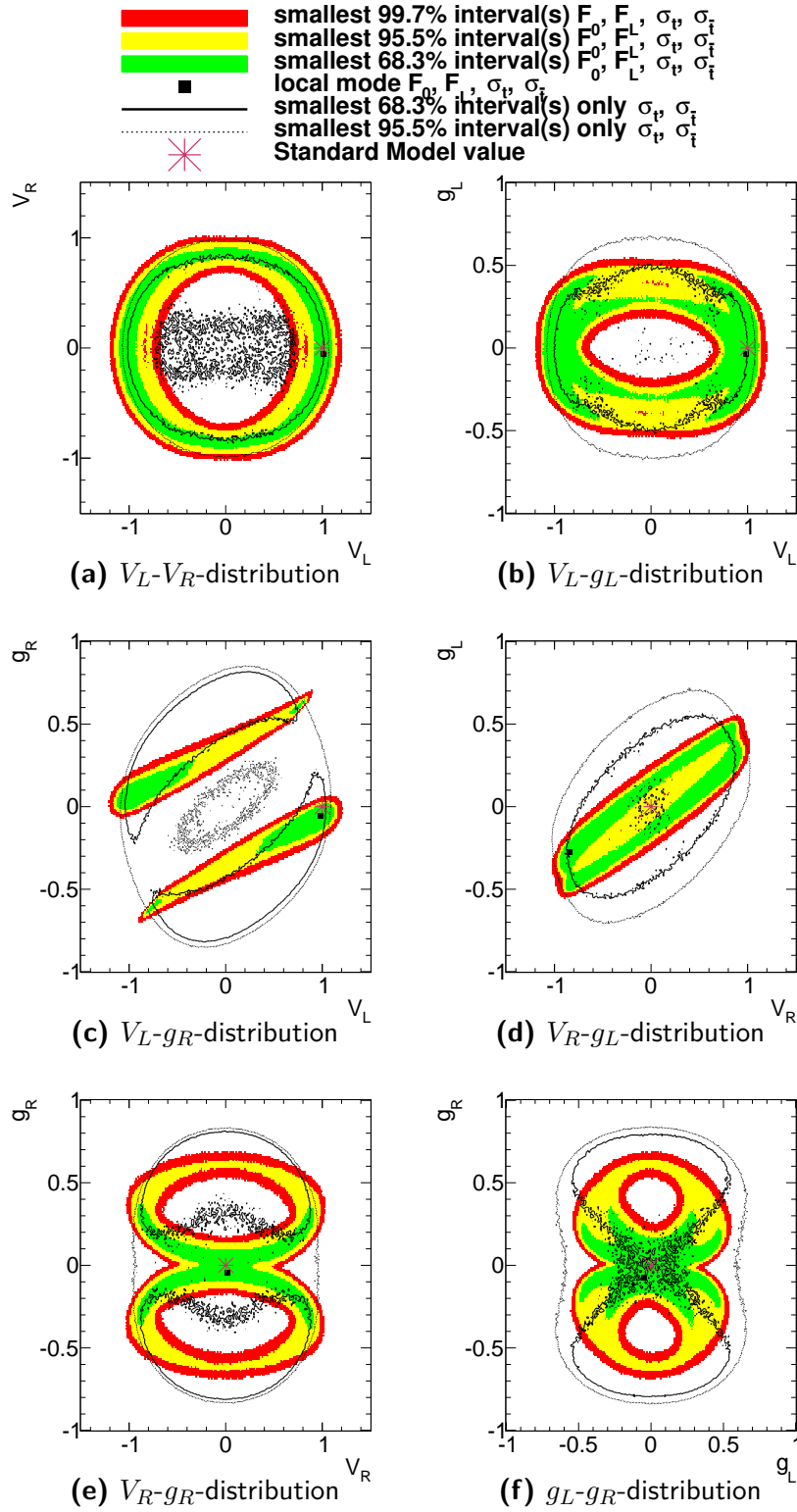


Figure 6.4: Plots of the four-dimensional fit of the t -channel cross section measurement only (black lines) and the combination of both top quark measurements (coloured contour plots). The couplings not displayed in the different plots are integrated over.

6.1.2 Combination of the two top quark measurements with the B -physics measurement

In this subsection, the measurement of the branching ratio of the process $\bar{B} \rightarrow X_s \gamma$ is combined with the two top quark measurements (W helicity and t -channel cross section measurement) and fits are conducted to set further limits on anomalous Wtb couplings. The combination and the model of the branching ratio in dependence on the anomalous couplings are shown in Section 5.6. The value from the B -physics measurement is a combined value² taken from Reference [10]. The combination of the measurements of the branching ratio $\text{Br}(\bar{B} \rightarrow X_s \gamma)$ to obtain the value used here is described in Appendix A.5. The value³ used for this combination is

$$\begin{aligned} \text{Br}(\bar{B} \rightarrow X_s \gamma) &= (3.55 \pm \underbrace{0.24}_{\text{stat\&sys}} \pm \underbrace{0.09}_{\text{comb}} \pm \underbrace{0.23}_{\text{pred}}) \times 10^{-4} \\ &= (3.55 \pm 0.34) \times 10^{-4} , \end{aligned} \tag{6.1}$$

with the combined statistical and systematic uncertainty (“stat&sys”), the systematic uncertainty of the average (“comb”, both from Reference [10]) and the uncertainty of the Standard Model prediction (“pred”) from Reference [126], which is added to describe the uncertainty of the reference value.

Table 6.2 shows the results of three one-dimensional fits: the fits of the combination of only the two top quark measurements, of the B -physics measurement only and of the three measurements combined. All smallest 95% C.L. intervals are consistent with the Standard Model values and overlap with the smallest 95% C.L. intervals from the expectation, see Table 5.4. The intervals for the combination of the top quark measurements only are the same as shown in Table 6.1. The intervals for the fits of the B -physics measurement are consistent with the results from Reference [124], also shown in Table 6.3 within the numerical uncertainties. The comparison is possible because the fit conducted in this thesis uses a constant prior. Possible deviations could stem from the fact that the top quark mass used in the reference is different from the one used here and that the combined value for the branching ratio is from a less recent combination [130] with larger uncertainties. As already mentioned in Section 5.6, the smallest 95% C.L. bounds from

²Taking a combined value for the B -physics measurement for this combination does not cause any problems because all sources of uncertainties are assumed to be uncorrelated between the top physics and B -physics measurements, as already explained in Section 5.6. The combined value can therefore be treated as the result of a single measurements with the advantage of smaller uncertainties.

³The influence of CP violation is taken to be small to be able to assume $\text{Br}(\bar{B} \rightarrow X_s \gamma) = \text{Br}(B \rightarrow X_s \gamma)$, see Appendix A.5.

observables \rightarrow	top and B -physics measurements		only top physics measurements		only B -physics measurements	
	lower bounds	upper bounds	lower bounds	upper bounds	lower bounds	upper bounds
$V_L - 1$	-0.081(1)	0.058(1)	-0.05(1) -2.17(1)	0.17(1) -1.94(1)	-0.13(1)	0.04(1)
V_R	-0.0006(1)	0.0025(1)	-0.30(1)	0.31(1)	-0.0006(1)	0.0025(1)
g_L	-0.0013(1)	0.0003(1)	-0.19(1)	0.16(1)	-0.0013(1)	0.0003(1)
g_R	-0.086(1)	0.035(1)	-0.094(1)	0.029(1)	-0.14(1)	0.56(1)

Table 6.2: The smallest 95% C.L. bounds from the one-dimensional fits of the anomalous couplings from the combination of the two top physics measurements, the B -physics measurement and the three measurements combined, including their numerical uncertainties and using data from the References [6, 7, 10]. The three other couplings are fixed to the Standard Model values at a time. The numerical uncertainties shown here are estimated from the range and the binning of the posterior distributions.

95% C.L. bounds	$V_L - 1$	V_R	g_L	g_R
upper bound	0.03	0.0025	0.0004	0.57
lower bound	-0.13	-0.0007	-0.0013	-0.15

Table 6.3: 95% C.L. bounds on anomalous couplings using the branching ratio of the decay $\bar{B} \rightarrow X_s \gamma$, taken from Reference [124].

the B -physics measurement on the right-handed vector coupling V_R and the left-handed tensor coupling g_L are two orders of magnitude narrower than for the combination of the two top quark measurements. Also, the bounds on the left-handed vector coupling V_L are narrower and do not allow a second “island” around $V_L \sim -1$ for the fit of the B -physics measurement. Only the smallest 95% C.L. bounds on the right-handed tensor coupling g_R are narrower for the combination of the top physics measurement. For the combination of the three measurements, the smallest 95% C.L. bounds on V_R and g_L are the same⁴ as those obtained from the fit of the B -physics measurement only. The smallest 95% C.L. bounds on g_R are the same⁴ as from the combination of the two top quark measurements only. Furthermore, the second “island” around $V_L \sim -1$ disappears and the smallest 95% C.L. bounds on V_L are even narrower than those from the fit of the B -physics measurement.

Figures 6.5 and A.8 show the posterior distributions from the two-dimensional fits of the B -physics measurement only and of the combination of the B -physics measurement with the two top quark measurements. As already discussed in Section 5.6, all distributions of the B -physics measurement are unconstrained in one direction because the model of

⁴ They are the same within the numerical uncertainties.

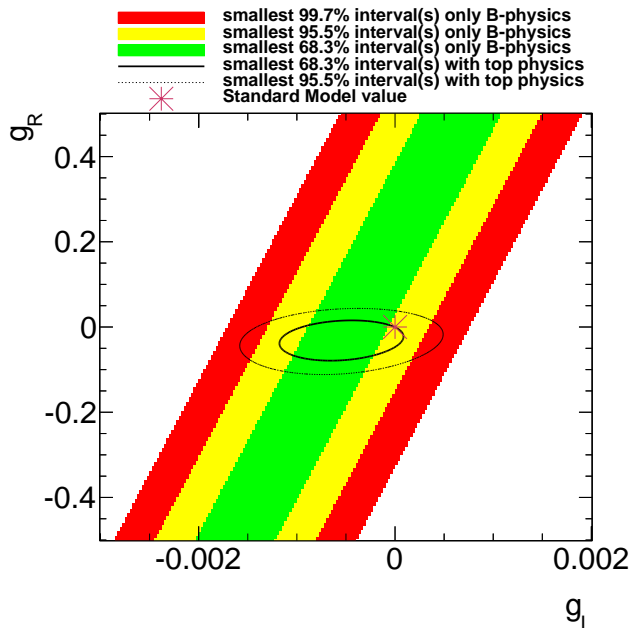


Figure 6.5: Posterior distributions of the two-dimensional fits of g_L and g_R with $V_L = 1$ and $V_R = 0$ for the data from References [6, 7, 10], including the $\text{Br}(\bar{B} \rightarrow X_s \gamma)$ measurement. The plot shows the comparison between the distribution only with the B -physics measurement (coloured contour plot) and with the B -physics measurement and the top physics measurements combined (black line as smallest 68.3% credibility level interval). The intervals resulting only from the B -physics measurement are dependent on the range of the plots since the distribution exceeds the range.

the branching fraction is linear in the anomalous couplings. For the combination of the B -physics measurement with the top quark measurements, all distributions are fully constrained. The smallest 95.5% C.L. intervals of all fits are consistent with the Standard Model values of the anomalous couplings. The V_L - V_R - and the V_L - g_L -distributions allow a second island each around $V_L \sim -1$ and $V_R \sim -0.04/g_L \sim 0.02$. The posterior distribution for the fit of V_R and g_L together could not be fully displayed in the plot because the distribution is too narrow. Figure A.9 shows the comparison between the fits of the data from the real measurements with the expectation obtained from the ensemble tests, which shows that the smallest 68.3% C.L. intervals for “result” and “expectation” overlap each other.

All distributions for the two-dimensional fits of the combination of the two top quark measurements with the B -physics measurement are narrower than these distributions for the two top quark physics measurements only. As already mentioned in Section 5.6, all bounds including the B -physics measurement are sensitive to more possible sources of physics beyond the Standard Model than the top quark measurements, so these bounds have to be regarded with care.

6.2 Comparison with similar results of the combination of top quark measurements setting bounds on anomalous Wtb couplings

There are several publications which also set bounds on anomalous Wtb couplings via the combination of top quark measurements. In this section, the results from this thesis will be compared to the results of two recent publications.

The combination presented in Reference [131] uses six top quark measurements to constrain the four anomalous couplings V_L , V_R , g_L and g_R , as well as an additional coefficient C_{4f} for four-fermion couplings. In addition, a study on anomalous $gt\bar{t}$ couplings⁵ is conducted in this reference. The six measurements used for the combination are a W helicity measurement conducted by the CMS collaboration at $\sqrt{s} = 8$ TeV [132], one t -channel single top cross section measurement for $\sqrt{s} = 7$ TeV and $\sqrt{s} = 8$ TeV each (both conducted by the CMS collaboration) [133, 134], one combination of s -channel single top cross section measurements at $\sqrt{s} = 1.98$ TeV conducted by the CDF and DØ collaborations [77] and one measurement of the W -associated single top cross section at $\sqrt{s} = 7$ TeV and $\sqrt{s} = 8$ TeV each (both conducted by the CMS collaborations) [135, 136]. A value of an anomalous coupling $c_i = V_L - 1, V_R, g_L, g_R, C_{4f}$ is considered to be excluded at 95% confidence level by the measurement of the observable x , if

$$\begin{aligned} x_{\text{MG5}}(c_i) - x_{\text{MG5}}(0) &> x_{\text{exp}} - x_{\text{th}} + 2\sqrt{(\Delta x_{\text{exp}})^2 + (\Delta x_{\text{th}})^2} && \text{or} \\ x_{\text{MG5}}(c_i) - x_{\text{MG5}}(0) &< x_{\text{exp}} - x_{\text{th}} - 2\sqrt{(\Delta x_{\text{exp}})^2 + (\Delta x_{\text{th}})^2}, \end{aligned} \quad (6.2)$$

where $x_{\text{MG5}}(c_i)$ is the observable in dependence on the coupling c_i modelled using FEYN-RULES [137] and MADGRAPH 5 [138], x_{exp} is central value of the experimental result and x_{th} theoretical Standard Model value with the respective uncertainties Δx_{exp} and Δx_{th} . For the W helicity measurements, the method described here is modified to take into account the correlation between F_0 and F_L . Correlations between the measurements are not taken into account.

In Reference [139], two CMS measurements are combined to determine bounds on the four anomalous couplings V_L , V_R , g_L and g_R using the TOPFIT package [140]. These two measurements are a W helicity measurement [132] and a t -channel single top cross section measurement [134], both using data taken at a centre-of-mass energy of 8 TeV. They are also used in the combination presented in Reference [131]. Correlations between these

⁵This describes the coupling of the gluon to two top quarks.

6 Results

observables \rightarrow	this combination top and B -physics		this combination only top physics		Reference [131]		Reference [139]	
	lower bounds	upper bounds	lower bounds	upper bounds	lower bounds	upper bounds	lower bounds	upper bounds
$V_L - 1$	-0.081(1)	0.058(1)	-0.05(1) -2.17(1)	0.17(1) -1.94(1)	-0.098	0.081	-	-
V_R	-0.0006(1)	0.0025(1)	-0.30(1)	0.31(1)	-0.112	0.162	-0.13	0.18
g_L	-0.0013(1)	0.0003(1)	-0.19(1)	0.16(1)	-0.081	0.049	-0.09	0.06
g_R	-0.086(1)	0.035(1)	-0.094(1)	0.029(1)	-0.142	0.023	-0.15	0.01

Table 6.4: The smallest 95% C.L. bounds on anomalous Wtb couplings from the one-dimensional fits of the combination presented in this thesis (with and without the B -physics measurement), as well as from the combinations presented in Reference [131] and in Reference [139]. Three couplings at the time are fixed to the Standard Model values.

measurements are not taken into account. In addition, imaginary parts of the couplings are studied, as well as the influence of the combination of these measurements with a measurement of the W -associated single top cross section [136] and TEVATRON results for the W helicity fractions [141] and the single top quark cross section (s - and t -channel combined) [142]. For the comparison, the combination of the two CMS measurements at $\sqrt{s} = 8$ TeV, assuming the anomalous couplings to be real, is chosen.

The results of the one-dimensional fits from these two combinations in comparison with the combination of the two top quark measurements presented in this thesis (with and without the B -physics measurement), are listed in Table 6.4. If not specified differently, “the combination presented in this thesis” means actually “the combination of the two top quark measurements, without the B -physics measurement, presented in this thesis”. The results for the two-dimensional fits of the g_L - g_R -distributions⁶ are listed in Figure A.10 for Reference [131] and in Figure A.11 for Reference [139]. For the two-dimensional fits from the two references, the top quark measurements are not combined. The overlap of the distributions of the separate fits mark the allowed regions from all measurements. To be able to compare the results, this overlap is interpreted as the approximated distribution from the fit for the combined measurements. Although the bounds from the two combinations are based on frequentist reasoning, they can be compared with the combination from this thesis, which is based on Bayesian reasoning, because the prior of the posterior distribution is constant.

⁶Both references also include two-dimensional fits of the V_L - V_R -distributions. They are not used for the comparison because the model of the W helicity fractions is not sensitive to V_L and therefore, the resulting distributions are sensitive to the range of the fits.

6.2 Comparison with similar results setting bounds on anomalous Wtb couplings

- Comparison with the combination presented in Reference [131]:

The one-dimensional 95% C.L. bounds on V_L , V_R and g_L from this reference are narrower than the bounds from the combination presented in this thesis, while the right-handed tensor coupling g_R is better constrained by the combination presented in this thesis. In the two-dimensional fits of the g_L - g_R -distributions, the overlap of the 95% C.L. regions of this reference constrains g_R approximately⁷ as good as the combination presented in this thesis. The bounds on g_L are narrower for the overlapping distributions presented in Reference [131] than for the combination presented in this thesis.

- Comparison with the combination presented in Reference [139]:

The one-dimensional 95% C.L. bounds on the anomalous couplings V_R and g_L from this reference are narrower than the bounds from the combination presented in this thesis. The bounds on g_R from this reference are wider than the bounds from the combination presented in this thesis. Also, there are no one-dimensional bounds listed for V_L in this reference. The one-dimensional 95% C.L. bounds on V_R and g_L from this reference are wider than the ones from Reference [131] because this combination only uses two measurements instead of six. The one-dimensional 95% C.L. bounds on g_R are slightly narrower than the ones from Reference [131], which could be due to the rounding or due to the different models and combination techniques used in Reference [131]. Regarding the two-dimensional 95% C.L. fits, the limits on g_R from the overlapping regions presented in this reference are approximately of the same size as for the overlapping regions presented in Reference [131] and the combination presented in this thesis. The bounds on g_L are narrower for the overlapping fits presented in this reference than for the combination presented in this thesis, and they are approximately of the same size as the ones from the combination presented in Reference [131].

The reason the combination presented in Reference [131] yields the narrowest bounds on the anomalous couplings V_L , V_R and g_L compared to the other two combinations is assumed to be the fact that six measurements are combined instead of two. Although the uncertainties of the CMS measurements⁸ from References [132] and [134], used in the combination from both references, are approximately of the same size as the ones of the ATLAS measurements used in this thesis, the bounds from the combination of these

⁷This is a rough estimation by eye. When estimating this range for the x - y -distribution, the maximal (minimal) values of x are the 95% bounds with the biggest deviations from the Standard Model value of the coupling x in the positive (negative) direction for all y .

⁸ $F_0 = 0.659 \pm 0.027$, $F_L = 0.350 \pm 0.026$, $\sigma_{t+\bar{t}} = 83.6 \pm 7.7$ pb

6 Results

two CMS measurements presented in Reference [139] are narrower for V_R and g_L . This can be due to the different model parameters of the t -channel cross section for $\sqrt{s} = 8$ TeV compared to the parameters used in this thesis for $\sqrt{s} = 7$ TeV. A more direct comparison can be made for the W helicity measurements, because the same model with the same particle masses is used for both combinations and this model is independent from the centre-of-mass-energy. The model in dependence on the anomalous couplings, fixing three couplings at the time, is shown in Figure 3.1. For constant ΔF_0 and ΔF_L , higher F_0 and F_L result in narrower bounds on g_L because of the quadratic behaviour in g_L peaking at the Standard Model values of the W helicity fractions. The same holds true for F_L in dependence on V_R (but not for F_0). On the other hand, the bounds on g_R from the combination presented in this thesis are narrower than the bounds from the CMS measurement, because the uncertainty on F_L from the ATLAS measurement is smaller than for the CMS measurement and g_R does not have the described property of V_R and g_L peaking at the Standard Model values. For a better comparison, sensitivity studies of the combinations presented in References [131] and [139], assuming the Standard Model values to be the real measured values, analogous to Chapter 5, would be necessary.

Besides the comparison of the three combinations only taking into account top quark measurements, the combination presented in this thesis including the two top quark measurements and the B -physics measurement yields the best bounds on the anomalous couplings for all of the combinations presented in this section, see Table 6.4. As it is expected, especially the bounds on V_R and g_L are two orders of magnitude narrower than these bounds from the three presented combinations taking into account only top quark measurements.

As already demonstrated in Section 5.4, it is very important to treat the correlations between the combined measurements with respect to their sources of uncertainties in the right way in order to obtain precise bounds on anomalous couplings from the fits. Even though the combinations from References [131] and [139] yield narrower bounds on V_R and g_L , they assume these correlations to be zero. Considering these correlations would result in more precise and therefore better bounds on the anomalous couplings for both of these combinations. However, it is necessary to have a further insight into the measurement's analysis for the correct determination of these correlations, which is only possible for members of the experiment's collaborations.

These combinations also do not take into account the uncertainties due to the Standard Model prediction of the observables. Therefore, the uncertainty of the actual position of $(V_L, V_R, g_L, g_R) = (1, 0, 0, 0)$ is not considered in the distributions emerging from the

fits of these combinations. Including these uncertainties would loosen the bounds on the anomalous couplings.

Even though the bounds on V_L , V_R and g_L from the combination presented in this thesis are not the narrowest ones of these three combinations, they can be considered to be the most reliable ones because of the consideration of the correlations between the two measurements with respect to the sources of uncertainties and the inclusion of the uncertainties of the Standard Model values of the observables. In addition, the bounds on the right-handed tensor coupling g_R are the best ones of these three combinations. In contrast to the other two combinations, the studies presented in this thesis also include two- and four-dimensional fits of the combination, with the possibility to also conduct three-dimensional fits.

As it is pointed out in Reference [139], the combination of the LHC measurements with TEVATRON measurements can improve the LHC limits by roughly 20%. This combination can also be considered to improve the limits presented in this thesis. Nevertheless, there are some sources of systematic uncertainties for which the correlations between the ATLAS measurements and the measurements of DØ and CDF have to be studied. Possible correlations can arise e.g. for Monte Carlo data, for Monte Carlo based uncertainty components of the jet energy scale or for the treatment of fragmentation processes. This requires some insight into these analyses and it has to be checked if the needed data is available in order to conduct this combination. A study of correlations between the sources of systematic uncertainties of ATLAS, CMS, CDF and DØ measurements is performed for instance in Reference [60] for a top quark mass combination.

6.3 Energy scale of the effective operators

As described in Section 1.3, the higher dimensional operators in the effective field theory of anomalous Wtb couplings are suppressed by orders of the mass scale where new electroweak physics is expected. From the one-dimensional limits on the anomalous couplings, lower limits of the energy scale for the effective operators from Equations (1.29) to (1.33) can be estimated the way it was done in Reference [131]. Above these lower limits, there is still room for new physics. With the rough estimation of $C_{\phi q}^{(3)*} \approx 1$ and $\text{Re} C_{qW} \approx 0$ using V_L , $C_{\phi\phi}^* \approx 1$ using V_R , $C_{dW}^* \approx 1$ using g_L and $C_{uW} \approx 1$ using g_R , one

6 Results

$$\begin{array}{ll}
|V_L - 1| \leq 0.17(1), & \Lambda \gtrsim 600 \text{ GeV} & |V_L - 1| \leq 0.081(1), & \Lambda \gtrsim 900 \text{ GeV} \\
|V_R| \leq 0.31(1), & \Lambda \gtrsim 300 \text{ GeV} & |V_R| \leq 0.0025(1), & \Lambda \gtrsim 3500 \text{ GeV} \\
|g_L| \leq 0.19(1), & \Lambda \gtrsim 700 \text{ GeV} & |g_L| \leq 0.0013(1), & \Lambda \gtrsim 8200 \text{ GeV} \\
|g_R| \leq 0.094(1), & \Lambda \gtrsim 1000 \text{ GeV} & |g_R| \leq 0.086(1), & \Lambda \gtrsim 1000 \text{ GeV}
\end{array}$$

(a) Constraints only from the two top quark measurements. **(b)** Constraints from the two top quark measurements and the B physics measurement.

Table 6.5: Constraints on the energy scale of the effective operators from the four anomalous couplings at 95% C.L..

can write the Equations from (1.36) as

$$\begin{aligned}
\Lambda &\approx \frac{246 \text{ GeV}}{\sqrt{|V_L - 1|}}, & \Lambda &\approx \frac{293 \text{ GeV}}{\sqrt{|g_L|}}, \\
\Lambda &\approx \frac{174 \text{ GeV}}{\sqrt{|V_R|}}, & \Lambda &\approx \frac{293 \text{ GeV}}{\sqrt{|g_R|}},
\end{aligned} \tag{6.3}$$

with the Higgs vacuum expectation value $v \approx 246 \text{ GeV}$ [12]. For this estimation, the limits⁹ from the one-dimensional fits of the combination of the two top quark measurements and of the combination of the two top quark measurements with the B -physics measurement shown in Tables 6.1 and 6.2 are used.

The results from this estimation of the lower 95% C.L. bounds can be seen in Table 6.5. Table 6.5a shows the constraints from the combination of the W helicity fraction measurement with the t -channel production cross section measurement. Table 6.5b shows the constraints from the combination of these two top quark measurements with the measurement of $\text{Br}(\bar{B} \rightarrow X_s \gamma)$. The lower 95% C.L. limits for the energy scale Λ , taking into account only the top quark measurements, vary from 300 GeV to 1000 GeV. These lower limits are in principle possible to test via direct searches at the LHC, e.g. in searches for new particles. Including the measurement of $\text{Br}(\bar{B} \rightarrow X_s \gamma)$ improves these limits by far because of the much higher sensitivity to V_R and g_L of the used B physics measurement. A lower limit of 8.2 TeV, like it emerges from V_R in the latter combination, is not possible or at least extremely difficult to test in direct searches at the LHC, even at a centre-of-mass energy of $\sqrt{s} = 14 \text{ TeV}$, because the partons inside the colliding protons contributing to the relevant interactions only carry a fraction of the energy of the protons. The lower 95% C.L. limits for the energy scale Λ from Reference [131] varies from 430 GeV to 1 TeV. These limits are of the same order of magnitude as the lower limits obtained here from

⁹The largest absolute value of the lower and upper value is taken for each coupling. For V_L , only the limits around the Standard Model value are considered, which is valid because this is just an estimation.

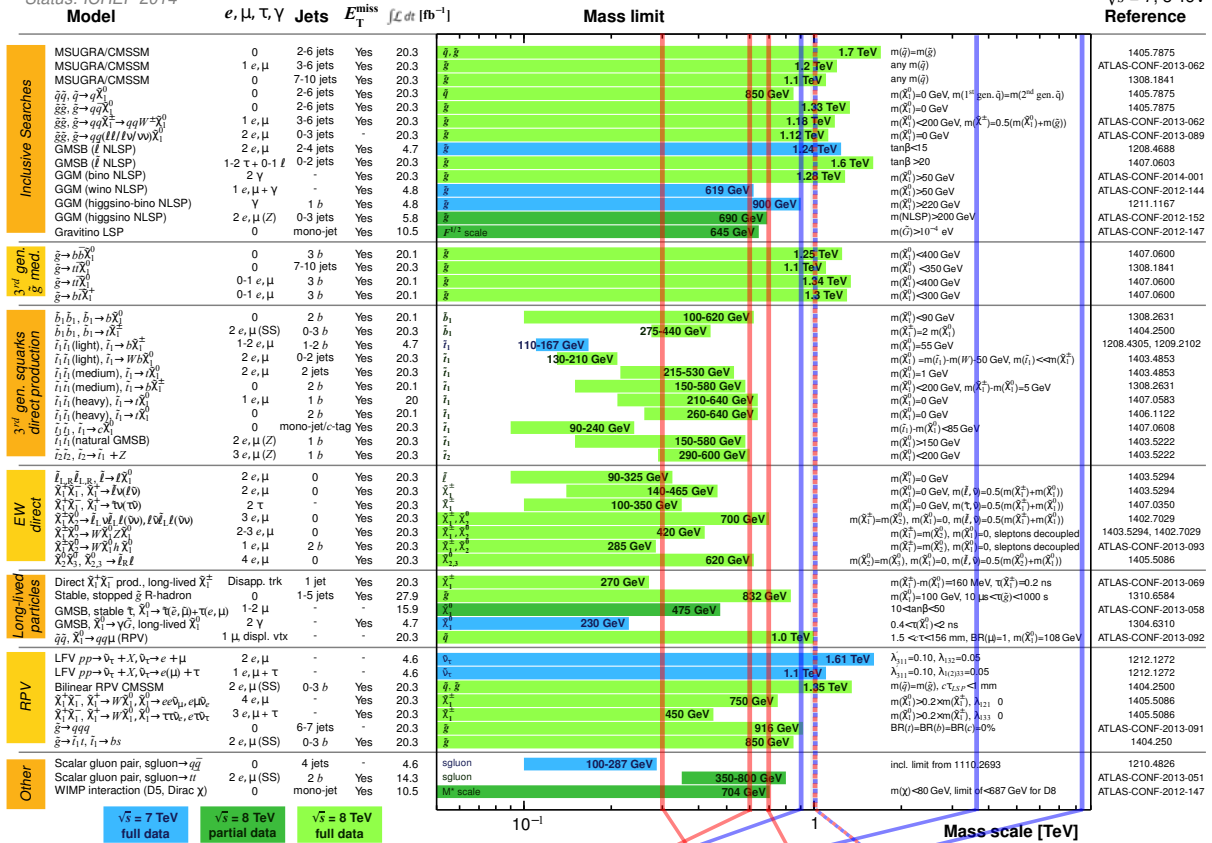
6.3 Energy scale of the effective operators

ATLAS SUSY Searches* - 95% CL Lower Limits

Status: ICHEP 2014

ATLAS Preliminary

$\sqrt{s} = 7, 8 \text{ TeV}$



*Only a selection of the available mass limits on new states or phenomena is shown. All limits quoted are observed minus 1 σ theoretical signal cross section uncertainty.

both top quark measurements
 both top quark- and B-physics measurements

V_L V_R g_L g_R

Figure 6.6: 95% C.L. mass exclusion limits on new states or phenomena for several supersymmetric models [143] in comparison to the bounds from Table 6.5. The red lines indicate the lower 95% C.L. bounds on the energy scale of the effective operators from the combination of the two top quark measurements for the different couplings and the blue lines indicate the lower 95% C.L. bounds from the combination of the top quark measurements with the B-physics measurement for the different couplings.

the combination of the two top quark measurements.

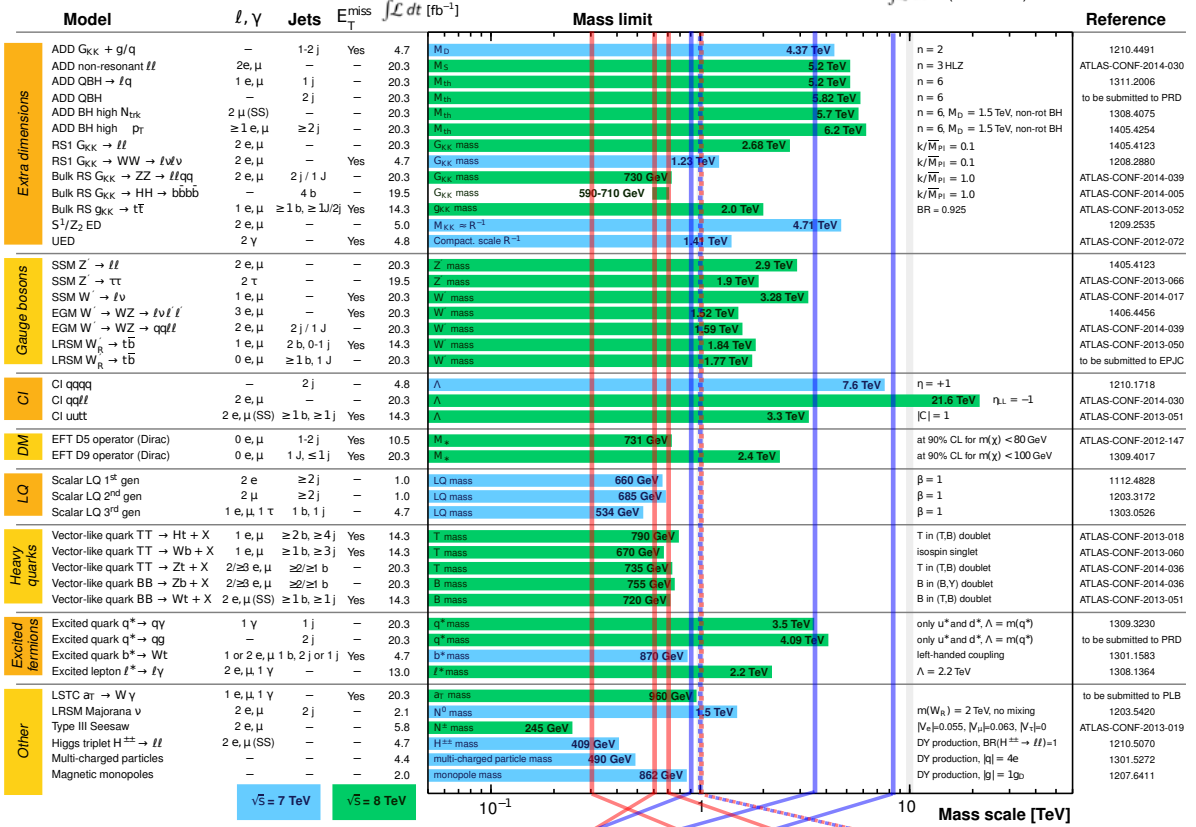
Figures 6.6 and 6.7 show the 95% C.L. mass exclusion limits on new states or phenomena for several models of physics beyond the Standard Model from different measurements in comparison to the bounds from Table 6.5. It has to be pointed out that in this thesis, the limits on the energy scale of the effective operators are obtained by a rough approximation and also do not set bounds on any of these specific models listed here. The comparison only serves the purpose to give an idea of the meaning of these bounds and to show of which order of magnitude the 95% C.L. bounds on physics beyond the Standard Model from direct searches are in comparison to the bounds obtained here.

These bounds are rough approximations, only hinting where new physics affecting the

ATLAS Exotics Searches* - 95% CL Exclusion
 Status: ICHEP 2014

ATLAS Preliminary

$\int \mathcal{L} dt = (1.0 - 20.3) \text{ fb}^{-1}$ $\sqrt{s} = 7, 8 \text{ TeV}$



*Only a selection of the available mass limits on new states or phenomena is shown.

both top quark measurements
 both top quark- and B-physics measurements

Figure 6.7: 95% C.L. mass exclusion limits on new states or phenomena for several other models of physics beyond the Standard Model [144] in comparison to the bounds from Table 6.5. The red lines indicate the lower 95% C.L. bounds on the energy scale of the effective operators from the combination of the two top quark measurements for the different couplings and the blue lines indicate the lower 95% C.L. bounds from the combination of the top quark measurements with the B-physics measurement for the different couplings.

Wtb vertex could still exist. To be able to set better limits, the values of the coefficients $C_{\phi q}^{(3)}$, C_{dW} , $C_{\phi\phi}$, C_{uW} and C_{gW} have to be known to some extent.

Summary, conclusion and outlook

In this thesis, anomalous couplings at the Wtb vertex are constrained by combining measurements sensitive to this vertex. These couplings emerge from an effective field theory assuming new electroweak physics to exist at mass scales not yet accessible. The left-handed vector coupling V_L , the right-handed vector coupling V_R , the left-handed tensor coupling g_L and the right-handed tensor coupling g_R are studied in this thesis, assuming them to be real. While the left-handed vector coupling acquires the value $V_L \sim 1$ in the Standard Model, the other three couplings vanish in the Standard Model. For the combination, two measurements conducted by the ATLAS collaboration are chosen: a measurement of the W helicity fractions and a measurement of the t -channel single top quark production cross section. In the process of the combination, it is necessary to obtain the correlations between the sources of systematic uncertainties of the two measurements. Because the sources of systematic uncertainties are categorised and processed in different ways for the two measurements, a more general categorisation of these sources has to be figured out in order to compare them and to determine the correlations. After taking into account the uncertainties of the Standard Model predictions, the total correlation matrix and the total uncertainties are obtained. The total correlation between the two measurements with respect to their sources of systematic uncertainties is approximately 20%. The combination is conducted with the *Bayesian Analysis Toolkit* (BAT) using Bayesian reasoning.

Ensemble tests confirm that the correlations between the systematic uncertainties of the two measurements have to be known precisely in order to perform the combination correctly. As a further study, a measurement of the branching ratio of the weak radiative B meson decay $\bar{B} \rightarrow X_s \gamma$ is added to the combination of the two top quark measurements. This B -physics measurement can be used to set bounds on anomalous Wtb couplings because of the virtual top quark and W boson in the loop of the process $b \rightarrow s \gamma$ included in this decay. Assuming that no other new physics phenomena contribute to the loop, the model of this observable is much more sensitive to V_R and g_L than the two top quark measurements.

Summary, conclusion and outlook

The fits to the experimental data are conducted in one, two and four dimensions of the anomalous couplings. The combination of the two measurements leads to an obvious improvement of the bounds on anomalous Wtb couplings, where huge areas of parameter space can be excluded with respect to the bounds from the single measurements. For the two- and four-dimensional fits, the Standard Model values of the anomalous couplings always lie within the smallest 95.5% credibility level intervals of all posterior distributions. The smallest 95% C.L. bounds from the one-dimensional fits of the combination of the two top quark measurements are

$$\begin{aligned} -0.05(1) &\leq V_L - 1 \leq 0.17(1) , \\ -0.30(1) &\leq V_R \leq 0.31(1) , \\ -0.19(1) &\leq g_L \leq 0.16(1) \quad \text{and} \\ -0.094(1) &\leq g_R \leq 0.029(1) , \end{aligned}$$

which is consistent with the Standard Model values of the anomalous couplings. There is also a second 95% C.L. interval for the left-handed vector coupling which is $-2.17(1) \leq V_L - 1 \leq -1.94(1)$. The combination of the two top quark measurements with the measurement of the branching ratio of the process $\bar{B} \rightarrow X_s \gamma$ yields tighter bounds compared to the fit of the two top quark measurements only, especially for V_R and g_L , and constrains the two-dimensional distributions from the fits to the B -physics measurement only.

The comparison between this and two other recent combinations setting bounds on anomalous couplings yields that the bounds on g_R obtained in this thesis are the narrowest ones compared to the other two combinations. Also, the other combinations do not take into account the correlations between the combined measurements, which is necessary to set precise bounds on anomalous couplings. The combination of the two top quark measurements constrains new electroweak physics to exist above energies between 300 GeV and 1000 GeV.

The combination of the two top quark measurements might not set the tightest bounds on all anomalous Wtb couplings, but the determination of the correlations between the two measurements, which took in fact the most effort of the whole combination, leads to more precise bounds than the bounds from other combinations which just combine a lot of measurements without taking into account their correlations. To determine these correlations, an insight into the measurement's analysis is required. Therefore it is necessary that these kind of combinations are conducted by the collaborations conducting

the combined measurements.

It is possible to consider further measurements uncorrelated to the two top quark measurements for the combination. One example shown here is the combination with a B -physics measurement. Another possibility is to combine the two measurements with TEVATRON results. For this purpose, correlations between the DØ, CDF and ATLAS measurements have to be taken into account and it has to be checked if it is possible to get the required insight into the TEVATRON measurements. Apart from the correlations, especially the combination with a W helicity measurement from the TEVATRON could be conducted without much effort since the model in dependence on anomalous couplings is already implemented in the framework presented in this thesis. It is also possible to include prior knowledge from other fit results of anomalous Wtb couplings in the posterior probability. Possibilities for further studies are to take into account the imaginary parts of V_L , V_R , g_L and g_R or include other anomalous Wtb couplings. The framework presented in this thesis can also be used to combine measurements to constrain other anomalous couplings for example for the $gt\bar{t}$, $Zt\bar{t}$, $\gamma t\bar{t}$ or $Ht\bar{t}$ vertices¹⁰. One of the next steps for these studies is taking into account the acceptance in dependence on the anomalous couplings. This will have an effect on the observables of the t -channel cross section measurement.

¹⁰ $gt\bar{t}$ vertex: coupling of a gluon to two top quarks.

$Zt\bar{t}$ vertex: coupling of a Z boson to two top quarks.

$\gamma t\bar{t}$ vertex: coupling of a photon to two top quarks.

$Ht\bar{t}$ vertex: coupling of a Higgs boson to two top quarks.

Bibliography

- [1] F. Abe, et al. (CDF Collaboration), Observation of Top Quark Production in $\bar{p}p$ Collisions with the Collider Detector at Fermilab, Phys.Rev.Lett. **74**, 2626 (1995)
- [2] S. Abachi, et al. (D0 Collaboration), Observation of the Top Quark, Phys.Rev.Lett. **74**, 2632 (1995)
- [3] S. P. Martin, A Supersymmetry primer (1997), arXiv:hep-ph/9709356 [hep-ph]
- [4] K. Kröninger, private communication
- [5] A. Caldwell, D. Kollár, K. Kröninger, BAT - The Bayesian analysis toolkit, Comput.Phys.Commun. **180**, 2197 (2009)
- [6] C. Fischer, Measurement of the W-Helicity in Top-Quark Decays with the ATLAS Experiment, Master's thesis, II. Institute of Physics, Georg-August-University of Göttingen (2013), II.Physik-UniGö-MSc-2013/03
- [7] ATLAS Collaboration, Comprehensive measurements of t -channel single top-quark production cross sections at $\sqrt{s} = 7$ TeV with the ATLAS detector, CERN-PH-EP-2014-133 (2014), arXiv:1406.7844 [hep-ex]
- [8] J. A. Aguilar-Saavedra, et al., Probing anomalous Wtb couplings in top pair decays, Eur.Phys.J. **C50**, 519 (2007)
- [9] F. Bach, T. Ohl, Anomalous Top Couplings at Hadron Colliders Revisited, Phys.Rev. **D86**, 114026 (2012)
- [10] Y. Amhis, et al. (Heavy Flavor Averaging Group), Averages of B-Hadron, C-Hadron, and tau-lepton properties as of early 2012 (2012), arXiv:1207.1158 [hep-ex]
- [11] J. Drobnak, S. Fajfer, J. F. Kamenik, Probing anomalous tWb interactions with rare B decays, Nucl.Phys. **B855**, 82 (2012)

Bibliography

- [12] K. Olive, P. D. Group, Review of Particle Physics, Chin.Phys. **C38(9)**, 090001 (2014)
- [13] D. Griffiths, Introduction to Elementary Particles, Wiley (2008)
- [14] F. Halzen, A. D. Martin, Quarks and Leptons, Wiley (1985)
- [15] A. Einstein, Über einen die Erzeugung und Verwandlung des Lichtes betreffenden heuristischen Gesichtspunkt, Annalen Phys. **322(6)**, 132 (1905)
- [16] M. Planck, Über das Gesetz der Energieverteilung im Normalspectrum, Annalen Phys. **309(3)**, 553 (1901)
- [17] S. L. Glashow, Partial-symmetries of weak interactions, Nucl.Phys. **22(4)**, 579 (1961)
- [18] S. L. Glashow, J. Iliopoulos, L. Maiani, Weak Interactions with Lepton-Hadron Symmetry, Phys.Rev. **D2**, 1285 (1970)
- [19] A. Salam, J. Ward, Electromagnetic and weak interactions, Phys.Lett. **13(2)**, 168 (1964)
- [20] S. Salam, Elementary Particle Theory, Almquist and Wiksells, Stockholm (1969)
- [21] S. Weinberg, A Model of Leptons, Phys.Rev.Lett. **19**, 1264 (1967)
- [22] G. Arnison, et al., Experimental observation of isolated large transverse energy electrons with associated missing energy at $\sqrt{s} = 540$ GeV, Phys.Lett. **B122(1)**, 103 (1983)
- [23] M. Banner, et al., Observation of single isolated electrons of high transverse momentum in events with missing transverse energy at the CERN $\bar{p}p$ collider, Phys.Lett. **B122(5–6)**, 476 (1983)
- [24] G. Arnison, et al., Experimental observation of lepton pairs of invariant mass around 95 GeV/c² at the CERN SPS collider, Phys.Lett. **B126(5)**, 398 (1983)
- [25] P. Bagnaia, et al., Evidence for $Z^0 \rightarrow e^+e^-$ at the CERN $\bar{p}p$ collider, Phys.Lett. **B129(1–2)**, 130 (1983)
- [26] R. Brandelik, et al., Evidence for planar events in e^+e^- annihilation at high energies, Phys.Lett. **B86(2)**, 243 (1979)

- [27] C. Berger, et al., Evidence for gluon bremsstrahlung in e^+e^- annihilations at high energies, Phys.Lett. **B86(3–4)**, 418 (1979)
- [28] W. Bartel, et al., Observation of planar three-jet events in e^+e^- annihilation and evidence for gluon bremsstrahlung, Phys.Lett. **B91(1)**, 142 (1980)
- [29] C. Berger, et al., Jet analysis of the $\Upsilon(9.46)$ decay into charged hadrons, Phys.Lett. **B82(3–4)**, 449 (1979)
- [30] C. S. Wu, et al., Experimental Test of Parity Conservation in Beta Decay, Phys.Rev. **105**, 1413 (1957)
- [31] E. D. Bloom, et al., High-Energy Inelastic $e - p$ Scattering at 6° and 10° , Phys.Rev.Lett. **23**, 930 (1969)
- [32] M. Breidenbach, et al., Observed Behavior of Highly Inelastic Electron-Proton Scattering, Phys.Rev.Lett. **23**, 935 (1969)
- [33] R. P. Feynman, Very High-Energy Collisions of Hadrons, Phys.Rev.Lett. **23**, 1415 (1969)
- [34] M. Gell-Mann, A schematic model of baryons and mesons, Phys.Lett. **8(3)**, 214 (1964)
- [35] G. Zweig, An SU(3) model for strong interaction symmetry and its breaking. Version 1, CERN-TH-401 (1964)
- [36] G. Zweig, An SU(3) model for strong interaction symmetry and its breaking. Version 2, CERN-TH-412, NP-14146, PRINT-64-170 (1964)
- [37] M. Thomson, Modern Particle Physics, Cambridge University Press (2013)
- [38] S. L. Glashow, J. Iliopoulos, L. Maiani, Weak Interactions with Lepton-Hadron Symmetry, Phys.Rev. **D2**, 1285 (1970)
- [39] B. J. Bjørken, S. L. Glashow, Elementary particles and SU(4), Phys.Lett. **11(3)**, 255 (1964)
- [40] J. J. Aubert, et al., Experimental Observation of a Heavy Particle J , Phys.Rev.Lett. **33**, 1404 (1974)
- [41] J. E. Augustin, et al., Discovery of a Narrow Resonance in e^+e^- Annihilation, Phys.Rev.Lett. **33**, 1406 (1974)

Bibliography

- [42] M. Kobayashi, T. Maskawa, CP Violation in the Renormalizable Theory of Weak Interaction, *Prog.Theor.Phys.* **49**, 652 (1973)
- [43] S. W. Herb, et al., Observation of a Dimuon Resonance at 9.5 GeV in 400-GeV Proton-Nucleus Collisions, *Phys.Rev.Lett.* **39**, 252 (1977)
- [44] J. J. Thomson, XL. Cathode Rays, *Phil.Mag. Series 5* **44(269)**, 293 (1897)
- [45] E. Fermi, Versuch einer Theorie der β -Strahlen, *Z.Phys.* (1934)
- [46] F. E. Wilson, Fermi's Theory of Beta Decay, *Am.J.Phys.* (1968)
- [47] C. L. Cowan, et al., Detection of the Free Neutrino: a Confirmation, *Science* **124(3212)**, 103 (1956)
- [48] S. H. Neddermeyer, C. D. Anderson, Note on the Nature of Cosmic-Ray Particles, *Phys.Rev.* **51**, 884 (1937)
- [49] J. C. Street, E. C. Stevenson, New Evidence for the Existence of a Particle of Mass Intermediate Between the Proton and Electron, *Phys.Rev.* **52**, 1003 (1937)
- [50] G. Danby, et al., Observation of High-Energy Neutrino Reactions and the Existence of Two Kinds of Neutrinos, *Phys.Rev.Lett.* **9**, 36 (1962)
- [51] M. L. Perl, et al., Evidence for Anomalous Lepton Production in e^+e^- Annihilation, *Phys.Rev.Lett.* **35**, 1489 (1975)
- [52] K. Kodama, et al., Observation of tau neutrino interactions, *Phys.Lett.* **B504(3)**, 218 (2001)
- [53] P. W. Anderson, Plasmons, Gauge Invariance, and Mass, *Phys.Rev.* **130**, 439 (1963)
- [54] F. Englert, R. Brout, Broken Symmetry and the Mass of Gauge Vector Mesons, *Phys.Rev.Lett.* **13**, 321 (1964)
- [55] P. W. Higgs, Broken Symmetries and the Masses of Gauge Bosons, *Phys.Rev.Lett.* **13**, 508 (1964)
- [56] G. S. Guralnik, C. R. Hagen, T. W. B. Kibble, Global Conservation Laws and Massless Particles, *Phys.Rev.Lett.* **13**, 585 (1964)
- [57] ATLAS Collaboration, Observation of a new particle in the search for the Standard Model Higgs boson with the ATLAS detector at the LHC, *Phys.Lett.* **B716(1)**, 1 (2012)

- [58] CMS Collaboration, Observation of a new boson at a mass of 125 GeV with the CMS experiment at the LHC, *Phys.Lett.* **B716**, 30 (2012)
- [59] R. P. Woodard, How Far Are We from the Quantum Theory of Gravity?, *Rept.Prog.Phys.* **72**, 126002 (2009)
- [60] The ATLAS, CDF, CMS and DØ Collaborations, First combination of Tevatron and LHC measurements of the top-quark mass, ATLAS-CONF-2014-008, CDF-NOTE-11071, CMS-PAS-TOP-13-014, D0-NOTE –6416 (2014)
- [61] C. Battilana (ATLAS, CMS Collaboration), Top quark Physics at the LHC pages 91–100 (2013), arXiv:1309.5307 [hep-ex]
- [62] I. Bigi, et al., Production and decay properties of ultra-heavy quarks, *Phys.Lett.* **B181(1–2)**, 157 (1986)
- [63] T. A. Aaltonen, et al. (CDF Collaboration, D0 Collaboration), Combination of measurements of the top-quark pair production cross section from the Tevatron Collider, *Phys.Rev.* **D89**, 072001 (2014)
- [64] ATLAS Collaboration, Measurement of the $t\bar{t}$ production cross-section using $e\mu$ events with b -tagged jets in pp collisions at $\sqrt{s} = 7$ and 8 TeV with the ATLAS detector, CERN-PH-EP-2014-124 (2014), arXiv:1406.5375 [hep-ex]
- [65] CMS Collaboration, Measurement of the $t\bar{t}$ production cross section in the dilepton channel in pp collisions at $\sqrt{s} = 7$ TeV, *JHEP* **2012(11)**, 1 (2012)
- [66] ATLAS Collaboration, Measurement of the $t\bar{t}$ production cross-section in pp collisions at $\sqrt{s} = 7$ TeV using kinematic information of lepton+jets events, ATLAS-CONF-2011-121 (2011)
- [67] CMS Collaboration, Measurement of the $t\bar{t}$ production cross section in pp collisions at $\sqrt{s} = 7$ TeV with lepton+jets final states, *Phys.Lett.* **B720(1–3)**, 83 (2013)
- [68] ATLAS Collaboration, Measurement of the top quark pair production cross section in the single-lepton channel with ATLAS in proton-proton collisions at 8 TeV using kinematic fits with b -tagging, ATLAS-CONF-2012-149 (2012)
- [69] CMS Collaboration, Top pair cross section in e/μ +jets at 8 TeV, CMS-PAS-TOP-12-006 (2012)

Bibliography

- [70] Combination of ATLAS and CMS top-quark pair cross-section measurements using proton-proton collisions at $\sqrt{s} = 8$ TeV, ATLAS-CONF-2014-054 (2014)
- [71] CMS Collaboration, Measurement of the $t\bar{t}$ production cross section in the dilepton channel in pp collisions at $\sqrt{s} = 8$ TeV, JHEP **1402**, 024 (2014)
- [72] M. Czakon, P. Fiedler, A. Mitov, Total Top-Quark Pair-Production Cross Section at Hadron Colliders Through $\mathcal{O}(\alpha_s^4)$, Phys.Rev.Lett. **110**, 252004 (2013)
- [73] TOPLHCWG: WG on Top physics at the LHC (2014), As of 8 October 2014, URL <https://atlas.web.cern.ch/Atlas/GROUPS/PHYSICS/CombinedSummaryPlots/TOP/>
- [74] N. Kidonakis, Next-to-next-to-leading-order collinear and soft gluon corrections for t-channel single top quark production, Phys.Rev. **D83**, 091503 (2011)
- [75] N. Kidonakis, Two-loop soft anomalous dimensions for single top quark associated production with a W^- or H^- , Phys.Rev. **D82**, 054018 (2010)
- [76] N. Kidonakis, Next-to-next-to-leading logarithm resummation for s-channel single top quark production, Phys.Rev. **D81**, 054028 (2010)
- [77] T. A. Aaltonen, et al. (CDF Collaboration, D0 Collaboration), Observation of s-channel production of single top quarks at the Tevatron, Phys.Rev.Lett. **112**, 231803 (2014)
- [78] ATLAS Collaboration, Evidence for the associated production of a W boson and a top quark in ATLAS at $\sqrt{s} = 7$ TeV, Phys.Lett. **B716(1)**, 142 (2012)
- [79] ATLAS Collaboration, Measurement of the Inclusive and Fiducial Cross-Section of Single Top-Quark t -Channel Events in pp Collisions at $\sqrt{s} = 8$ TeV, ATLAS-CONF-2014-007 (2014)
- [80] ATLAS Collaboration, Measurement of the cross-section for associated production of a top quark and a W boson at $\sqrt{s} = 8$ TeV with the ATLAS detector, ATLAS-CONF-2013-100 (2013)
- [81] ATLAS Collaboration, Single top-quark production (2014), ATLAS Top physics group, As of 8 October 2014, URL <https://atlas.web.cern.ch/Atlas/GROUPS/PHYSICS/CombinedSummaryPlots/TOP/>

- [82] ATLAS Collaboration, Search for s-Channel Single Top-Quark Production in pp Collisions at $\sqrt{s} = 7$ TeV, ATLAS-CONF-2011-118 (2011)
- [83] ATLAS Collaboration, Search for s-channel single top-quark production in proton-proton collisions at $\sqrt{s}=8$ TeV with the ATLAS detector, CERN-PH-EP-2014-224 (2014), arXiv:1410.0647 [hep-ex]
- [84] W. Buchmüller, D. Wyler, Effective lagrangian analysis of new interactions and flavour conservation, Nucl.Phys. **B268(3–4)**, 621 (1986)
- [85] C. Zhang, S. Willenbrock, Effective-Field-Theory Approach to Top-Quark Production and Decay, Phys.Rev. **D83**, 034006 (2011)
- [86] J. A. Aguilar-Saavedra, Single top quark production at LHC with anomalous Wtb couplings, Nucl.Phys. **B804**, 160 (2008)
- [87] H. S. Do, S. Groote, J. G. Körner, M. C. Mauser, Electroweak and finite width corrections to top quark decays into transverse and longitudinal W bosons, Phys.Rev. **D67**, 091501 (2003)
- [88] B. Grzadkowski, M. Misiak, Anomalous Wtb coupling effects in the weak radiative B-meson decay, Phys.Rev. **D78**, 077501 (2008)
- [89] ATLAS Collaboration, Measurement of the W boson polarization in top quark decays with the ATLAS detector, JHEP **1206**, 088 (2012)
- [90] ATLAS Collaboration, Measurement of the W -boson polarisation in top quark decays in pp collision data at $\sqrt{s} = 7$ TeV using the ATLAS detector, ATLAS-CONF-2011-037 (2011)
- [91] CMS Collaboration, W helicity in top pair events, CMS-PAS-TOP-11-020 (2012)
- [92] ATLAS Collaboration, Combination of the ATLAS and CMS measurements of the W -boson polarization in top-quark decays, ATLAS-CONF-2013-033 (2013)
- [93] M. E. Peskin, D. V. Schroeder, An Introduction to Quantum Field Theory, Addison-Wesley Publishing Company (1995)
- [94] M. S. Chanowitz, M. K. Gaillard, The TeV physics of strongly interacting W 's and Z 's, Nucl.Phys. **B261(0)**, 379 (1985)
- [95] J. M. Cornwall, D. N. Levin, G. Tiktopoulos, Derivation of Gauge Invariance from High-Energy Unitarity Bounds on the s Matrix, Phys.Rev. **D10**, 1145 (1974)

Bibliography

- [96] A. Czarnecki, J. G. Korner, J. H. Piclum, Helicity fractions of W bosons from top quark decays at NNLO in QCD, *Phys.Rev.* **D81**, 111503 (2010)
- [97] A. Quadt, Top quark physics at hadron colliders, *Eur.Phys.J. C - Particles and Fields* **48(3)**, 835 (2006)
- [98] CMS Collaboration, Measurement of the W boson helicity in events with a single reconstructed top quark in pp collisions at $\sqrt{s} = 8$ TeV, CMS-TOP-12-020, CERN-PH-EP-2014-242 (2014), arXiv:1410.1154 [hep-ex]
- [99] R. Frederix, E. Re, P. Torrielli, Single-top t-channel hadroproduction in the four-flavour scheme with POWHEG and aMCNLO, *JHEP* **2012(9)**, 130 (2012)
- [100] T. M. P. Tait, C.-P. Yuan, Single top quark production as a window to physics beyond the standard model, *Phys.Rev.* **D63**, 014018 (2000)
- [101] L. Evans, P. Bryant, LHC Machine, *JINST* **3(08)**, S08001 (2008)
- [102] S. Myers, The Large Hadron Collider 2008–2013, *Int.J.Mod.Phys.* **A28(25)**, 1330035 (2013)
- [103] ATLAS Collaboration, The ATLAS Experiment at the CERN Large Hadron Collider, *JINST* **3(08)**, S08003 (2008)
- [104] J. Erdmann, et al., A likelihood-based reconstruction algorithm for top-quark pairs and the KLFitter framework, *Nucl.Instrum.Meth.* **A748**, 18 (2014)
- [105] A. H. Knue, Measurement of the W-boson Polarisation in Top-Quark Decays with the ATLAS Detector, Ph.D. thesis, II. Institute of Physics, Georg-August-University of Göttingen (2013), II.Physik-UniGö-Diss-2013/01
- [106] K. Becker, private communication
- [107] ATLAS Collaboration, Jet energy scale and its systematic uncertainty in proton-proton collisions at $\sqrt{s}=7$ TeV with ATLAS 2011 data, ATLAS-CONF-2013-004 (2013)
- [108] ATLAS Collaboration, Jet energy measurement with the ATLAS detector in proton-proton collisions at $\sqrt{s} = 7$ TeV, *Eur.Phys.J.* **C73**, 2304 (2013)
- [109] ATLAS Collaboration, Jet energy measurement and systematic uncertainties using tracks for jets and for b-quark jets produced in proton-proton collisions at $\sqrt{s} = 7$ TeV in the ATLAS detector, ATLAS-CONF-2013-002 (2013)

- [110] ATLAS Collaboration, Jet energy resolution in proton-proton collisions at $\sqrt{s} = 7$ TeV recorded in 2010 with the ATLAS detector, *Eur.Phys.J.* **C73**, 2306 (2013)
- [111] ATLAS Collaboration, Electron performance measurements with the ATLAS detector using the 2010 LHC proton-proton collision data, *Eur.Phys.J.* **C72**, 1909 (2012)
- [112] ATLAS Collaboration, Muon Momentum Resolution in First Pass Reconstruction of pp Collision Data Recorded by ATLAS in 2010, ATLAS-CONF-2011-046 (2011)
- [113] V. M. Abazov, et al. (D0 Collaboration), Measurement of the $p\bar{p} \rightarrow t\bar{t}$ production cross section at $\sqrt{s} = 1.96$ -TeV in the fully hadronic decay channel., *Phys.Rev.* **D76**, 072007 (2007)
- [114] G. Facini, JetVertexFraction: Selecting jets in pile-up events using jet-vertex association, CERN TWiki (2012), As of 8 October 2014, URL <https://twiki.cern.ch/twiki/bin/view/Main/JetVertexFraction>
- [115] ATLAS Collaboration, Combination of ATLAS and CMS results on the mass of the top quark using up to 4.9 fb^{-1} of data, ATLAS-CONF-2012-095 (2012)
- [116] J. M. Campbell, J. W. Huston, W. J. Stirling, Hard Interactions of Quarks and Gluons: A Primer for LHC Physics, *Rept.Prog.Phys.* **70**, 89 (2007)
- [117] F. Maltoni, et al., Choosing the Factorization Scale in Perturbative QCD, CP3-07-10 (2007), arXiv:hep-ph/0703156 [HEP-PH]
- [118] ATLAS Collaboration, Luminosity Determination in pp Collisions at $\sqrt{s} = 7$ TeV Using the ATLAS Detector at the LHC, *Eur.Phys.J.* **C71**, 1630 (2011)
- [119] ATLAS Collaboration, Luminosity Determination in pp Collisions at $\sqrt{s} = 7$ TeV using the ATLAS Detector in 2011, ATLAS-CONF-2011-116 (2011)
- [120] C. Fischer, private communication
- [121] L. Lyons, D. Gibaut, P. Clifford, How to combine correlated estimates of a single physical quantity, *Nucl.Instrum.Meth.* **A270(1)**, 110 (1988)
- [122] T. Bayes, An essay towards solving a problem in the doctrine of chances, *Phil. Trans. of the Royal Soc. of London* **53**, 370 (1763)
- [123] F. Bach, private communication

Bibliography

- [124] B. Grzadkowski, M. Misiak, Anomalous Wtb coupling effects in the weak radiative B-meson decay (2008), arXiv:0802.1413 [hep-ph]
- [125] M. Misiak, private communication
- [126] M. Misiak, et al., Estimate of $\mathcal{B}(\bar{B} \rightarrow X_s \gamma)$ at $O(\alpha_s^2)$, Phys.Rev.Lett. **98**, 022002 (2007)
- [127] S. Karlin, H. Taylor, A First Course in Stochastic Processes, Academic Press (1975)
- [128] W. R. Gilks, S. Richardson, D. Spiegelhalter, Markov Chain Monte Carlo in Practice, Chapman and Hall (1996)
- [129] N. Metropolis, et al., Equation of State Calculations by Fast Computing Machines, J.Chem.Phys. **21(6)**, 1087 (1953)
- [130] E. Barberio, et al. (Heavy Flavor Averaging Group (HFAG) Collaboration), Averages of b -hadron properties at the end of 2006, FERMILAB-FN-0815-E (2007), arXiv:0704.3575 [hep-ex]
- [131] M. Fabbrichesi, M. Pinamonti, A. Tonerio, Limits on anomalous top quark gauge couplings from Tevatron and LHC data (2014), arXiv:1406.5393 [hep-ph]
- [132] CMS Collaboration, Measurement of the W-boson helicity in top decays from $t\bar{t}$ production in lepton+jets events at the LHC at $\sqrt{s} = 8$ TeV, CMS-PAS-TOP-13-008 (2013)
- [133] CMS Collaboration, Measurement of the single-top-quark t -channel cross section in pp collisions at $\sqrt{s} = 7$ TeV, JHEP **1212**, 035 (2012)
- [134] CMS Collaboration, Measurement of the t -channel single-top-quark production cross section and of the $|V_{tb}|$ CKM matrix element in pp collisions at $\sqrt{s} = 8$ TeV, JHEP **1406**, 090 (2014)
- [135] CMS Collaboration, Evidence for associated production of a single top quark and W boson in pp collisions at $\sqrt{s} = 7$ TeV, Phys.Rev.Lett. **110**, 022003 (2013)
- [136] CMS Collaboration, Observation of the associated production of a single top quark and a W boson in pp collisions at $\sqrt{s} = 8$ TeV, Phys.Rev.Lett. **112**, 231802 (2014)
- [137] N. D. Christensen, C. Duhr, FeynRules - Feynman rules made easy, Comput.Phys.Commun. **180**, 1614 (2009)

- [138] J. Alwall, et al., MadGraph 5 : Going Beyond, JHEP **1106**, 128 (2011)
- [139] C. Bernardo, et al., Studying the Wtb vertex structure using recent LHC results (2014), arXiv:1408.7063 [hep-ph]
- [140] J. Fleischer, et al., Status of electroweak corrections to top pair production, DESY-02-203 (2002), arXiv:hep-ph/0211428 [hep-ph]
- [141] T. Aaltonen, et al. (CDF and D0 Collaborations), Combination of CDF and D0 measurements of the W boson helicity in top quark decays, Phys.Rev. **D85**, 071106 (2012)
- [142] T. Aaltonen, et al. (CDF Collaboration), Updated Measurement of the Single Top Quark Production Cross Section in the Missing Transverse Energy plus Jets Topology in $p\bar{p}$ Collisions at $\sqrt{s} = 1.96$ TeV, CDF/PUB/TOP/CDFR/11033 (2014)
- [143] ATLAS Collaboration, ATLAS SUSY Searches (2014), ATLAS Supersymmetry physics group, Status: ICHEP 2014, As of 8 October 2014, URL https://atlas.web.cern.ch/Atlas/GROUPS/PHYSICS/CombinedSummaryPlots/SUSY/index.html#ATLAS_SUSY_Summary
- [144] ATLAS Collaboration, ATLAS Exotics Searches (2014), ATLAS Exotic physics group, Status: ICHEP 2014, As of 8 October 2014, URL https://atlas.web.cern.ch/Atlas/GROUPS/PHYSICS/CombinedSummaryPlots/EXOTICS/index.html#ATLAS_Exotics_Summary
- [145] S. Chen, et al. (CLEO Collaboration), Branching Fraction and Photon Energy Spectrum for $b \rightarrow s\gamma$, Phys.Rev.Lett. **87**, 251807 (2001)
- [146] K. Abe, et al., A measurement of the branching fraction for the inclusive $B \rightarrow X_s\gamma$ decays with the Belle detector, Phys.Lett. **B511(2-4)**, 151 (2001)
- [147] B. Aubert, et al. (BABAR Collaboration), Measurements of the $B \rightarrow X_s\gamma$ branching fraction and photon spectrum from a sum of exclusive final states, Phys.Rev. **D72**, 052004 (2005)
- [148] B. Aubert, et al. (BABAR Collaboration), Measurement of the Branching Fraction and Photon Energy Moments of $B \rightarrow X_s\gamma$ and $A_{CP}(B \rightarrow X_{s+d}\gamma)$, Phys.Rev.Lett. **97**, 171803 (2006)

Bibliography

- [149] B. Aubert, et al. (BABAR Collaboration), Measurement of the $B \rightarrow X_s \gamma$ branching fraction and photon energy spectrum using the recoil method, *Phys.Rev.* **D77**, 051103 (2008)
- [150] A. Limosani, et al. (Belle Collaboration), Measurement of Inclusive Radiative B -Meson Decays with a Photon Energy Threshold of 1.7 GeV, *Phys.Rev.Lett.* **103**, 241801 (2009)
- [151] J. A. Aguilar-Saavedra, N. F. Castro, A. Onofre, Constraints on the Wtb vertex from early LHC data, *Phys.Rev.* **D83**, 117301 (2011)

Acknowledgements

First of all, I would like to thank Prof. Dr. Arnulf Quadt and Prof. Dr. Ariane Frey for being by referees. Also, I would like to thank Prof. Dr. Kevin Alexander Kröninger for being a great specialist contact person. He provided me with lots of creative input and introduced me to the people I communicated with to exchange knowledge. In situations that seemed like a dead end, his experience was an indispensable support. He also provided me with the basic framework that I expanded to do this analysis. He, Prof. Dr. Quadt and Prof. Dr. Frey were the people who encouraged me to keep my focus on particle physics. I am deeply grateful to Prof. Dr. Quadt for making it possible for me to attend the CERN Summer Student Programme and to do my master's thesis in his group.

Special thanks go to Dr. Kathrin Becker and Cora Fischer for giving me the needed insight into their analyses. Without their data, the analysis presented in this thesis would have been impossible. Further thanks go to Dr. Nuno Filipe da Silva Fernandes de Castro for sharing his deep knowledge in anomalous Wtb couplings and for his fresh ideas concerning this combination, as well as to Dr. Fabian Bach and Prof. Dr. Mikołaj Misiak for their help to implement their models of the t -channel single top quark cross section and the branching ratio of the process $\bar{B} \rightarrow X_s \gamma$ into our combination.

I also would like to thank Prof. Dr. Kröninger and Dr. Boris Lemmer for proofreading and discussing this thesis, as well as all people from the II. Institute of Physics in Göttingen for the fruitful discussions about physics and computing topics in the meetings and during the coffee breaks. I really enjoyed the creative atmosphere in this institute.

Zuallerletzt möchte ich noch meiner Familie und meinen Freunden danken. Die Unterstützung meiner Familie hat es mir ermöglicht, unter hervorragenden Bedingungen zu studieren und meine Freunde haben es oft geschafft, meinen Kopf mit anderen Dingen als Physik zu füllen, auch wenn es nicht immer einfach für sie war. Allerdings muss ich ihnen mitteilen, dass mit Abgabe dieser Arbeit ihr Leidensweg noch nicht beendet ist, denn ich fange bald an diesem Institut an, als Doktorand zu arbeiten. Somit werden sie auch in kommender Zeit, mehr oder weniger freiwillig, stets über die interessantesten Aspekte

Acknowledgements

der Physik auf dem Laufenden gehalten. Außerdem möchte ich auch meinen ehemaligen Physiklehrerinnen und Physiklehrern danken, die es schafften, mich so für dieses Fach zu interessieren, dass ich mich schließlich für dieses Studium entschieden und es durchgezogen habe.

Erklärung nach §18(8) der Prüfungsordnung für den Bachelor-Studiengang Physik und den Master-Studiengang Physik an der Universität Göttingen:

Hiermit erkläre ich, dass ich diese Abschlussarbeit selbständig verfasst habe, keine anderen als die angegebenen Quellen und Hilfsmittel benutzt habe und alle Stellen, die wörtlich oder sinngemäß aus veröffentlichten Schriften entnommen wurden, als solche kenntlich gemacht habe.

Darüberhinaus erkläre ich, dass diese Abschlussarbeit nicht, auch nicht auszugsweise, im Rahmen einer nichtbestanden Prüfung an dieser oder einer anderen Hochschule eingereicht wurde.

Göttingen, den 26. Januar 2015

(Nils-Arne Rosien)